



FACULTÉ DES SCIENCES

Jülich Centre for Neutron Science JCNS and Peter Grünberg Institut PGI
JCNS-2, PGI-4: Scattering Methods
“Lattice Dynamics in Emerging Functional Materials” group
Forschungszentrum Jülich

Structure and Lattice Dynamics of Thermoelectric Complex Chalcogenides

Année académique 2011-2012

Dissertation présentée par
Paula Bauer Pereira
en vue de l'obtention du grade de
Docteur en Sciences



FACULTÉ DES SCIENCES

Jülich Centre for Neutron Science JCNS and Peter Grünberg Institut PGI
JCNS-2, PGI-4: Scattering Methods
“Lattice Dynamics in Emerging Functional Materials” group
Forschungszentrum Jülich

Structure and Lattice Dynamics of Thermoelectric Complex Chalcogenides

Année académique 2011-2012

Dissertation présentée par
Paula Bauer Pereira
en vue de l'obtention du grade de
Docteur en Sciences

*“Two roads diverged in a wood, and I
I took the one less traveled by,
And that has made all the difference.”*

- Robert Frost

Acknowledgements

This PhD thesis is the result of the work of many people and I feel thankful to all of them. First, I express my gratitude and admiration to my thesis supervisor Dr. Raphaël P. Hermann. For the last three years he was a constant guide in the rocky path of Scattering Methods and I am thankful for all the shared ideas, dedication and encouragement. My co-supervisor Dr. Werner Schweika is also acknowledged.

I am thankful to my supervisors at the University of Liège, Prof. R. Cloots and Prof. J.-P. Gaspard, and to the PhD thesis committee members, Prof. B. Vertruyen, Prof. M. Verstraete and Dr. E. Müller for accepting to be a part of the jury and their general interest in my work.

My special gratitude to all the colleagues from JCNS-2/PGI-4 and colleagues from partner laboratories at the Forschungszentrum Jülich, especially Mr. D. Bessas, Dr. Anne Houben, Dr. S. Disch, Mr. F. Gossen, Dr. J. de Groot, Dr. A. Houben, Dr. B. Klobes, Mr. J. Persson, Mr. B. Schmitz, Mr. T. Radermacher, Mrs. B. Cela Greven, Dr. D. Faidel and Mr. D. Weber, for all shared information, their help with the set ups and experiments, data analysis, fruitful discussions and comments and for the conviviality during all the period of this PhD. Many thanks to Mrs. T. Claudio Weber for her friendship, nice time, the energetic mood and mutual support.

A list of acknowledgements cannot be complete without mentioning Dr. J. Glad-den and his family. Thank you very much for providing valuable inspiration, example, experience and even data.

I am in debt with the beamline scientists from 6-ID-D at the Advanced Photon Source (Argonne, USA), Dr. D. Robinson, Dr. U. Rütt from PETRA III at the Deutsches Elektronen Synchrotron (Hamburg, Germany), and Dr. O. Gourdon

from POWGEN, at the Spallation Neutron Source (Oak Ridge, USA), for their hard work and help. A special thank you to Dr. I. Sergueev, formerly beam-line scientist at ID18 and ID22 at the European Synchrotron Radiation Facility (ESRF, France), for being so friendly and full of energy, for setting up the beam-line so many times, and for reading this manuscript. I also thank the institutions cited above for providing synchrotron and neutron beam time.

I would like to acknowledge all the support from the members of the NanoKoCh Project, Dr. E. Müller and Dr. J. Dadda (DLR, Köln) for sharing their expertise in the synthesis and characterization of thermoelectric materials, Dr. T. Höche (IWM, Halle) and Ms. S. Perlt (IOM, Leipzig) for the data and beauty extracted from the electron microscope images and Dr. A. Neubrand (IWM, Freiburg) for his knowledge and creativity in the construction of the local thermal conductivity probe. The Bundesministerium für Bildung und Forschung (BMBF) is also acknowledged for funding this project.

A very special thank you to all the friends, the ones that I left back home and were a constant source of motivation, and the ones I made in Germany and around the world over the past three years - too many to cite them all here. To my best friend and flatmate Mrs. Juciana Aleixo, for her patience and time shared over dinners, parties and daily life. Thank you for the company, support and friendship.

I would like to thank above all, my family. My mother, Guaraciaba, thank you for your dedication over the years, example and perseverance, and for the many books in the childhood. My father, Valentim, for his constant concern about the weather in Germany and for making the best caipirinha in the world. My brother Michel, who has been my best friend since I was born. My sisters Daniella and Alessandra, thank you for the attention and comprehension. And my nieces, Ana Beatriz and Valentina, and nephews João Vitor and João Lucas, for their love, and the infinite source of joy and happiness.

Lastly, I deeply thank my boyfriend Bernhard for his love and support, and for believing in me. Even when I had trouble believing in myself.

Publication Dissertation

Chapter 2-4 of this dissertation are manuscripts that are submitted or will be submitted shortly.

Chapter 2: P. Bauer Pereira, S. Gorsse, I. Sergueev, J. Dadda, E. Müller, R. P. Hermann, **Lattice dynamics and structure of GeTe, SnTe and PbTe**, submitted to *Physica Status Solidi B*, August 2012.

Chapter 3: P. Bauer Pereira, I. Sergueev, J. Dadda, E. Müller, R. P. Hermann, **Lattice dynamics in AgSbTe₂**. To be submitted to *Physics Review B*, September 2012.

Chapter 4: P. Bauer Pereira, I. Sergueev, J. Dadda, E. Müller, R. P. Hermann, **Structure and Lattice dynamics in AgPb₁₈SbTe₂₀**. To be submitted to *Journal of Electronic Materials*, September 2012.

Abstract

The goal of this work is to characterize the structure and lattice dynamics of complex chalcogenide alloys. Particular interest is paid to the system $\text{AgPb}_m\text{SbTe}_{m+2}$ (LAST- m), AgSbTe_2 and the binaries PbTe , SnTe and GeTe . Synchrotron radiation studies including high energy X-ray diffraction and nuclear inelastic scattering, and macroscopic measurements of heat capacity and elastic constants were performed. A new resonant ultrasound spectroscopy setup with capable of performing measurements from room temperature to 1073 K was built for mechanical characterization of the thermoelectric alloys at their working temperatures.

The first chapter presents a brief review of relevant information on thermoelectricity and on the materials under study. The characterization methods including heat capacity, resonant ultrasound spectroscopy, X-ray diffraction and nuclear inelastic scattering are introduced. Not as an exhaustive review, but rather in order to give the reader a basic level of understanding and a sense of the accessible information. The introduction is followed by three chapters which address the experimental studies of lattice dynamics in chalcogenide alloys.

Chapter 2 describes the lattice dynamics in the compounds GeTe , SnTe and PbTe studied by ^{119}Sn and ^{125}Te nuclear inelastic scattering. The obtained partial density of phonon states were compared with published theoretical calculations, and the resulting vibrational properties were found to be in good agreement with these reports. Additionally, the phase purity and structure were characterized by high energy X-ray diffraction. The atomic arrangement, rhombohedral for GeTe and cubic for SnTe and PbTe , is seem to affect the density of phonon states, with the NaCl-type structure having a softer character in comparison with the rhombohedral structure.

In Chapter 3, the lattice dynamics of a polycrystalline AgSbTe_2 sample was investigated by ^{121}Sb and ^{125}Te nuclear inelastic scattering, at low temperatures. For this compound, the phonon modes have energies below 25 meV and a sound velocity of $v_s = 1490(30)$ m/s was determined. A simple temperature independent estimation of the lattice thermal conductivity of AgSbTe_2 yielded $\kappa_L = 0.50 \pm 0.05 \text{ Wm}^{-1}\text{K}^{-1}$. The low Debye temperature, $\theta_D = 150(15)$ K combined with the short phonon lifetime and the low sound velocity are found to be key factors for the low thermal conductivity in AgSbTe_2 and are related to the good thermoelectric performance in AgSbTe_2 and AgSbTe_2 containing systems.

Chapter 4 is dedicated to the study of the average and local structure in bulk $\text{AgPb}_{18}\text{SbTe}_{20}$ alloy, by a combined Rietveld and Pair Distribution Function analysis. The strong influence of the synthesis conditions on the lattice parameters and on the composition and the concentration of nanoclusters in LAST-18 is confirmed. Moreover, the ^{121}Sb and ^{125}Te partial density of phonons states were obtained by nuclear inelastic scattering in order to separately characterize the lattice dynamics from the matrix and the nanoinclusions. Additional characterization of the elastic properties and lattice governed properties were performed by resonance ultrasound spectroscopy, heat capacity and thermal expansion measurements.

The final chapter is dedicated to the resonant ultrasound spectroscopy technique, and the process of building up this buffer-rods high-temperature measurement system are presented. Advantages and disadvantages, as well as limitations and difficulties are discussed. Using the “mode-tracking” method, the mechanical behavior of a PbTe and a Niobium sample, from room temperature to 523 K and from room temperature to 973 K, respectively, were investigated.

Résumé

Le but de ce travail est de caractériser les structures et dynamiques de réseau d'alliage de chalcogènes complexes, avec un intérêt particulier pour le système $\text{AgPb}_m\text{SbTe}_{m+2}$ (LAST- m), AgSbTe_2 et les binaires PbTe , SnTe and GeTe . Des mesures utilisant le rayonnement synchrotron, dont la diffraction de rayons X de haute énergie et la diffusion nucléaire inélastique, ainsi que des mesures macroscopiques de chaleur spécifique et de constantes élastiques. Un nouveau spectromètre à résonance d'ultrasons capable de réaliser des mesures jusqu'à 1073 K à été construit pour la caractérisation mécanique d'alliages thermoélectriques à leur température d'utilisation.

Le premier chapitre passe en revue les informations pertinentes sur la thermoélectricité et les matériaux étudiés. Les techniques de caractérisation de chaleur spécifique, de spectroscopie à résonance d'ultrasons, de diffraction de rayons X et de diffusion nucléaire inélastique sont présentées, sans prétention d'exhaustivité, afin de donner au lecteur la compréhension de base et une mesure des informations accessibles. Cette introduction est suivie de trois chapitres consacrés aux études expérimentales de la dynamique de réseaux dans les alliages de chalcogènes.

Le deuxième chapitre décrit la dynamique de réseau dans les composés GeTe , SnTe et PbTe étudiée par diffusion nucléaire inélastique par ^{119}Sn and ^{125}Te . Les densités d'états de phonons partielles obtenues sont comparées aux calculs théoriques publiés, et les propriétés vibrationnelles sont en bon accord avec ces publications. De plus, la pureté des phases est caractérisée par diffraction de rayons X de haute énergie. L'arrangement atomique, rhomboédrique pour GeTe et cubique pour SnTe et PbTe , est déterminant pour la densité d'états de phonons, la structure cubique de type NaCl étant moins rigide que la structure rhomboédrique.

Dans le troisième chapitre, la dynamique de réseau dans AgSbTe_2 est étudiée par diffusion nucléaire inélastique par ^{121}Sb et ^{125}Te sur un échantillon polycristallin, à basse température. Pour cet échantillon les modes de phonons ont une énergie inférieure à 25 meV et une vitesse du son de $v_s = 1490(30)$ m/s a été mesurée. Une estimation simple de la conductivité thermique indépendante de la température dans AgSbTe_2 donne $\kappa_L = 0.50 \pm 0.05 \text{ Wm}^{-1}\text{K}^{-1}$. Nous trouvons que la faible température de Debye, $\theta_D = 150(15)$ K combinée avec la courte durée de vie moyenne des phonons et la faible vitesse du son sont les facteurs déterminants pour la faible conductivité thermique dans AgSbTe_2 et sont liés aux bonnes propriétés thermoélectriques de AgSbTe_2 et de matériaux contenant AgSbTe_2 .

Le chapitre 4 est dédié à l'étude de la structure moyenne et locale dans l'alliage $\text{AgPb}_{18}\text{SbTe}_{20}$ (LAST-18), par une combinaison d'une analyse Rietveld et de la fonction de distribution de paires. L'influence importante des conditions de synthèse sur les paramètres de réseau, et sur la composition et la concentration en nano inclusions dans LAST-18 est confirmée. De plus les densités partielles d'états de phonons de ^{121}Sb et ^{125}Te ont été obtenues par diffusion nucléaire inélastique afin de caractériser séparément la dynamique de réseau de la matrice et des nano inclusions. Une caractérisation supplémentaire des propriétés élastiques est de propriété de réseau a été réalisée par spectroscopie à résonance d'ultrasons, et par des mesures de chaleur spécifique et d'expansion thermique.

Le dernier chapitre est dédié à la technique de spectroscopie à résonance d'ultrasons, et la construction d'un système de mesures avec des tiges tampons pour les hautes températures. Les avantages et les désavantages, ainsi que les limites et les difficultés sont discutées. En utilisant le suivi de modes de résonances, le comportement mécanique de PbTe , entre 300 et 523 K, et d'un échantillon de Nb entre 300 et 973 K, a été étudié.

Kurzbeschreibung

Das Ziel dieser Arbeit ist die strukturelle und gitterdynamische Charakterisierung von Komplexchalkogenidlegierungen. Der Fokus liegt auf den Systemen $\text{AgPb}_m\text{SbTe}_{m+2}$ (LAST- m), AgSbTe_2 und den Verbindungen PbTe , SnTe und GeTe . Hierzu wurden Untersuchungen mit Synchrotronstrahlung, einschließlich hochenergetischer Röntgenstreuung und unelastischer Kernstreuung, durchgeführt und die Wärmekapazität und thermische Ausdehnung der Proben bestimmt. Darüber hinaus wurde ein neuer Aufbau zur Resonanzultraschallspektroskopie aufgebaut, der die mechanische Charakterisierung von thermoelektrischen Legierungen bei Raumtemperatur bis hin zu 1073 K erlaubt.

Das erste Kapitel fasst relevante wissenschaftliche Informationen zur Thermoelektrizität zusammen und stellt die derzeit wichtigsten thermoelektrischen Materialien vor. Ferner werden die Untersuchungsmethoden, d. h. die Wärmekapazitätsmessung, die Resonanzultraschallspektroskopie, die Röntgenstreuung und die unelastische Kernstreuung, nähergehend erläutert. Hiermit soll dem Leser ein elementares Verständnis der experimentellen Methoden und der Thematik an sich ermöglicht werden. Dieser Einführung folgen drei Kapitel zur experimentellen Untersuchung der Gitterdynamik in Chalkogenidlegierungen.

Kapitel 2 beschreibt die Gitterdynamik der Verbindungen GeTe , SnTe und PbTe mittels unelastischer ^{119}Sn und ^{125}Te Kernstreuung. Die erhaltene Partialdichte der Phononenzustände wird mit publizierten theoretischen Berechnungen verglichen und eine weitgehende Übereinstimmung der Schwingungseigenschaften festgestellt. Weiterhin werden die Phasenreinheit und die Struktur der Verbindungen durch hochenergetische Röntgenstrahlung charakterisiert. Die räumliche Anordnung der Atome, rhomboedrisch für GeTe und kubisch für SnTe und PbTe ,

beeinflusst die Zustandsdichte der Phononen: Die NaCl-Struktur besitzt verglichen mit der rhomboedrischen Struktur einen weicheren Charakter.

In Kapitel 3 wird die Gitterdynamik von polykristallinem AgSbTe_2 bei niedrigen Temperaturen mit unelastischer ^{121}Sb und ^{125}Te Kernstreuung untersucht. Die Energien der Phononenmoden lagen für diese Verbindung unterhalb von 25 meV und eine Schallgeschwindigkeit von $v_s = 1490(30)$ m/s konnte ermittelt werden. Eine einfache temperaturunabhängige Abschätzung der thermischen Leitfähigkeit des AgSbTe_2 -Gitters ergab $\kappa_L = 0.50 \pm 0.05 \text{ Wm}^{-1}\text{K}^{-1}$. Wir fanden heraus, dass diese geringe thermische Leitfähigkeit und damit die guten thermoelektrischen Eigenschaften von reinem AgSbTe_2 und AgSbTe_2 -Systemen auf die niedrige Debye Temperatur $\theta_D = 150(15)$ K, verbunden mit der kurzen Lebensdauer der Phononen und der niedrigen Schallgeschwindigkeit, zurückzuführen ist.

Kapitel 4 ist der Bulk-Untersuchung der mittleren und lokalen Struktur einer $\text{AgPb}_{18}\text{SbTe}_{20}$ (LAST-18) Legierung durch eine kombinierte Rietveld und Paarverteilungsfunktionsanalyse gewidmet. Der starke Einfluss der Synthesebedingungen auf die Gitterparameter und die Zusammensetzung und Konzentration der Nanocluster in LAST-18 werden bestätigt. Um die Gitterdynamiken der Materialmatrix und der Nanoeinschlüsse separat zu untersuchen, wurde die Partialdichte der Phononenzustände von ^{121}Sb und ^{125}Te durch unelastische Kernstreuung bestimmt. Zusätzlich wurden die elastischen und gitterdominierten Eigenschaften mittels Resonanzultraschallspektroskopie und der Messung der Wärmekapazität und der thermischen Ausdehnung ermittelt.

Im letzten Kapitel wird die Technik der Resonanzultraschallspektroskopie und der Aufbauprozess dieses *buffer-rods*-Systems für Hochtemperaturmessungen vorgestellt. Vor- und Nachteile, wie auch Limitierungen und Schwierigkeiten der Technik werden diskutiert. Unter Benutzung der “mode-tracking” Methode wird das mechanische Verhalten von PbTe und einer Niobiumprobe bei Raumtemperatur bis hin zu 523 K, beziehungsweise von Raumtemperatur bis hin zu 973 K, untersucht.

Contents

List of Figures	xiii
List of Tables	xviii
1 Introduction	1
1.1 Thermoelectricity	2
1.1.1 Chalcogenides Compounds	4
1.2 Macroscopic Measurements	9
1.2.1 Heat Capacity	9
1.2.2 Resonant Ultrasound Spectroscopy	12
1.3 X-Ray Diffraction	13
1.4 Nuclear Inelastic Scattering	17
References	20
2 Lattice dynamics and structure of GeTe, SnTe and PbTe	23
2.1 Introduction	25
2.2 Experimental	28
2.3 Results and discussion	28
2.3.1 Structural characterization	28
2.3.2 Lattice dynamics characterization	31
2.4 Conclusion	35
2.5 Acknowledgements	36
References	38

3	Lattice dynamics in AgSbTe₂	41
3.1	Introduction	43
3.2	Experimental	45
3.3	Results and discussion	46
3.3.1	Structural Characterization	46
3.3.2	Lattice Dynamics Characterization	46
3.4	Conclusion	54
3.5	Acknowledgements	54
	References	55
4	Structure and Lattice dynamics in AgPb₁₈SbTe₂₀	57
4.1	Introduction	59
4.2	Experimental	61
4.3	Results and discussion	62
4.3.1	Structural characterization	62
4.3.2	Lattice dynamics characterization	70
4.4	Conclusion	77
4.5	Acknowledgements	78
	References	79
5	Resonant Ultrasound Spectroscopy	82
5.1	Resonant Ultrasound Spectroscopy	83
5.2	Theoretical background	85
5.2.1	Linear Elasticity	86
5.3	High Temperature RUS	91
5.3.1	Design and Fabrication	92
5.3.2	Testing of the Buffer-rod Transducer System	97
	References	104
6	Conclusions and Outlook	105

List of Figures

1.1	The Transit 4A satellite, launched on June 29, 1961, was the first satellite to use a nuclear power source and radioisotope thermoelectric generator (RTG). It is shown here at the bottom of a triple-decker payload. (Image credit: John Hopkins Applied Physics Laboratory)	5
1.2	Two test rovers and a flight spare provides a graphic comparison of three generations of Mars rovers developed at NASA’s Jet Propulsion Laboratory, Pasadena, California. (Image credit: NASA/JPL-Caltech)	5
1.3	(a) The units cell for PbTe, SnTe and (b) GeTe. In the plots Te is shown in blues, Pb and Sn in red, and Ge in green. Pb/Sn and Ge are depicted as bigger spheres than Te.	6
1.4	The unit cell for $Pm\bar{3}m$ (cubic) AgSbTe ₂ . Ag is shown in orange, Sb in green and Te in red. Note the shared occupancy at position ($x = 0.5, y = 0.5, z = 0$) with stochastic distribution by Ag and Sb.	8
1.5	Ag ₂ Te-Sb ₂ Te ₃ pseudo-binary Ag-Sb-Te phase diagram (47, 48). The cubic AgSbTe ₂ phase is only stable in the region marked as δ . Below 418 K, the face-centered cubic β -Ag ₂ Te phase transforms into the monoclinic α -Ag ₂ Te phase. The ϵ phase corresponds to trigonal Sb ₂ Te ₃	8
1.6	The unit cell for $Fm\bar{3}m$ LAST-18. Pb is shown in blue, Te in red, Sb in green and Ag in orange.	9
1.7	The quasi-binary PbTe- AgSbTe ₂ phase diagram (47). The composition for obtaining LAST-10 and LAST-18 are shown by black arrows. Existing phases are identified as (α) monoclinic Ag ₂ Te, (β) face-centered cubic Ag ₂ Te and trigonal Sb ₂ Te ₃	10

LIST OF FIGURES

1.8	A schematic representation of the set up used for measuring the heat capacity of a sample with the relaxation method. From (51).	12
1.9	Conventional RUS set up for measurements at room temperature.	13
1.10	The geometry of Bragg reflection from a set of crystal planes. Incoming beams (1) and (3), and diffracted beam (2). The short-dashed lines show another possible set of atomic planes.	15
1.11	Schematic diagram of an X-ray diffractometer.	15
1.12	The experimental hall and storage ring building of the ESRF. (Courtesy: P. Ginter/ESRF)	16
1.13	Experimental set up for nuclear inelastic resonance measurement. The corresponding energy spectral is schematically shown measured by the detectors for Nuclear Forward Scattering (NFS) and Nuclear Inelastic Scattering (NIS). Figure adapted from Ref. (53).	19
2.1	(a) The units cell for PbTe, α -SnTe and (b) β -GeTe, all at 298 K. In both plots Te is depicted in blues atoms, Pb and Sn in red, and Ge in green. Pb / Sn and Ge are illustrated as larger spheres as compared to Te.	26
2.2	Room temperature X-ray diffraction patterns of PbTe, SnTe and GeTe. Red dots correspond to the experimental data, while the black line, blue line and green sticks are, respectively, the Rietveld refinement, the difference plot and the peak positions for main and secondary phases.	29
2.3	The nuclear inelastic scattering, NIS, spectra and the instrumental functions, measured by nuclear forward scattering, NFS, obtained with the ^{125}Te resonance in PbTe (top), SnTe (middle), and GeTe (bottom), and with the ^{119}Sn resonance in SnTe (middle).	32
2.4	The partial Te density of phonon states of PbTe (top), SnTe (middle) and GeTe (bottom) at 55, 60 and 30 K, respectively (solid lines). Typical error bars are given. The total DPS of SnTe by NIS is also presented (middle, in black). The lines with points are the theoretical calculations for PbTe (light blue (41) and dark blue (42)) and GeTe (violet (43)) and the total DPS of SnTe from inelastic neutron scattering data (orange (46)). The insets show the reduced partial DPS, $g(E)/E^2$, and the low energy fit, between 0 and 4 meV, for the Debye levels, indicated by the same type of lines.	33

LIST OF FIGURES

3.1	The unit cell for $Pm\bar{3}m$ AgSbTe ₂ , at 298 K. Ag is depicted in orange atoms, Sb in green and Te in red atoms.	44
3.2	X-ray diffraction pattern of AgSbTe ₂ , at room temperature. Red dots correspond to the experimental data, while the black line, blue line and green sticks are, respectively, the Rietveld refinement, the difference plot and the peak positions for AgSbTe ₂ and the secondary phase Ag _{4.5} Te ₃	47
3.3	The influence of temperature on the lattice constants of AgSbTe ₂ (top), and the corresponding thermal expansion, α (bottom).	48
3.4	Macroscopically measured (red solid line) heat capacity AgSbTe ₂ and the corresponding Debye model fit (gray). The total contribution of Ag, Sb and Te calculated from the DPS of AgSbTe ₂ , assuming that Ag contribution to the heat capacity is similar to the Sb contribution, is presented in black.	50
3.5	¹²⁵ Te-partial (top) and ¹²¹ Sb-partial DPS (bottom) for AgSbTe ₂ , at 11K (green line), 30K (red line for ¹²⁵ Te and orange line for ¹²¹ Sb) and 60K (blue line). The calculated partial DPS for Sb and Te, after Ref. (5), is presented as magenta and black lines, respectively. The arrow points the region at the experimental data with an excess of vibrational modes due the presence of the Ag _{4.5} Te ₃ phase. The reduced partial DPS $g(E)/E^2$ in units of 10^{-3}meV^{-3} , and the low-energy fit between 0.5 and 6 meV for the Debye levels, indicated by the same type of lines, are shown in the inset.	52
4.1	X-ray diffraction patterns, at room temperature, of LAST-18 samples obtained by gradient annealing method, along with those of the end-member (pure chalcogenides PbTe and AgSbTe ₂) and Sb-metal (dashed line). The samples are identified as GA-1 (Gradient annealing-1), GA-2, GA-3, GA-4 and GA-5, according to their corresponding annealing temperature of 683, 738, 778, 798 and 853 K, respectively. In the bottom image, the Sb-peak at $\sim 2.62^\circ$ is seen to decrease, until it vanishes, with increasing the annealing temperature during synthesis of LAST-18.	63
4.2	Dependence of the lattice parameter of AgPb ₁₈ SbTe ₂₀ (LAST-18) on the annealing temperature. XRD data was collected at room temperature.	66
4.3	The influence of temperature on the lattice constants of LAST-18 (top), and the corresponding thermal expansion, α (bottom).	68

4.4	(a) X-ray powder diffraction of a water quenched (WQ) LAST-18 sample; the corresponding PDF data analysis with a two-phase model (PbTe-matrix with $\text{AgPb}_2\text{SbTe}_4$) is shown in (c). (b) X-ray powder diffraction from an annealed LAST-18 sample (DLR2594, $T_{ann} = 723$ K); the corresponding PDF data analysis with a two-phase model (PbTe-matrix with $\text{AgPb}_{10}\text{SbTe}_{12}$) is shown in (d). Red line is the data, black line is the calculated curve from fitting, and the blue line in offset is their difference. In the X-ray diffraction patterns, the peak positions for main phases is depicted in green.	69
4.5	Macroscopically measured heat capacity (blue line) and the fit from the Debye model (light gray).	71
4.6	The nuclear inelastic scattering, NIS, spectra and the instrumental functions, measured by nuclear forward scattering, NFS, obtained with the ^{121}Sb (top) and ^{125}Te resonance for sample DLR2594 (bottom).	72
4.7	(a) Calculated DPS of PbTe (24) and (PbTe + 0.125 AgSbTe_2) alloy (25) and, (b) DPS of LAST-18 measured by time-of-flight (TOF) inelastic neutron scattering (25), at 7 and 300 K. (c) The element specific DPS measured with the ^{121}Sb (blue line) and ^{125}Te (green line) resonances for sample DLR2594, at 55 and 50 K, respectively. The dashed line crossing the three graphics indicate the mismatch between the energy cut-off obtained by theoretical calculations and TOF, with the NIS data.	73
4.8	The reduced partial DPS of DLR2594, $g(E)/E^2$, and the low energy fit, between 0 and 3 meV, for the Debye levels, indicated by the same type of lines. The regions marked with I and II show two possible Debye levels for the Sb contribution, that depend of the subtracting procedure of the elastic line from the inelastic scattering data for Sb in LAST-18. The shaded are between 4.2 and 8.7 meV reveals a mismatch in the acoustic region between the Sb and Te reduced DPS.	74
4.9	Comparison between the Sb DPS of LAST-18 and the Sb DPS of AgSbTe_2 (46) (top) and the partial Te DPS of LAST-18 compared to the partial DPS of PbTe (47) (bottom).	75
5.1	Classical experimental arrangement of the RUS method.	85
5.2	Stress tensor in a infinitesimal material element around a point P.	88

LIST OF FIGURES

5.3	Technical drawing of the support cage of the HT-RUS setup. The figure shows the components (discs and long alumina rods) used and their dimensions.	93
5.4	Current HT-RUS set up. The figure shows cage/transducer probes inside the quartz tube in the tube furnace, before a measurement.	96
5.5	The figure compares frequency scans obtained with the conventional room temperature setup (red line) and the newly constructed high-temperature RUS (blue line). The extra peaks, marked with (*), correspond to peaks generated by the lock-in amplifier when the amplifier is momentarily unlocked during frequency switching.	100
5.6	Modes tracking of PbTe from room temperature to 523 K. Four modes were tracked throughout the temperature range from room to 523 K. The elastic behavior of PbTe can be inferred based on this method.	101
5.7	Nb modes tracking: Six modes were tracked throughout the temperature range from room to 973 K.	102

List of Tables

2.1	PbTe, SnTe and GeTe at 298 K: Measurement conditions, refined results and reliability factors obtained by Rietveld analysis.	29
2.2	Atomic parameters and atomic displacement parameters $\langle u^2 \rangle$ of PbTe, SnTe, GeTe and the secondary phase identified in this study, at 298 K.	30
2.3	Summary of sound velocity, force constant, Lamb-Mössbauer factor, atomic displacement parameter and Debye temperature in polycrystalline PbTe, SnTe and GeTe calculated from the Te-partial DPS.	35
3.1	AgSbTe ₂ X-ray diffraction at 298 K: Refined results and reliability factors obtained by Rietveld refinement.	47
3.2	Summary of the sound velocity, force constant, Lamb-Mössbauer factor, atomic displacement parameter and Debye's temperature in polycrystalline AgSbTe ₂ calculated from the Sb- and Te-partial DPS.	51
4.1	Powder X-ray diffraction refined results and reliability factors, at room temperature, for AgPb ₁₈ SbTe ₂₀ samples annealed at different temperatures along with a water quenched sample.	65
4.2	Summary of the sound velocity v_s , force constant F^M , Lamb-Mössbauer factor f_{LM} , atomic displacement parameter $\langle u^2 \rangle$ and Debye's temperature θ_D in polycrystalline LAST-18 calculated from the Sb- and Te-partial DPS.	76
4.3	Longitudinal and transversal sound velocities and elastic properties of polycrystalline LAST-18 obtained by RUS, at room temperature.	76
5.1	Different crystal symmetries and their independent elastic constants.	89

LIST OF TABLES

5.2	Measured (f^{meas}) and calculated (f^{calc}) resonance frequencies for a PbTe sample, at room temperature, using the conventional room temperature (RT-RUS) and HT-RUS setups. A final RMS error of 0.44 and 0.22 %, respectively, were obtained for these sets of data.	99
5.3	Comparison between the elastic properties of a PbTe sample, at room temperature, probed with the conventional and HT-RUS setups.	101

Chapter 1

Introduction

Future comfortable and sustainable access to energy is currently a great challenge at the forefront of scientific research. A conjunct effort in reducing consumption, developing and implementing alternative and sustainable energy sources, improving electrical energy storage and transmission, and recovering waste heat produced by industrial processes are examples of the different approaches to respond to this challenge. Thermoelectric materials can directly contribute towards a global joint solution because they are capable of converting a thermal gradient into a voltage, and *vice-versa*, and thus to recover waste heat. Many advantages of this technology can be cited with respect to other approaches to refrigeration or power generation: compactness and quietness, scalability, no moving parts, long and reliable working life, local cooling or power generation, no need of maintenance and most important of all, the abundance of waste heat sources present in household and industrial processes. Thermoelectric technology, however, has not fulfilled its whole potential in engineering applications mainly due to the relatively low efficiency (<10%) of commercially available materials (1). In order to fully benefit from all the advantages of TE devices, an improvement in the efficiency in which the material converts heat into electricity is required.

1.1 Thermoelectricity

The appearance of an electrical current resulting from a heat flow across a thermal gradient in a material, and *vice-versa*, is known as thermoelectricity. Seebeck first noticed this effect in the early 1800's (2) while studying the relation between electricity and heat. He reported that a magnetic field was observed around the circuit when two dissimilar electrically conductive materials (*e.g.*, bismuth and copper, in one of his experiment) were joined in a closed circuit and the two junctions were kept at different temperatures. The magnetic effect was observed because of the deflection of a compass placed nearby the experimental set up. Seebeck, however, did not recognize nor report that there was an electric current involved, so he named his discovery *thermomagnetism*. The term *thermoelectricity* and a clear explanation for the phenomenon, namely the appearance of an electric voltage, was proposed only later, by Oersted (3). The voltage arises because electrons and holes in a semiconductor will diffuse inside the material in the presence of a thermal gradient between its two ends. If the temperature difference is maintained, hot carriers can diffuse to the cold side, whereas cold carriers diffuse to the hot end, similarly to a classical gas that expands when heated. An electric field across the material will result due to the charge accumulation at each end.

Conversely, when a voltage is applied to the device, a temperature difference is observed. The performance of a thermoelectric material, that means, its potential to convert heat into electricity, will depend only on the working temperature, T , and on an intrinsic material's parameter, the figure of merit Z , with unit of K^{-1} , defined as:

$$Z = \frac{S^2 \cdot \sigma}{\kappa} \quad (1.1)$$

where S is the Seebeck coefficient, σ is the electrical conductivity and κ is the total thermal conductivity ($\kappa = \kappa_E + \kappa_L$, the sum of the electronic and the lattice contribution, respectively). Z is temperature dependent, therefore, the dimensionless figure-of-merit ZT is also commonly used. The challenge in thermoelectricity is to increase the figure-of-merit, and consequently the material's efficiency by having high values of the Seebeck coefficient and electrical conductivity whereas extremely low thermal conductivity is desired. Clearly, few materials combine these rather incompatible properties. Even after many years of research, a ZT above unity has been reported just for a limited number of compounds. Good results have been obtained through optimal doping in alloys with weakly bounded heavy elements as in the case of bismuth telluride (Bi_2Te_3) and lead telluride (PbTe) (4), partly filled cage-structures such as chalcogenides (5, 6) and skutterudites (7), and by nanostructuring (8). These approaches will selectively have a greater effect on the power factor ($S^2 \cdot \sigma$) or on the thermal conductivity, κ . In the last years, nanostructuring of thermoelectric materials or the presence of nanostructures in bulk compounds have been investigated, where the increased scattering of mid to long wavelength phonons has been proven beneficial in reducing the lattice part of the thermal conductivity (8). The lattice thermal conductivity is related to the sound velocity, v_s , heat capacity, C and the phonon mean free path, L_{ph} through $\kappa_L \approx (1/3)(v_s C L_{ph})$. From a practical perspective, the use of nanostructures increase the scattering of phonon, causing interruptions of phonons with large mean free path at interfaces and boundaries, without a deleterious effect on the electrical properties since electrons have a much shorter mean free path than phonons. Based on this principle, artificial structures such as $\text{Bi}_2\text{Te}_3/\text{Sb}_2\text{Te}_3$, $\text{Bi}_2\text{Te}_3/\text{Bi}_2(\text{Se},\text{Te})_3$ (9, 10) and $\text{PbTe}/\text{PbTeSe}$ thin-film superlattices (11, 12, 13, 14) have been grown by low temperature metal-organic chemical vapor deposition or thermal evaporation-condensation technique, resulting in ZT value above 2 at 300 K. Note that this high value ZT has not entirely been independently confirmed. Natural structures were also investigated and modified through thermal processes and doping, allowing the formation of secondary phases during synthesis, *i.e.* PbTe alloys. The addition of a few

percent of AgSbTe₂ in PbTe in the compound AgPb_{*m*}SbTe_{*m*+2} (LAST-*m*) and the formation of nanostructures in the PbTe-matrix decreases the thermal conductivity of PbTe from ~ 2.2 W/mK to 0.5 W/mK, at 300 K, and a ZT of 1.4 is obtained for LAST-18 at 700 K (15, 16, 17). This work investigates the structure and lattice dynamics in complex chalcogenides such as the binaries PbTe, SnTe and GeTe, the metastable phase AgSbTe₂ with intrinsically minimal thermal conductivity (18) and AgPb_{*m*}SbTe_{*m*+2} aiming to map out the lattice dynamics properties and provide insights in the thermal conductivity in these systems.

1.1.1 Chalcogenides Compounds

Chalcogenides include a wide number of compounds where bonding between, at least, one chalcogen ion and one electropositive element occurs. The term is usually preferred for sulfides, selenides and tellurides but not for oxides. Members of these group of compounds are characterized by their air stability, high melting points and flexibility in composition. Since the early days of thermoelectric research, chalcogenides received great attention mainly due to their appropriate energy band gap for thermoelectric applications (0.1-0.8 eV) and their large Seebeck coefficient values, combined with a relatively low thermal conductivity.

1.1.1.1 PbTe, GeTe and SnTe

The binaries PbTe, SnTe and GeTe are of interest in practical applications in different fields such as infrared optoelectronics and in thermoelectric devices (19). Parallel to the research on the pure binaries, alloys, such as AgPb₁₈SbTe₂₀ (15), Pb_{0.36}Ge_{0.64}Te (20) and Pb_{0.25}Sn_{0.25}Ge_{0.5}Te (21) received also great attention in the last decade. PbTe, SnTe and GeTe based alloys are appropriate candidates for thermoelectric application, from room temperature to 773 K, due to their high carrier mobility, direct narrow band gap and relatively low thermal conductivity. PbTe is one of the oldest and most studied thermoelectric materials for power generation, since the early report of Ioffe (22) and a great number of experimental data has been accumulated in the decades of 1950 and 1960's on it. In this same period, alloys of PbTe were the materials of choice by NASA for the first radioisotope thermoelectric generator (RTG) which powered the spacecraft for the Transit 4A satellite (23), see Fig. 1.1. The current NASA's project of probing the possibility of life on Mars has switched back the attention to PbTe based alloys for powering the spacecraft and the rovers to be used on Mars surface (24) (Fig. 1.2).

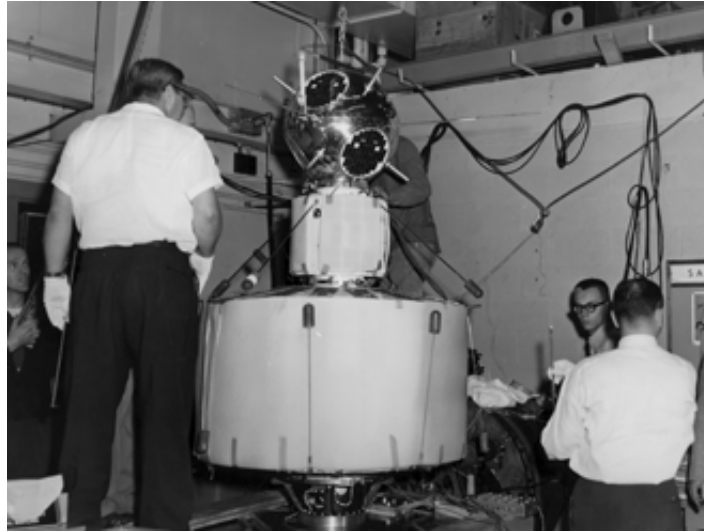


Figure 1.1: The Transit 4A satellite, launched on June 29, 1961, was the first satellite to use a nuclear power source and radioisotope thermoelectric generator (RTG). It is shown here at the bottom of a triple-decker payload. (Image credit: John Hopkins Applied Physics Laboratory)



Figure 1.2: Two test rovers and a flight spare provides a graphic comparison of three generations of Mars rovers developed at NASA's Jet Propulsion Laboratory, Pasadena, California. (Image credit: NASA/JPL-Caltech)

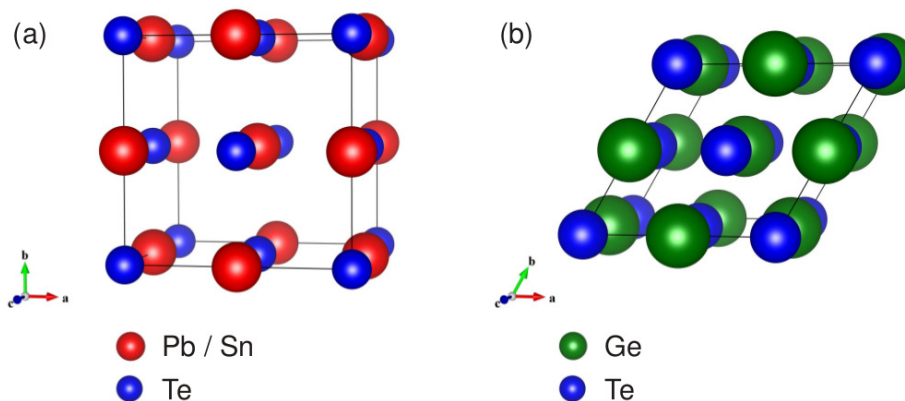


Figure 1.3: (a) The units cell for PbTe, SnTe and (b) GeTe. In the plots Te is shown in blues, Pb and Sn in red, and Ge in green. Pb/Sn and Ge are depicted as bigger spheres than Te.

The relatively low thermal conductivity of PbTe, 2.2 W/mK at room temperature, combined to its excellent electronic properties are key parameters for the interesting thermoelectric efficiency in this material, resulting in a maximum ZT between 0.8-1.0 at 700 K (25). By doping PbTe ($A_x\text{Pb}_{1-x}\text{Te}$, $A = \text{Sn, Tl or I}$ and $0.01 \leq x \leq 0.02$), an enhancement larger than 50% in the the figure of merit, with $ZT \sim 1.5$ at 773 K (26, 27), as compared to pure PbTe, was reported. Nanostructuring in PbTe-based materials can be obtained by precipitation of a fine secondary phase of a metastable supersaturated solid solution via nucleation and growth processes and/or the decomposition of an instable solid solution via spinodal decomposition mechanisms and have been reported for systems such as (Pb,Ge)Te alloys (28), TAGS (Te-Ag-Ge-Sb, GeTe alloy with 15% AgSbTe_2) (1, 29) and LAST (Pb-Sb-Ag-Te, $\text{AgPb}_m\text{SbTe}_{m+2}$) (15, 16).

PbTe and SnTe are closely related. Lead telluride is a semiconductor which crystallizes in the NaCl-structure ($\text{Fm}\bar{3}\text{m}$ group) with lattice constant $a = 6.460(1) \text{ \AA}$ (25), as seen in Fig. 3.1(a). By appropriate doping, either n- or p-type semiconductor can be obtained. At room temperature, SnTe crystallizes in the same crystal structure as PbTe, with slightly lower lattice parameter $a = 6.312 \text{ \AA}$ (30), $ZT \sim 1.5$ at 773 K (26, 27), with medium doping level. Below 100 K, the cubic symmetry is reduced to a rock salt-like equilibrium structure, α -SnTe, via a distortion along the (111) direction (31, 32, 33). Similarly, GeTe also crystallizes in the rocksalt structure at temperatures above $T_c \approx 700 \text{ K}$ (34) - β -GeTe phase, with lattice parameters $a = 6.020 \text{ \AA}$ (35). Below T_c , a rhombohedral structure, α -GeTe, is stabilized,

with $a=b=4.1719 \text{ \AA}$ and $c=10.710 \text{ \AA}$ (36, 37), see Fig. 3.1(b). GeTe presents a thermal conductivity of $2.6 \text{ Wm}^{-1}\text{K}^{-1}$, at 298 K, (38) and compared to PbTe and SnTe, has a larger thermoelectric figure of merit (39). Yet GeTe shows low structural and chemical stability, due to its high sublimation rate and low-temperature phase transition (40).

1.1.1.2 AgSbTe₂

AgSbTe₂ crystallizes in a rock-salt cubic structure where the Ag and Sb atoms occupy the Na site, whereas Te is located at the Cl position. Due to its very low lattice thermal conductivity of $0.65 \pm 0.05 \text{ W}\cdot\text{m}^{-1}\text{K}^{-1}$ (18), applications of AgSbTe₂ are mainly related to their thermoelectric (18, 41, 42) and optical phase-change properties (43, 44). The origin of low thermal conductivity in such compounds is related to their atomic and electronic structures which are responsible for the material's transport properties. Highly anharmonic chemical bonds (18) and compositional fluctuations across the material can also contribute to decrease the thermal conductivity by adding Umklapp, disorder and phonon-phonon scattering to the system. The atomic structure of AgSbTe₂ was investigated by different groups, and the possible existence of Ag-Sb ordering (42, 45, 46) was suggested. An ordering model however could not be fully established because according to the Ag₂Te-Sb₂Te₃ pseudo-binary Ag-Sb-Te phase diagram (47, 48), AgSbTe₂ decomposes into Sb₂Te₃ and Ag₂Te below 630 K, depending on the synthesis conditions, which indicates the structural complexity of such alloys, see Fig.1.5. In order to prevent this potential decomposition, AgSbTe₂ can be rapidly cooled from the melt through a quenching process. Alternatively, AgSbTe₂ is added to other thermoelectric alloys such as GeTe and PbTe and favors the formation of nanoinclusions in composite materials with increased thermoelectric efficiency, such as TAGS, (GeTe)_{0.85}(AgSbTe₂)_{0.15} (1), and LAST- m AgPb _{m} SbTe _{$2+m$} (15). In order to clarify the ZT improvement due to nanocrystalline precipitates in the latter materials, a better understanding of the underlying microscopic mechanisms responsible for the low thermal conductivity in AgSbTe₂ is desirable.

1.1.1.3 AgPb _{m} SbTe _{$m+2$} (LAST- m)

AgPb _{m} SbTe _{$m+2$} (LAST- m) derives from the combination of PbTe and AgSbTe₂ and it is a promising bulk material for thermoelectric applications at mid-range temperatures (500-700 K). In this material, nanostructures are formed naturally during cooling from the melt, via spinodal decomposition and/or nucleation and growth. High figure of merit $Z \sim 1.7$ to 2.2 were reported (15, 16, 17). The properties can be tuned by optimizing the doping of

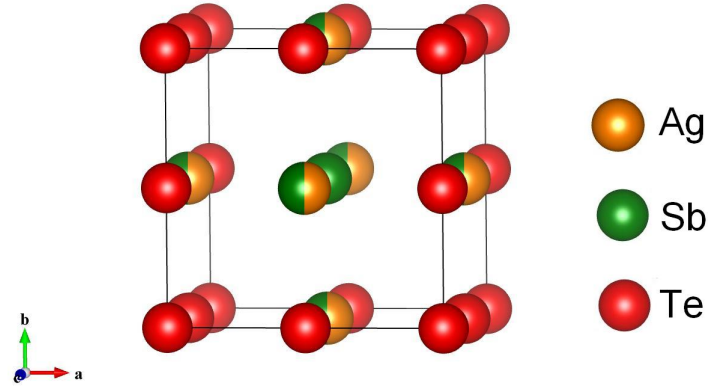


Figure 1.4: The unit cell for $Pm\bar{3}m$ (cubic) AgSbTe_2 . Ag is shown in orange, Sb in green and Te in red. Note the shared occupancy at position $(x=0.5, y=0.5, z=0)$ with stochastic distribution by Ag and Sb.

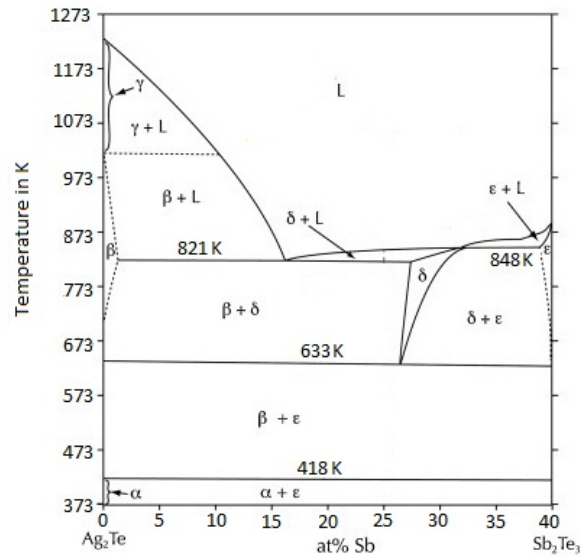


Figure 1.5: Ag_2Te - Sb_2Te_3 pseudo-binary Ag-Sb-Te phase diagram (47, 48). The cubic AgSbTe_2 phase is only stable in the region marked as δ . Below 418 K, the face-centered cubic β - Ag_2Te phase transforms into the monoclinic α - Ag_2Te phase. The ϵ phase corresponds to trigonal Sb_2Te_3 .

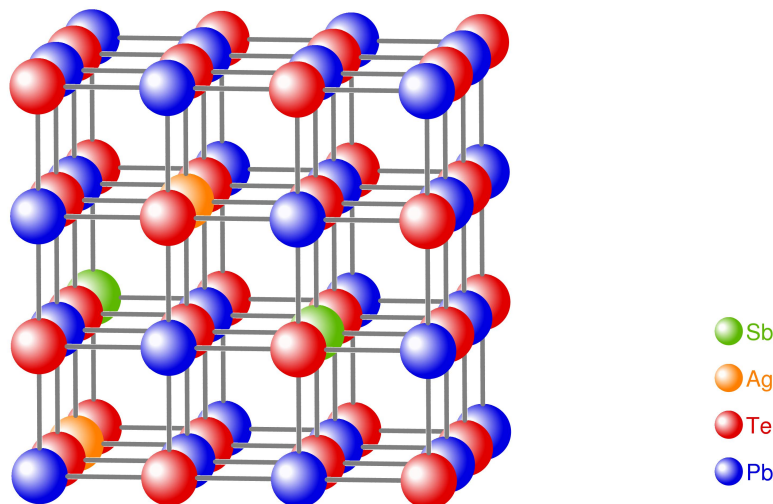


Figure 1.6: The unit cell for $Fm\bar{3}m$ LAST-18. Pb is shown in blue, Te in red, Sb in green and Ag in orange.

Ag, Sb and Pb fractions. LAST- m crystallizes in a cubic NaCl structure (same structure as PbTe), where the cations Ag, Pb and Sb occupy the Na site, whereas Te is located at the anionic position. The flexibility in composition, and consequently, the ability of tailoring the final properties, is reached by varying $(1/m)$ amount of AgSbTe_2 . The higher the m value, the lower the AgSbTe_2 content in the final LAST composition. The presence of nanostructures and the compositional fluctuation in the matrix introduce inhomogeneity on the atomic and nanoscale that greatly reduce the thermal conductivity and thus the thermoelectric quality of the materials increases significantly, as compared to PbTe (16). Additionally, this system presents a complex phase diagram (Fig. 1.7), and the final properties are also strongly sensitive to the synthesis conditions (15, 49, 50).

1.2 Macroscopic Measurements

1.2.1 Heat Capacity

Heat capacity relates the amount of energy (*i.e.*, *heat*) required to raise the temperature of a body by a given amount. In a material with large heat capacity, a large amount of supplied energy causes only a small temperature increase. The specific heat capacity of a substance is the heat capacity per unit volume, in units of joules per m^3 (or mol) per degree Kelvin. The

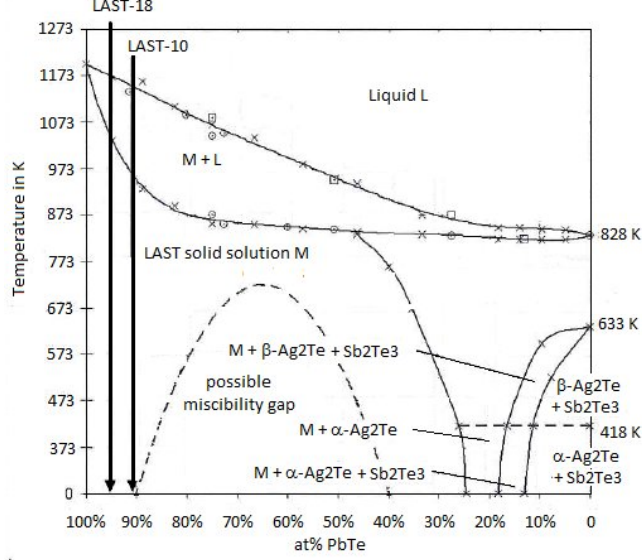


Figure 1.7: The quasi-binary PbTe-AgSbTe₂ phase diagram (47). The composition for obtaining LAST-10 and LAST-18 are shown by black arrows. Existing phases are identified as (α) monoclinic Ag₂Te, (β) face-centered cubic Ag₂Te and trigonal Sb₂Te₃.

heat capacity of polycrystalline chalcogenides samples have been measured in a Quantum Design Physical Properties Measurement System (PPMS) (51). A schematic representation of the set up used for measuring heat capacity is shown in Fig. 1.8. The sample is placed on the measuring platform. To assure thermal contact between sample and platform, a thin layer of grease is normally used. The platform and puck are thermally contacted by 8 wires of a known conductance, G_w . Additionally, a thermometer and a heater are fixed on the base of the platform. During a measurement, the entire set up is placed within an evacuated chamber. Then, a heat pulse of constant power, P_0 , is applied from the heater for over a period of time. A cooling time of same duration follows the heating. For thermal equilibrium conditions between sample and platform at temperature T , the total heat capacity, C , of both components is given by

$$C \frac{dT}{dt} = -K_w(T - T_p) + P(t), \quad (1.2)$$

where T_p is the puck temperature, $P(t) = P_0$ during heating and $P(t) = 0$ during cooling and K_w is the thermal conductivity of the wires. As the temperature approaches equilibrium after a period of time t on heating, it can be described as

$$T(t) = T(0)(1 + \Delta T(1 - \exp(-t/\tau))) \quad (1.3)$$

with $\Delta T = P_0/G_w$. Heat capacity can therefore be deduced by observing the relaxation of the sample temperature.

Heat capacity measurements were performed from 300 to 3 K. The heat capacity of the grease-covered platform (without sample), $C_{addenda}(T)$ is measured as a function of temperature prior to the measurement of the heat capacity of a sample plus platform, $C_{total}(T)$. The heat capacity of the sample is the difference of these two measurements $C_{sample}(T) = C_{total}(T) - C_{addenda}(T)$.

The lattice dynamics of materials can be macroscopically probed by measuring the heat capacity. In the simplest model, it is assumed that each atom vibrates independently of the others. The total heat capacity is then simply the sum of all atomic contributions, and independent of temperature, resulting in $C_v = 3R = 24.94 \text{ JK}^{-1}\text{mol}^{-1}$, where R is the gas constant, $8.3145 \text{ JK}^{-1}\text{mol}^{-1}$. This description works for most solids at temperatures well above the Debye temperature of the solid, θ_D , but fails in describing the heat capacity at low temperatures. In the Einstein model, each atom vibrates like a simple harmonic oscillator. All the atoms are vibrating independently with the same frequency, so that their energy levels, E , are expressed as

$$E = \left(n + \frac{1}{2}\right) h\nu, \quad (1.4)$$

where n is an integer quantum number, h is Planck's constant, and ν is the vibration frequency. For an harmonic motion, the frequency ν is dependent on the mass of the atoms and the force constants, *i.e.* bonding between the atoms. With this assumption, an improvement from the classical model is observed, however experimental data could not still be precisely described at low temperature. This model is a good approximation for the optical phonon branches, however it is over simplified. In a real crystal, interactions between atoms are strong enough that they will inevitably affect their neighbors (52). At low temperatures, phonons with large energy can not be excited. Therefore, only low energy phonons can be created which are due to acoustic branches near $\mathbf{k} = 0$, *i.e.*, long acoustic waves. For these phonons, it turns out that the Debye model accounts for their collective motion throughout the crystal, via chemical bonding. The wavelength, frequency and energy of vibrations are

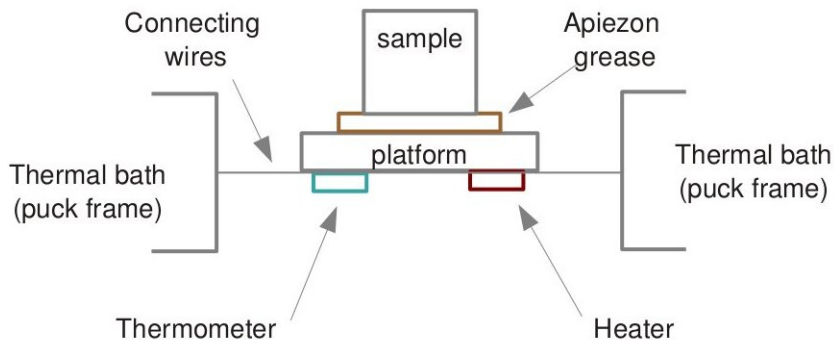


Figure 1.8: A schematic representation of the set up used for measuring the heat capacity of a sample with the relaxation method. From (51).

quantized, as they must fit into the dimensions of the solid, and the heat capacity calculated by Debye is given by

$$C_v = 9R \left(\frac{T}{\theta_D} \right)^3 \int_0^{\theta_D/T} \frac{x^4 e^x}{e^x - 1} dx, \quad (1.5)$$

with $x = h\nu/k_B T$, $\theta_D = h\nu_D/k_B$, where θ_D is called the Debye temperature, ν_D is the Debye frequency, R is the gas constant, and T is the temperature. At temperatures well below the Debye temperature, C_v is given by

$$C_v = \frac{12\pi^4}{5} R \left(\frac{T}{\theta_D} \right)^3. \quad (1.6)$$

The Debye approximation yields a good insight in the acoustic phonons of a material, *i.e.*, the collective motion of atoms in the solid. Similarly, due to its assumption of independent atomic vibration, the Einstein model probes a general picture of the optical phonons behavior.

1.2.2 Resonant Ultrasound Spectroscopy

Resonant Ultrasound Spectroscopy is a method which aims at studying mechanical properties (elastic moduli) and the sound velocity of an elastic body from its normal modes of vibration. It is based on the principle that a body resonates when an external vibrational excitation matches one of its natural frequencies of vibration. The elastic response of the materials can be inferred from its vibrational spectra when the mass and dimensions and estimated values for the elastic constants of the sample are known. For a frequency scan, a properly prepared sample, normally a rectangular parallelepiped, is placed between two transducers,

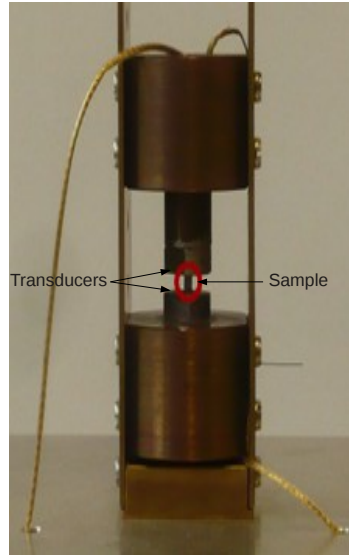


Figure 1.9: Conventional RUS set up for measurements at room temperature.

one of which is the drive frequency emitter whereas the second detects the response of the sample. The resonance spectrum is recorded and, in principle, all elastic constants can be acquired from a single, accurate measurement of this spectrum. The elastic moduli are obtained by least square fitting of the frequencies to a simple finite element mode. By evaluating a large number of resonance frequencies, it is possible to obtain the bulk and shear moduli, Poisson's ratio and sound velocity. This technique is described in more details in Chapter 5.

1.3 X-Ray Diffraction

Diffraction is a physical phenomenon and an experimental method for determining the crystal structure of materials, *i.e.*, how the atoms are arranged in the crystalline state, their inter-atomic distances and bonding angles. If an incoming beam with wavelength similar to that of the spacing of atoms (such as X-rays, neutrons, electrons) impinges on matter, the incident radiation is diffracted from the successive planes of atoms in the sample. By analyzing the spatial distribution of the diffracted intensity, a map of the reciprocal lattice of the crystal is obtained and the structure of the material can be inferred. From a diffraction experiment,

one can determine lattice parameters, the presence of residual strain, particle or grain size, phase composition and homogeneity, preferred orientation (in the case of textured materials), order-disorder transitions and thermal expansion. The thickness of thin films and multilayered systems can also be obtained, for a special diffraction geometry. X-ray diffraction is the most common technique used for structure determination, but diffraction of electrons and neutrons is also important, since these can reveal features that are not readily observed with X-rays, for example, the detection of light elements such as oxygen and or hydrogen in combination with heavy atoms. X-ray diffraction can be carried out on single crystals of a material or microcrystalline powdered samples. It also allows fast, non-destructive analysis of multi-component mixtures with rather simple sample preparation. Furthermore, high precision and accuracy in the measurement of interplanar spacings (in the order of fractions of Å) is achievable. *In-situ* measurements with dependence on temperature, electric field, pressure and deformation can also be performed. By considering two or more atomic planes in a crystal structure, diffraction occurs when scattering in a certain direction is in phase with scattered rays from other atomic planes and constructive interference takes place. The position of a diffracted beam depends only on the interplanar spacing d_{hkl} , and the wavelength of the used X-rays. From geometric considerations, Bragg's Law correlates these quantities (see Fig 1.10):

$$n\lambda = 2d_{hkl}\sin\theta, \quad (1.7)$$

where n is an integer (order of diffraction), λ is the wavelength of the X-ray radiation, d_{hkl} is the interplanar spacing of the hkl planes and θ is the diffraction angle (angle between the incoming beam and crystalline plan). For a cubic crystal, the relation between the interplanar distance and the Miller indices h, k, l is simplified and given by:

$$d_{hkl} = \frac{a}{\sqrt{h^2 + k^2 + l^2}}, \quad (1.8)$$

where a is the cubic unit cell lattice parameter. Distinct parameters affect the diffracted intensities from a X-ray experiment, including the number of electrons per atom, the spatial distribution of atoms considering the various planes of a crystalline structure and the different densities of atoms or electrons per plane.

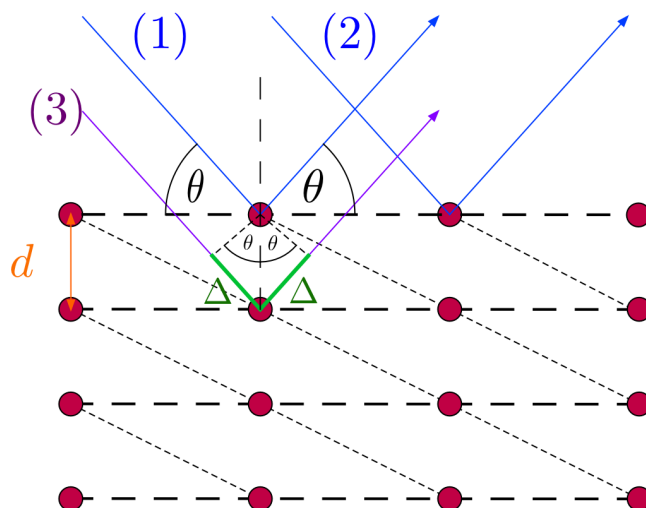


Figure 1.10: The geometry of Bragg reflection from a set of crystal planes. Incoming beams (1) and (3), and diffracted beam (2). The short-dashed lines show another possible set of atomic planes.

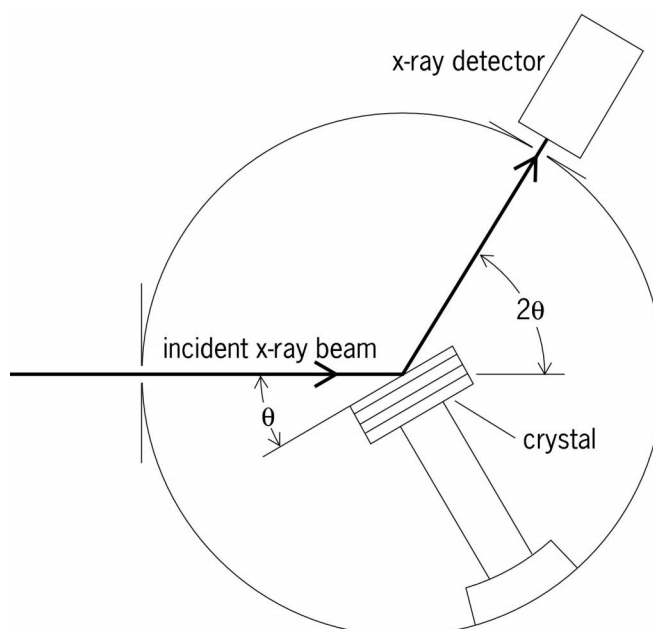


Figure 1.11: Schematic diagram of an X-ray diffractometer.



Figure 1.12: The experimental hall and storage ring building of the ESRF. (Courtesy: P. Ginter/ESRF)

X-rays sources X-rays are electromagnetic radiation with much shorter wavelength than light, between 10^{-11} and 10^{-8} m and correspond to energies in the range of 100 keV to 100 eV. Two different approaches can be used to produce X-rays (1) by decelerating electrically charged particles, commonly used in laboratory systems X-ray production where radiation (*Bremsstrahlung* and X-rays) results from bombarding a metallic target with electrons and (2) by tangentially accelerating highly energetic charged particles in magnetic fields, as in the case of synchrotron radiation facilities. A schematic view of the geometrical arrangement of a conventional X-ray diffractometer is presented in Fig. 1.11. The X-ray diffractometer comprises a source of monochromatic radiation and an X-ray detector situated on the circumference of a graduated circle centered on the powder specimen. Slits, located between the X-ray source and the specimen, and located between the specimen and the detector, limit the scattered (non-diffracted) radiation, reduce background noise, and collimate the radiation. The detector and specimen holder are mechanically coupled with a goniometer so that a rotation of the detector through 2θ degrees occurs in conjunction with the rotation of the specimen through θ degrees.

By contrast, in a synchrotron radiation facility the production of X-rays depends on different processes of bending, beam focusing, and acceleration, that are separated into different components arranged inside a large storage ring (*i.e.*, the European Synchrotron Radiation Facility in France, see Fig. 1.12).

Synchrotron radiation characteristically is highly polarized and pulsed. Its intensity and frequency are directly related to the strength of the magnetic field and the energy of the charged particles affected by the field. Accordingly, the stronger the magnetic field and the higher the energy of the particles, the greater the intensity and frequency of the emitted radiation. The most important advantage of synchrotron radiation over a laboratory X-ray source is its brilliance. The brilliance is the number of photons emitted within a certain wavelength interval per unit of source size and per unit of solid angle. It essentially limits the number of photons that can be focused in a defined spot and describes both the brightness and the angular spread of the beam. Moreover, it can not be improved by optics. A synchrotron source like the ESRF has a brilliance that is more than a billion times higher than a laboratory source. The difference between the two sources can be likened to the difference between a laser beam and a light bulb. Higher brilliance lets us see more detail in the material under study e.g. there is a greater precision in the diffraction of light from a crystal where both the angle and the intensity is significant and recorded by a detector.

1.4 Nuclear Inelastic Scattering

The density of phonon states (DPS), $g(E)$, describes the number of phonon modes in certain energy range directionally averaged over the Brillouin zone. The investigation of the DPS allows deeper insight to the lattice dynamics of materials and other important lattice related properties such as such elastic behavior, specific heat, force constant and Debye temperature. The nuclear inelastic scattering (NIS) technique (53) was employed in order to investigate the lattice dynamics of our chalcogenide systems. This technique is isotope-specific and gives direct access to the partial phonon density of states of atoms that possess a nuclear resonant level, such as ^{119}Sn , ^{121}Sb and ^{125}Te isotopes. Therefore, by using NIS, it is possible to obtain an in-depth understanding of the element-specific dynamic properties of chalcogenides materials. The experimental DPS characterization is also interesting to verify the accuracy of theoretical calculations of the partial DPS from one atom type. With this technique, beside obtaining the isotope-specific DPS itself, it is possible to determine the sound velocity of the sample, the Debye temperature, the Lamb-Mössbauer factor, the vibrational contributions to the Helmholtz free energy, specific heat, internal energy and atomic displacement parameters directly from the phonon density of states (53). Advantages of the technique include its precision, relatively short measurement time, and the small amount of material required,

which might be used in different aggregate states. By varying the sample environment, measurements can be performed at high pressure, low/high temperature, external magnetic field and ultra high vacuum conditions. NIS using synchrotron radiation with high brilliance, is based on the Mössbauer effect, *i.e.* recoil-free gamma-ray resonance absorption. In the process of emission or absorption of a gamma ray by a nucleus, some energy can be lost as recoil energy, in quantized lattice vibrations called phonons. If no phonons are involved, a "recoil-free" event occurs and conservation of momentum is achieved, without energy loss. The Mössbauer effect describes that when there is a strong bonding of the atomic nucleus to the lattice, the gamma radiation emitted by the nuclei are recoil-free, and resonant absorption may occur. With decreasing temperature the recoil free processes become more and more probable. The Lamb-Mössbauer-factor f_{LM} represents the fraction of the recoil free transitions over the total number of transitions and is related to the wavevector k of the resonant photon and mean-square displacement $\langle u^2 \rangle$ by $f_{LM} = \exp(-\vec{k}^2 \langle u^2 \rangle)$. The f_{LM} is analogous to the Debye-Waller factor, which gives the attenuation of X-ray scattering or coherent neutron scattering due thermal motion. In principle, NIS can be applied for all Mössbauer isotopes. In practice, tuning the synchrotron radiation to proper energy values for each specific resonance energy requires the use of appropriate high-resolution X-rays monochromator, which are still in development. Additionally, the characteristic average lifetime of the excited state of the probed nucleus before it decays must be long enough to be detected separately from the prompt electronic and nuclear fluorescence scattering. At last, the recoil energy should not be too large (≤ 40 keV) in order to avoid multiphonon contributions. For the chalcogenide systems of interest, measurements with the ^{125}Te , ^{121}Sb and ^{119}Sn were performed, at the resonance energy of $E_{\gamma}^{Te} = 35.49$ keV (54, 55), $E_{\gamma}^{Sb} = 37.13$ keV (56) and $E_{\gamma}^{Sn} = 23.88$ keV (55), respectively. The experimental set up is schematically shown in Fig. 1.13. The incoming X-rays beam impinges on the high-heat load monochromator, with a bandwidth of ~ 100 eV. After the high-heat-load monochromator, the energy of the photon beam has a bandwidth in the eV range. Part of this radiation is backscattered to a high-resolution monochromator, which monochromatizes the beam to a bandwidth of ~ 1 meV. This is the experimental resolution. The fine tuned radiation hits the sample, and the scattered radiation and fluorescence are collected by avalanche photodiode X-rays detectors. The time resolution of the detectors is used to discriminate the prompt Compton, and Thomson scattering and electronic fluorescence. The nuclear forward scattering (NFS, *i.e.*, elastic scattering) represents the instrumental function of the measurement and is detected

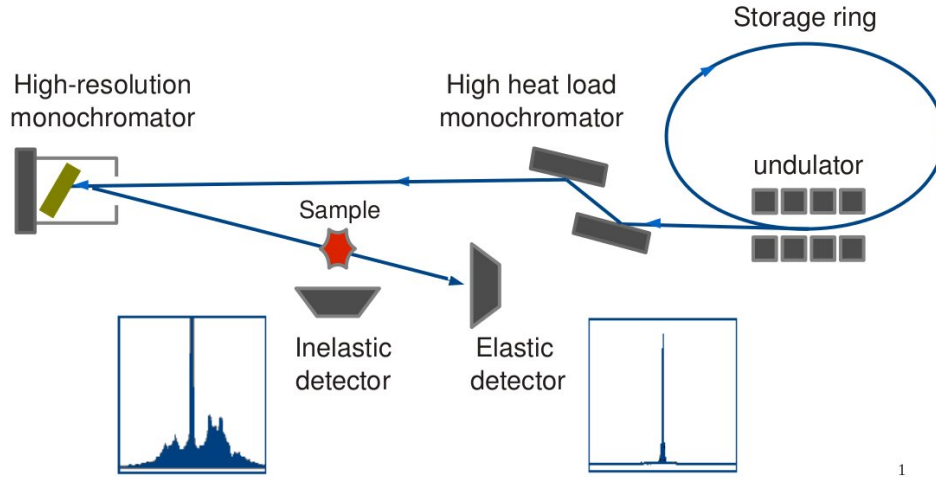


Figure 1.13: Experimental set up for nuclear inelastic resonance measurement. The corresponding energy spectral is schematically shown measured by the detectors for Nuclear Forward Scattering (NFS) and Nuclear Inelastic Scattering (NIS). Figure adapted from Ref. (53).

'far' from the sample by the elastic detector. The nuclear inelastic detector is placed very close to the sample and detects the inelastic scattering. The data treatment procedure to extract the DPS from the inelastic scattering data includes the subtraction of the elastic peak and the correction of the multiphonon contribution to the inelastic scattering (57), and the deconvolution of the data by the experimental instrumental function. The measurements are usually done at low temperatures in order to avoid excessive multiphonon contributions. From the element specific density of phonon states the sound velocity, the element specific Debye temperature, the mean force constants and atomic mean displacements can be obtained, see Chapter 2, 3 and 4.

References

- [1] D. M. ROWE, editor. *CRC Handbook of Thermoelectrics: Macro to Nano*. CRC Press, 1995. 2, 6, 7
- [2] T. J. SEEBECK. **Ueber die magnetische Polarisation der Metalle und Erze durch Temperaturdifferenz**. *Annalen der Physik*, **82**(3):253–286, 1826. 2
- [3] H. C. OERSTED. *Experimenta circa effectum conflictus electrici in acum magneticam*. Schultzeianis, 1820. 2
- [4] G. S. NOLAS, J. POON, AND M. KANATZIDIS. **Recent developments in bulk thermoelectric materials**. *MRS Bulletin*, **31**:199–205, 2006. 3
- [5] V. L. KUZNETSOV, L. A. KUZNETSOVA, A. E. KALIAZIN, AND D. M. ROWE. **Preparation and thermoelectric properties of A8IIB16IIIB30 clathrate compounds**. *J. of Appl. Phys.*, **87**:7871–7875, 2000. 3
- [6] A. SARAMAT, G. SVENSSON, A. E. C. PALMQVIST, C. STIEWE, E. MUELLER, D. PLATZEK, S. G. K. WILLIAMS, D. M. ROWE, J. D. BRYAN, AND G. D. STUCKY. **Large thermoelectric figure of merit at high temperature in Czochralski-grown clathrate Ba8Ga16Ge30**. *J. of Appl. Phys.*, **99**:023708–023714, 2006. 3
- [7] X. TANG, Q. ZHANG, L. CHEN, T. GOTO, AND T. HIRAI. **Synthesis and thermoelectric properties of p-type- and n-type-filled skutterudite R[sub y]M[sub x]Co[sub 4 - x]Sb[sub 12](R:Ce,Ba,Y;M:Fe,Ni)**. *J. of Appl. Phys.*, **97**(9):093712, 2005. 3
- [8] L. D. HICKS AND M. S. DRESSELHAUS. **Effect of quantum-well structures on the thermoelectric figure of merit**. *Phys. Rev. B*, **47**(19):12727–12731, 1993. 3
- [9] R. VENKATASUBRAMANIAN, E. SILVOLA, T. COLPITTS, AND B. O’QUINN. **Thin-film thermoelectric devices with high room-temperature figures of merit**. *Nature*, **413**:597–602, 2001. 3
- [10] J. C. CAYLOR, K. COONLEY, J. STUART, T. COLPITTS, AND R. VENKATASUBRAMANIAN. **Enhanced thermoelectric performance in PbTe-based superlattice structures from reduction of lattice thermal conductivity**. *Appl. Phys. Lett.*, **87**(2):023105, 2005. 3
- [11] T. C. HARMAN, P. J. TAYLOR, M. P. WALSH, AND B. E. LAForge. **Quantum dot superlattice thermoelectric materials and devices**. *Science*, **297**(5590):2229–2232, 2002. 3
- [12] H. BEYER, J. NURNUS, H. BÖTTNER, A. LAMBRECHT, T. ROCH, AND G. BAUER. **PbTe based superlattice structures with high thermoelectric efficiency**. *Appl. Phys. Lett.*, **80**:1216, 2002. 3
- [13] T. C. HARMAN, M. P. WALSH, B. E. LAForge, AND G. W. TURNER. **Nanostructured thermoelectric materials**. *J. of Electr. Mat.*, **34**:L19–L22, 2005. 3
- [14] J. R. SOOTSMAN, R. J. PCIONEK, H. KONG, C. UHER, AND M. G. KANATZIDIS. **Strong reduction of thermal conductivity in nanostructured PbTe prepared by matrix encapsulation**. *Chem. of Mater.*, **18**:4993–4995, 2006. 3
- [15] K. F. HSU, S. LOO, F. GUO, W. CHEN, J. S. DYCK, C. UHER, T. HOGAN, E. K. POLYCHRONIADIS, AND M. G. KANATZIDIS. **Cubic AgPbmSbTe2+m: bulk thermoelectric materials with high figure of merit**. *Science*, **303**(5659):818–821, 2004. 4, 6, 7, 9
- [16] M. ZHOU, J.-F. LI, AND T. KITA. **Nanostructured AgPbmSbTe2+m system bulk materials with enhanced thermoelectric performance**. *J. Am. Chem. Soc.*, **130**(13):4527–4532, 2008. 4, 6, 7, 9
- [17] H. WANG, J.-F. LI, C.-W. NAN, M. ZHOU, W. LIU, B.-P. ZHANG, AND T. KITA. **High-performance Ag0.8Pb18SbTe20 thermoelectric bulk materials fabricated by mechanical alloying and spark plasma sintering**. *Appl. Phys. Lett.*, **88**(9):092104, 2006. 4, 7
- [18] D. T. MORELLI, V. JOVOVIC, AND J. P. HEREMANS. **Intrinsically minimal thermal conductivity in cubic I-V-VI2 semiconductors**. *Phys. Rev. Lett.*, **101**:035901, 2008. 4, 7

REFERENCES

- [19] C. M. I. OKOYE. **Electronic and optical properties of SnTe and GeTe.** *J. of Phys.: Cond. Matt.*, **14**:8625, 2002. 4
- [20] S. GORSSE, P. BAUER PEREIRA, R. DECOURT, AND E. SELLIER. **Microstructure engineering design for thermoelectric materials: an approach to minimize thermal diffusivity.** *Chem. Mater.*, **20**(3):988–993, 2010. 4
- [21] Y. ROSENBERG, Y. GELBSTEIN, AND M. P. DARIEL. **Phase separation and thermoelectric properties of the Pb_{0.25}Sn_{0.25}Ge_{0.5}Te compound.** *J. of Alloys and Comp.*, **526**:31–38, 2012. 4
- [22] A. F. IOFFE. *Semiconductor Thermoelements and Thermoelectric Cooling.* Infosearch Ltd, 1957. 4
- [23] J. YANG AND T. CAILLAT. **Thermoelectric materials for space and automotive power generation.** *MRS Bulletin*, pages 224–229, 2006. 4
- [24] W. BRITTAIN. **Application of PbTe-TAGS CPA thermoelectric module technology in RTGs for Mars surface missions.** *AIP Conf. Proc.*, **246**:743–748, 1992. 4
- [25] Z. DUGHAIISH. **Lead telluride as a thermoelectric material for thermoelectric power generation.** *Phys. B: Cond. Matt.*, **322**:205–223, 2002. 6
- [26] J. P. HEREMANS, V. JOVOVIC, E. S. TOBERER, A. SARAMAT, K. KUROSAKI, A. CHAROENPHAKDEE, S. YAMANAKA, AND G. J. SNYDER. **Enhancement of thermoelectric efficiency in PbTe by distortion of the electronic density of states.** *Science*, **321**:554–557, 2008. 6
- [27] A. D. LALONDE, Y. PEI, AND G. J. SNYDER. **Reevaluation of PbTe(1-x)I(x) as high performance n-type thermoelectric material.** *Energy Environ. Sci.*, **4**:2090–2096, 2011. 6
- [28] S. GORSSE, P. BELLANGER, Y. BRECHET, E. SELLIER, A. UMARJI, U. AIL, AND R. DECOURT. **Nanostructuring via solid state transformation as a strategy for improving the thermoelectric efficiency of PbTe alloys.** *Acta Mater.*, **59**:7425–7437, 2011. 6
- [29] S. K. PLACHEOVA. **Thermoelectric figure of merit of the system (GeTe)_{1-x}(AgSbTe₂)_x.** *Phys. Status Solidi A*, **83**:349–355, 1984. 6
- [30] I. LEFEBVRE, M. A. SZYMANSKI, J. O. FOURCADE, AND J. C. JUMAS. **Electronic structure of tin monochalcogenides from SnO to SnTe.** *Phys. Rev. B*, **58**:1896–1906, 1998. 6
- [31] J. E. LEWIS AND J. C. LASJAUNIAS. **Specific heat and resistivity of the GeTe-SnTe alloy system.** *Philos. Mag.*, **32**(4):687–696, 1975. 6
- [32] O. VALASSIADES AND N. A. ECONOMOU. **On the phase transformation of SnTe.** *Phys. Status Solidi A*, **30**:187–195, 1975. 6
- [33] E. K. H. SALJE, D. J. SAFARIK, K. A. MODIC, J. E. GUBERNATIS, J. C. COOLEY, R. D. TAYLOR, B. MIHAILA, A. SAXENA, T. LOOKMAN, J. L. SMITH, R. A. FISHER, M. PASTERNAK, C. P. OPEIL, T. SIEGRIST, P. B. LITTLEWOOD, AND J. C. LASHLEY. **Tin telluride - a weakly co-elastic metal.** *Phys. Rev. B*, **82**:184112, 2010. 6
- [34] K. M. RABE AND J. D. JOANNOPOULOS. **Structural properties of GeTe at T=0.** *Phys. Rev. B*, **36**:3319–3324, 1987. 6
- [35] H. WIEDEMEIER AND P. A. SIEMERS. **The thermal expansion of GeS and GeTe.** *Z. Anorg. Allg. Chem.*, **431**:299–304, 2004. 6
- [36] J. GOLDAK, C. S. BARRETT, D. INNES, AND W. YOUDELIS. **Structure of alpha GeTe.** *J. Chem. Phys.*, **44**:3323, 1966. 7
- [37] T. NONAKA, G. OHBAYASHI, Y. TORIUMI, Y. MORI, AND H. HASHIMOTO. **Crystal structure of GeTe and Ge₂Sb₂Te₅ meta-stable phase.** *Thin Solid Films*, **370**:258–261, 2000. 7
- [38] J. M. YANEZ-LIMON, J. GONZALEZ-HERNANDEZ, J. J. ALVARADO-GIL, I. DELGADILLO, AND H. VARGAS. **Thermal and electrical properties of the Ge:Sb:Te system by photoacoustic and Hall measurements.** *Phys. Rev. B*, **52**:16321–16324, 1995. 7
- [39] Y. GELBSTEIN, O. BEN-YEHUDA, E. PINHAS, T. EDREI, Y. SADIA, Z. DASHEVSKY, AND M. P. DARIEL. **Thermoelectric properties of (Pb,Sn,Ge)Te-based alloys.** *J. Electr. Mat.*, **38**:1478–1482, 2009. 7
- [40] E. SKRABECK AND D. S. TRIMMER. *Handbook of Thermoelectrics.* D. M. Rowe, 1995. 7
- [41] J. XU, H. LI, B. DU, X. TANG, Q. ZHANG, AND C. UHER. **High thermoelectric figure of merit and nanostructuring in bulk AgSbTe₂.** *J. of Mater. Chem.*, **20**:6138–6143, 2010. 7
- [42] S. V. BARABASH, V. OZOLINS, AND C. WOLVERTON. **First-Principles Theory of Competing Order Types, Phase Separation, and Phonon Spectra in Thermoelectric AgPb_mSbTe_{m+2} Alloys.** *Phys. Rev. Lett.*, **101**:155704, 2008. 7
- [43] R. DETEMPLE, D. WAMWANGI, M. WUTTIG, AND G. BIHLMAYER. **Identification of Te alloys with suitable phase change characteristics.** *Appl. Phys. Lett.*, **83**:2572, 2003. 7

REFERENCES

- [44] C. STEIMER, W. WELNIC, J. KALB, AND M. WUTTIG. **Towards an atomistic understanding of phase change materials.** *J. of Optoelectr. and Adv. Mat.*, **8**:2044–2050, 2006. 7
- [45] E. QUAREZ, K. F. HSU, R. PCIONEK, N. FRANGIS, E. K. POLYCHRONIADIS, AND M. G. KANATZIDIS. **Nanostructuring, compositional fluctuations, and atomic ordering in the thermoelectric materials AgPbmSbTe_{2+m} : the myth of solid solutions.** *J. of the Am. Chem. Soc.*, **127**(25):9177–9190, 2005. 7
- [46] K. HOANG, S. D. MAHANTI, J. R. SALVADOR, AND M. G. KANATZIDIS. **Atomic ordering and gap formation in Ag-Sb-based ternary chalcogenides.** *Phys. Rev. Lett.*, **99**:156403, 2007. 7
- [47] R. G. MAIER. **Zur kenntnis des systems PbTeAgSbTe_2 .** *Z. Metallkd.*, **54**:311–312, 1963. xiii, 7, 8, 10
- [48] J. D. SUGAR AND D. L. MEDLIN. **Precipitation of Ag_2Te in the thermoelectric material AgSbTe_2 .** *J. of All. and Comp.*, **478**(1-2):75–82, 2009. xiii, 7, 8
- [49] T. J. ZHU, F. YAN, S. N. ZHANG, AND X. B. ZHAO. **Microstructure and electrical properties of quenched $\text{AgPb}_{18}\text{Sb}_{(1-x)}\text{Te}_{20}$ thermoelectric materials.** *J. of Phys. D: Appl. Phys.*, **40**(11):3537–3540, 2007. 9
- [50] H. S. DOW, M. W. OH, S. D. PARK, B. S. KIM, B. K. MIN, H. W. LEE, AND D. M. WEE. **Thermoelectric properties of $\text{AgPbmSbTe}_{(m+2)}$ at elevated temperature.** *J. Appl. Phys.*, **105**(11):113703, 2009. 9
- [51] *Manual to the Physical Properties Measurement System (PPMS) from Quantum Design.* xiv, 10, 12
- [52] D.-P. YANG Y.-L. CHEN. *Mössbauer Effect in Lattice Dynamics.* Wiley-VCH Verlag GmbH & Co. KGaA, 2007. 11
- [53] R. RÜFFER AND A. I. CHUMAKOV. **Nuclear inelastic scattering.** *Hyp. Inter.*, **128**:255–272, 2000. xiv, 17, 19
- [54] H.-C. WILLE, R. P. HERMANN, I. SERGUEEV, U. PELZER, A. MÖCHEL, T. CLAUDIO, J. PERSSON, R. RÜFFER, A. SAID, AND YU. V. SHVYD'KO. **Nuclear forward and inelastic spectroscopy on ^{125}Te and $\text{Sb}_{2125}\text{Te}_3$.** *Europhys. Lett.*, **91**:62001–62006, 2010. 18
- [55] I. SERGUEEV, H.-C. WILLE, R. P. HERMANN, D. BESSAS, YU. V. SHVYD'KO, M. ZAJAC, AND R. RÜFFER. **Milli-electronvolt monochromatization of hard X-rays with a sapphire backscattering monochromator.** *J. of Synchr. Rad.*, **18**:802–810, 2011. 18
- [56] H.-C. WILLE, YU. V. SHVYD'KO, E. E. ALP, H. D. RÜTER, O. LEUPOLD, I. SERGUEEV, R. RFFER, A. BARLA, AND J. P. SANCHEZ. **Nuclear resonant forward scattering of synchrotron radiation from ^{121}Sb at 37.13 keV.** *Europhys. Lett.*, **74**:170, 2006. 18
- [57] V. G. KOHN AND A. I. CHUMAKOV. **DOS: Evaluation of phonon density of states from nuclear resonant inelastic absorption.** *Hyp. Int.*, **125**:205–221, 2000. 19

Chapter 2

Lattice dynamics and structure of GeTe, SnTe and PbTe

Lattice dynamics and structure of GeTe, SnTe and PbTe

P. Bauer Pereira^{1,2}, I. Sergueev^{1,3}, S. Gorsse⁴, J. Dadda⁵, E. Müller⁵,
Raphaël P. Hermann^{1,2}

¹*Jülich Centre for Neutron Science JCNS and Peter Grünberg Institut PGI, JARA-FIT,
Forschungszentrum Jülich GmbH, D-52425 Jülich, Germany*

²*Faculté des Sciences, Université de Liège, B-4000 Liège, Belgium*

³*European Synchrotron Radiation Facility, F-38043 Grenoble Cedex, France*

⁴*CNRS, Université de Bordeaux, ICMCB, F-33608 Pessac Cedex, France*

⁵*Deutsches Zentrum für Luft- und Raumfahrt, Institut für Werkstoff-Forschung, Thermoelektrische
Materialien und Systeme, D-51147 Köln, Germany*

Abstract

The lattice dynamics in the IV-VI compounds GeTe, SnTe and PbTe were studied by ¹²⁵Te and ¹¹⁹Sn nuclear inelastic scattering and the obtained partial density of phonon states were compared with published theoretical calculations. The phase purity and structure were characterized by high energy X-ray diffraction. The effect of the atomic arrangement, rhombohedral for GeTe and cubic for SnTe and PbTe, is visible in the density of phonon states. Vibrational properties are found to be in good agreement with available calculated data and the softer character of the NaCl-type structures in comparison with the rhombohedral GeTe is confirmed.

Key words: chalcogenides, phonons, structure, sound velocity, nuclear inelastic scattering

2.1 Introduction

Among the IV-VI class of materials, PbTe, SnTe, and GeTe have been extensively studied and attracted interest over the last decades due to their practical applications in infrared optoelectronics and in thermoelectric devices (1, 2). Applications are not limited to the pure compounds and alloys such as $\text{AgPb}_{18}\text{SbTe}_{20}$ (3), $\text{Pb}_{0.36}\text{Ge}_{0.64}\text{Te}$ (4) and $\text{Pb}_{0.25}\text{Sn}_{0.25}\text{Ge}_{0.5}\text{Te}$ (5) also find use. Large dielectric constants, high carrier mobilities, direct narrow band gaps and various structural phase transitions are other attractive aspects (6). Superconductivity has been identified in GeTe (7) and SnTe (8) below 0.4 K, whereas this characteristic has not yet been confirmed for PbTe.

PbTe and SnTe are closely related. Lead telluride is a semiconductor which crystallizes in the NaCl-structure ($Fm\bar{3}m$ group) with lattice constant $a = 6.460(1) \text{ \AA}$ (9). The PbTe structure is formed by two inter-penetrating fcc lattices, one of Pb atoms and other of Te atoms connected by bonds with mixed ionic and covalent character (10). Each atom is octahedrally coordinated by six nearest neighbors of the other type, as seen in Fig. 2.1(a).

By appropriate doping, either n- or p-type semiconduction can be obtained. At 298 K, β -SnTe presents the same crystal structure as PbTe, with $a = 6.312 \text{ \AA}$ (11). Below 100 K the cubic symmetry is reduced to a rock salt-like equilibrium structure, α -SnTe, that is slightly rhombohedrally distorted along the (111) direction (12, 13, 14). Like PbTe and SnTe, GeTe also crystallizes in the rocksalt structure at temperatures above $T_c \approx 700 \text{ K}$ (15), in the β -GeTe phase, with cell parameters $a = 6.020 \text{ \AA}$ (15). Below T_c , α -GeTe phase is stabilized into a rhombohedral structure ($R\bar{3}m$) with an angular distortion of $\approx 1.65^\circ$ between the principal axes and a relative displacement of the Ge and Te sublattices along [111] direction (16), resulting in lattice parameters $a = b = 4.1719 \text{ \AA}$ and $c = 10.710 \text{ \AA}$ (17, 18), see Fig. 2.1(b). Given the polar nature of the Ge-Te bond, ferroelectricity results. A similar but short range effect was recently reported in PbTe (19), above 550 K, where a tendency to ferroelectric-like dipolar fluctuations was revealed. In this case, however, no macroscopic symmetry change is associated but only atomic off-centering and formation of local structural dipoles (19).

Lead telluride, tin telluride, and germanium telluride based alloys are known as appropriate candidates for thermoelectric modules in the temperature range from room temperature to $\approx 773 \text{ K}$. PbTe is one of the oldest and most studied thermoelectric materials for power generation, since the early report by Ioffe (20). The interesting thermoelectric properties of

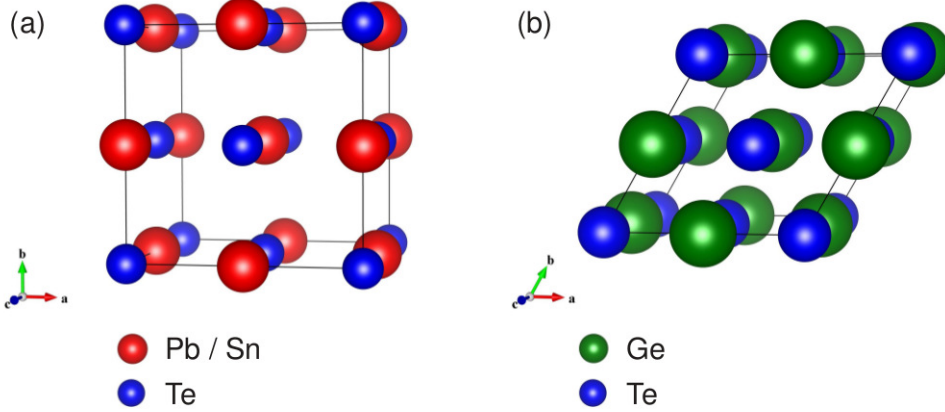


Figure 2.1: (a) The units cell for PbTe, α -SnTe and (b) β -GeTe, all at 298 K. In both plots Te is depicted in blues atoms, Pb and Sn in red, and Ge in green. Pb / Sn and Ge are illustrated as larger spheres as compared to Te.

PbTe occur mainly due to its rather low thermal conductivity, $2.2 \text{ Wm}^{-1}\text{K}^{-1}$ at room temperature, and excellent electronic properties, resulting in a maximum ZT between 0.8-1.0 at 700 K (9). Optimally doped PbTe ($A_x\text{Pb}_{1-x}\text{Te}$, $A = \text{Sn, Tl, or I}$ and $0.01 \leq x \leq 0.02$) exhibits a ZT enhancement of more than 50%, reaching 1.5 at 773 K (21, 22). Nanostructuring PbTe-based materials through solid solution decomposition has also been reported for systems such as (Pb,Ge)Te alloys (23), TAGS (Te-Ag-Ge-Sb, GeTe alloy with 15% AgSbTe₂) (24, 25) and LAST (Pb-Sb-Ag-Te, AgPb_{*m*}SbTe_{*m*+2}) (3, 26). Further enhancement of the figure of merit, with $ZT \sim 2$ were reported for PbTe/PbTeSe thin film superlattices (27) and PbSeTe/PbTe quantum-dot superlattice (QDSL) (28).

In contrast, SnTe has not yet received the same attention mainly due its intrinsic defect chemistry: compared to PbTe, which can be either p-type or n-type, SnTe is always Sn-deficient and therefore, pure SnTe is invariably a p-type semiconductor (29). The large cation vacancies and hole concentration lead to high carrier concentration ($\approx 5 \cdot 10^{19} - 5 \cdot 10^{20} \text{ cm}^{-3}$) (30) which limits the Seebeck coefficient, and thus, the power factor. (31). For SnTe, with medium doping level, a maximum ZT of ≈ 1 was reported, at 545 K(32). For thermoelectric applications, however, in quantum well systems which utilize the special band offsets introduced by alloys, such as in SnTe/PbTe system (33, 34), the charge concentration can be controlled and optimized and thermal conductivity $\approx 2 \text{ Wm}^{-1}\text{K}^{-1}$ (35, 36), at 298 K, are obtained. GeTe presents a thermal conductivity, at 298 K, of $2.6 \text{ Wm}^{-1}\text{K}^{-1}$ (37) and com-

pared to PbTe and SnTe, has a larger thermoelectric figure of merit (38). Yet this alloy is associated with low structural and chemical stability, due to its high sublimation rate and low-temperature phase transition (39). Doping and alloy engineering approaches can be used to control and optimize the structural stability and thermoelectric properties of GeTe, *e.g.*, in Bi₂Te₃/GeTe system, where Bi₂Te₃ acts as a donor for GeTe (38). By adding PbTe (4) and/or SnTe (5) to GeTe, alloys with better stability than pure GeTe are obtained, since the phase transition temperature is reduced below the working temperature. At the same time, by use of solid solution, a decrease in thermal conductivity can be obtained since the large difference in atomic masses of the constituent atoms (Sn and Pb) can reduce the thermal conductivity in the disordered alloy (40).

In order to have a better understanding of the underlying lattice dynamics responsible for the low thermal conductivity and other lattice related properties in pure PbTe, SnTe and GeTe, it is necessary to learn more about the structure and density of phonon states on such materials. Whereas *ab initio* calculations of the partial phonon density of state (DPS) within density functional theory, with and without spin-orbit interaction, have been reported for PbTe (41, 42) and GeTe (43), the understanding of the phonon density of states of tin telluride is less complete. Experimentally, phonon dispersion relations of PbTe (44, 45) and SnTe (46) were obtained by inelastic neutron scattering measurements. However, the density of phonon states of GeTe has not yet been confirmed experimentally. Here we report lattice vibrational properties of PbTe, α -SnTe and β -GeTe by ¹²⁵Te and ¹¹⁹Sn by Nuclear Inelastic Scattering (NIS) (47). Through this method, additional information such as the mean force constant, Debye temperature, the Lamb-Mössbauer factor, atomic displacement parameters, and the average sound velocity were obtained. Our results agree fairly well with the theoretical calculations and previous experimental reports. A comparison between the sound velocity and the Debye temperature of the three compounds supports the similarities in properties between PbTe and SnTe. GeTe is established as a material with a stiffer structure as compared to PbTe and SnTe.

2.2 Experimental

About 100 mg of polycrystalline samples were synthesized using high purity (99,999%) Pb, 80% enriched Sn-119, Ge, and 95% enriched Te-125, according to stoichiometry. Each composition was placed into a quartz capillary, evacuated, sealed under vacuum and heated above its melting temperatures, 1000, 1063 and 1200 K for GeTe, SnTe and PbTe, respectively. After a homogenization period of six hours at these high temperatures, the materials were rapidly cooled by water quenching. In order to evaluate the homogeneity and structure of the obtained pellets, X-ray diffraction at room temperature was performed at the high energy station 6-ID-D, of the Advanced Photon Source. The X-ray energy used was 99.53 keV ($\lambda = 0.124559 \text{ \AA}$) and a circular image plate detector camera Mar345 was used. The sample to detector distance of 1850(1) mm was calibrated using NIST640c silicon. The diffraction patterns were refined by the Rietveld method using FullProf (48).

Nuclear inelastic scattering measurements on PbTe, SnTe and GeTe samples were performed for ^{125}Te and ^{119}Sn , at the resonance energy of $E_{\gamma}^{Te} = 35.49 \text{ keV}$ (49, 50) and $E_{\gamma}^{Sn} = 23.88 \text{ keV}$ (50), respectively, at the ID22N beamline of the European Synchrotron Radiation Facility. 1.1 meV resolution (50) was achieved for both energies.

2.3 Results and discussion

2.3.1 Structural characterization

The X-ray diffraction patterns for PbTe, SnTe and GeTe are presented in Fig. 2.2. From our Rietveld refinement, PbTe is characterized as one-phase material, which crystallizes in the $Fm\bar{3}m$ crystal structure with cell parameter $a = 6.461(3) \text{ \AA}$. SnTe has the same crystal structure as PbTe but a smaller lattice parameter $a = 6.318(3) \text{ \AA}$. Additionally, the presence of a secondary phase was identified for SnTe, where SnO_2 accounts for 5(1)%wt of the sample. This phase has the $P4_2/mnm$ structure with lattice parameters $a = b = 4.732(2) \text{ \AA}$ and $c = 3.185(3) \text{ \AA}$. In GeTe, secondary phases were not observed. The pure GeTe phase was indexed with a rhombohedral $R\bar{3}m$ crystal structure, with lattice parameters $a = b = 4.153 \text{ \AA}$ and $c = 10.663 \text{ \AA}$. Table 2.1 summarizes the refined parameters at 298 K and reliability factors obtained by Rietveld analysis for the PbTe, SnTe and GeTe.

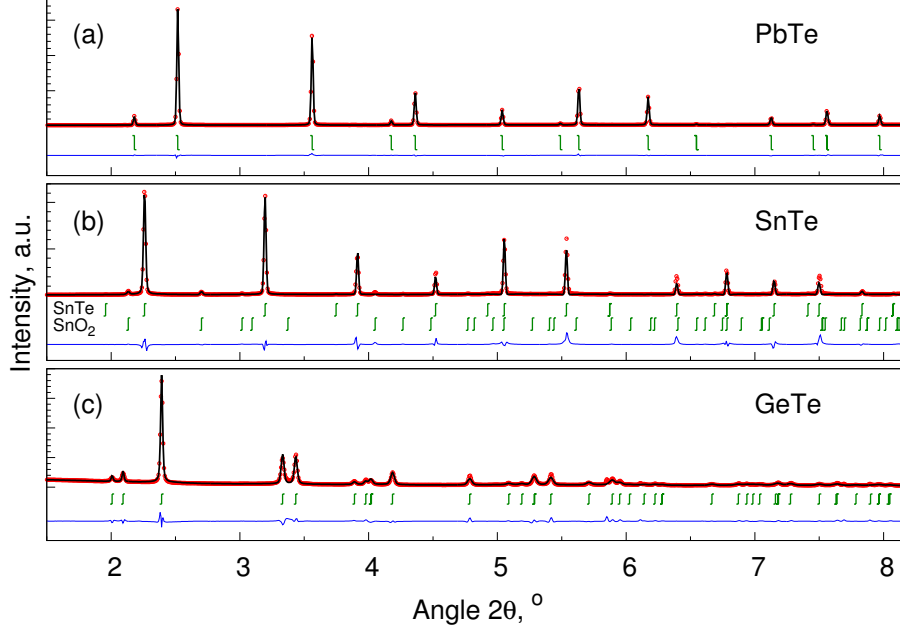


Figure 2.2: Room temperature X-ray diffraction patterns of PbTe, SnTe and GeTe. Red dots correspond to the experimental data, while the black line, blue line and green sticks are, respectively, the Rietveld refinement, the difference plot and the peak positions for main and secondary phases.

Table 2.1: PbTe, SnTe and GeTe at 298 K: Measurement conditions, refined results and reliability factors obtained by Rietveld analysis.

	PbTe	SnTe	SnO ₂	GeTe
Crystal system	Cubic	Cubic	Tetragonal	Rhombohedral
Space group	$Fm\bar{3}m$	$Fm\bar{3}m$	$P4_2/mnm$	$R\bar{3}m$
Lattice parameter, Å	a = 6.461(3)	a = 6.318(3)	a = b = 4.732(2) c = 3.185(3)	a = b = 4.156(3) c = 10.663(5)
Volume, Å ³	269.711	252.196	71.318	161.430
Density, g/cm ³	8.17	6.48	7.0	6.18
Phase amount, wt%	100(1)	95(5)	5(1)	100(1)
R _p (R-structure factor), %	22.9	21.9	21.9	22.4
R _{wp} (R-weighted pattern), %	24.3	4.0	14.0	21.8
R _{exp} (Expected error), %	25.85	12.89	12.89	26.8
GoF (Goodness of fit)	0.94	1.08	1.08	0.66

2.3 Results and discussion

Table 2.2: Atomic parameters and atomic displacement parameters $\langle u^2 \rangle$ of PbTe, SnTe, GeTe and the secondary phase identified in this study, at 298 K.

Compound	Atom	Site	Occupancy	x	y	z	$\langle u^2 \rangle (\text{\AA}^2)$
PbTe	Pb	$4a$	0.01959	0.0	0.0	0.0	0.0244(3)
	Te	$4b$	0.02083	0.5	0.5	0.5	0.0129(3)
SnTe	Sn	$4a$	0.02063	0.0	0.0	0.0	0.0199(3)
	Te	$4b$	0.02083	0.5	0.5	0.5	0.0101(3)
SnO₂	Sn	$2a$	0.125	0.0	0.0	0.0	-
	O	$4f$	0.125	0.3071	0.3071	0.3071	-
GeTe	Ge	$3a$	0.16667	0.0	0.0	0.2403	0.0165(4)
	Te	$3a$	0.16667	0.0	0.0	0.7597	0.0091(3)

From Rietveld refinement, the amplitude of the thermal vibration in the studied alloys was also obtained. The Pb, Sn and Ge displacement parameters are consistently larger than the ones of the lighter chalcogen atom. As seen in Table 2.2, the atomic displacement parameter $\langle u^2 \rangle$ of the cation increases for larger atomic weight. Thermal parameters of the Pb atoms were found to be larger than those of the chalcogen reported elsewhere (51). As the studied materials and their alloys are intended for thermoelectric applications which requires low thermal conductivity values, the large atomic displacement parameters is of interest and indicate significant phonon scattering in these compounds. It was suggested by Noda *et al.* that thermal vibrations in such compounds can be further enhanced by alloying, such as the addition of Ge or Sn in PbTe and/or Pb in SnTe and GeTe (40). This creates compositional fluctuations across the material that can also contribute to decrease the thermal conductivity by adding disorder scattering to phonon-phonon scattering in the system. Additional information on the site position and occupancy from the Rietveld refinement are summarized on Table 2.2, where the Pb, Sn and Ge occupancies were refined assuming full occupation of the Te sites. PbTe and SnTe show a deficiency of Pb and Sn, whereas for GeTe, no deviation from the nominal stoichiometry is observed.

2.3.2 Lattice dynamics characterization

Nuclear inelastic scattering from the ^{125}Te NIS experiments in PbTe, SnTe and GeTe are shown in Fig. 2.3. The nuclear forward scattering (NFS, *i.e.*, elastic scattering) represents the instrumental function with a FWHM resolution of 1.1 meV for all measurements. The data treatment procedure to extract the DPS from the inelastic scattering data includes the subtraction of the elastic peak and the correction of the multiphonon contribution to the inelastic scattering (52). Finally, the data was deconvoluted by the experimental instrumental function and reconvoluted with a symmetric Gaussian with a FWHM of 1.9 meV, in order to avoid unphysical termination ripples in the DPS.

The partial Te density of phonon states of PbTe, SnTe and GeTe at 55, 60 and 30 K, respectively, and the Sn DPS and total DPS of SnTe, at 60 K, along with *ab-initio* calculated Te-contribution for the DPS of PbTe (41, 42) and GeTe (43), and the total DPS of SnTe measured by neutron scattering (46) are discussed next. Measurements were performed at low temperature in order to minimize multiphonon contributions to the inelastic spectra and the temperature was verified by the detailed balance in the inelastic spectra. The DPS extracted from the inelastic scattering spectra are shown in Fig. 2.4.

The similarities between the Te specific DPS of PbTe and SnTe are quite evident whereas GeTe presents unique features. Both Te-DPS spectra consist of a main peak around 11 and 12 meV, for PbTe and SnTe, respectively. The Sn-DPS consists of two main regions centered at ~ 7 and 15 meV. In contrast, the partial Te-DPS of GeTe exhibits two peaks centered at 9.5 and 16 meV plus a minor peak at ~ 20.8 meV. The upper limit of the acoustical range, E^A , can be estimated, in first approximation (53), by

$$M_R/M_{Total} = \int_0^{E^A} g(E)d(E), \quad (2.1)$$

where M_R is the mass of the resonant nucleus and M_{Total} is the total mass of the content of the primitive unit cell. As calculated from the Te DPS in PbTe, SnTe, the acoustical regions extend up to ~ 10 meV, and in GeTe, up to ~ 12 meV; the E^A calculated from the Sn DPS in SnTe is also ~ 10 meV. The cut-off energies for PbTe, SnTe and GeTe Te-DPS are ~ 20 meV and ~ 25 meV, respectively. This different cut-off arises due to the difference in the mass and lattice parameters of PbTe and SnTe as compared to GeTe, and to the different space group in which GeTe crystallizes. The softer characteristics of PbTe and SnTe can also be

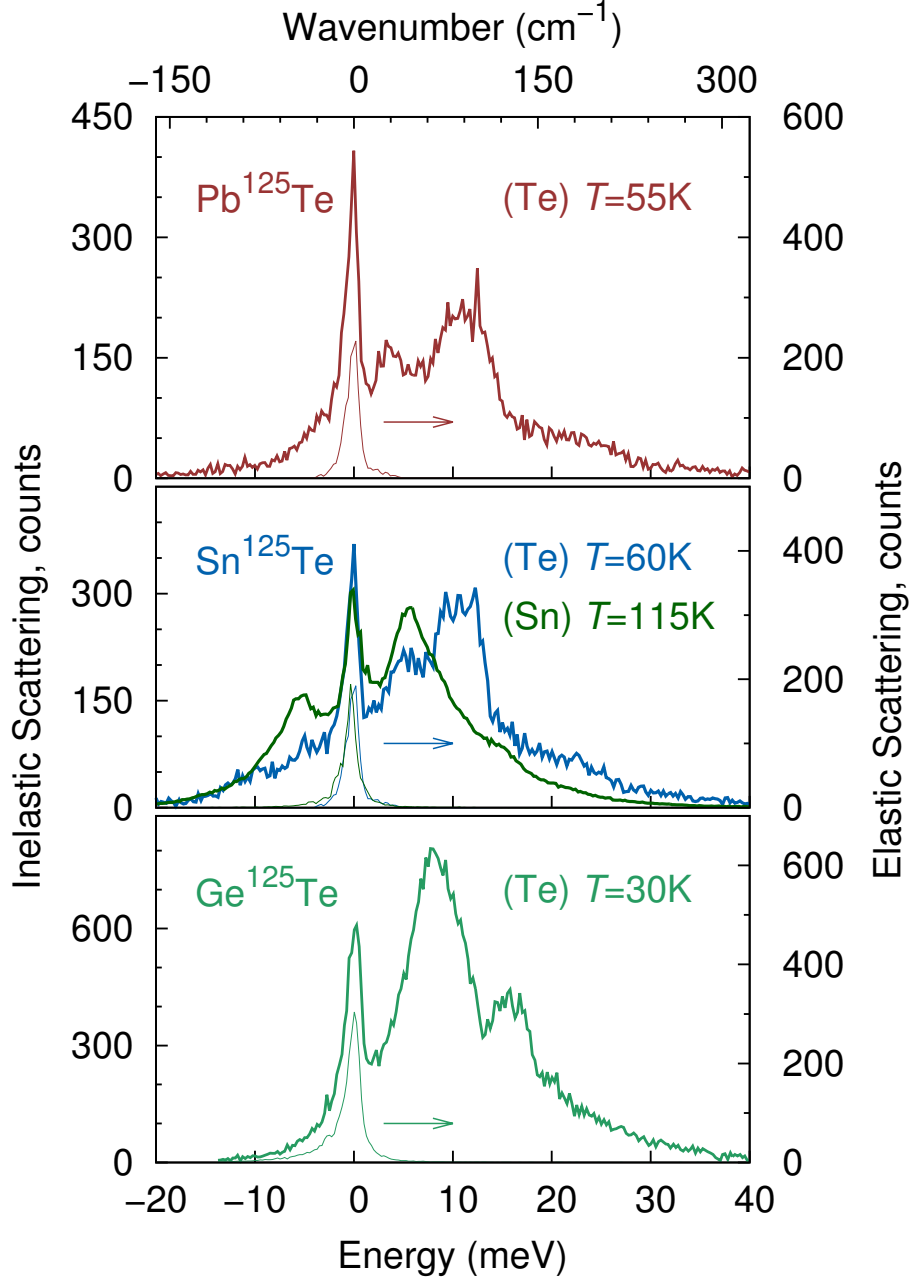


Figure 2.3: The nuclear inelastic scattering, NIS, spectra and the instrumental functions, measured by nuclear forward scattering, NFS, obtained with the ¹²⁵Te resonance in PbTe (top), SnTe (middle), and GeTe (bottom), and with the ¹¹⁹Sn resonance in SnTe (middle).

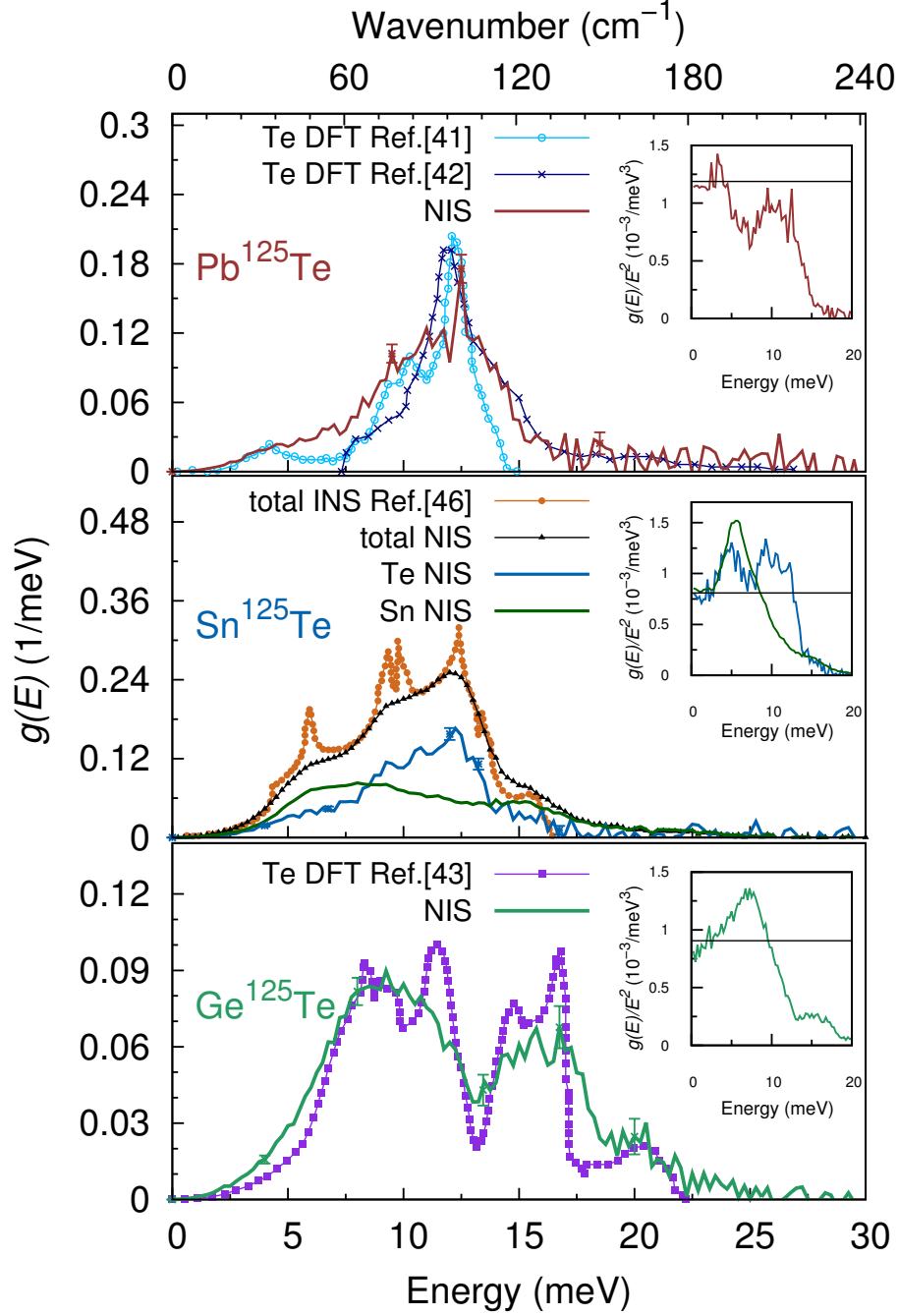


Figure 2.4: The partial Te density of phonon states of PbTe (top), SnTe (middle) and GeTe (bottom) at 55, 60 and 30K, respectively (solid lines). Typical error bars are given. The total DPS of SnTe by NIS is also presented (middle, in black). The lines with points are the theoretical calculations for PbTe (light blue (41) and dark blue (42)) and GeTe (violet (43)) and the total DPS of SnTe from inelastic neutron scattering data (orange (46)). The insets show the reduced partial DPS, $g(E)/E^2$, and the low energy fit, between 0 and 4 meV, for the Debye levels, indicated by the same type of lines.

confirmed by their estimated sound velocities. The sound velocity was estimated from the Debye level $\lim_{E \rightarrow 0} g(E)/E^2$ (54), in the Debye approximation (55), using

$$\lim_{E \rightarrow 0} g(E)/E^2 = \frac{M_R}{2\pi^2 \hbar^3 \rho v_s^3}, \quad (2.2)$$

where ρ is the density of the material. The average sound velocities, v_s , of PbTe, SnTe and GeTe are 1700(100), 1800(80) and 1900(70) m/s, respectively (see also Table 2.3). The values obtained are in agreement with literature values reported for PbTe, $v_s = 1830(30)$ m/s (56), and SnTe, $v_s = 1750(50)$ m/s, obtained from the elastic constants in Ref. (57).

The experimental DPS are compared in Fig. 2.4 with the partial DPS from first-principles calculations for PbTe and GeTe (41, 42, 43), and the total DPS of SnTe measured by neutron scattering (46). The overall agreement of the calculated values with the experimentally obtained results is fairly good, whereas the theoretical calculated DPS and single crystalline neutrons inelastic scattering data show slightly sharper peaks than the observed ones, because of the better resolution and the recalculation of the DPS from dispersion curves. Note that a small impurity contribution from SnO₂ might affect the Sn DPS in SnTe. The insets of Fig. 2.4 show the reduced DPS, $g(E)/E^2$, and the low energy fit, between 0 and 4 meV for the Debye levels.

Additional lattice related properties (interatomic force constants, Lamb-Mössbauer factor and atomic displacement) were obtained from the DPS (55) and are presented in Table 2.3. The atomic displacement parameters, $\langle u^2 \rangle$, obtained from NIS at low temperatures were extrapolated to room temperature values, within the harmonic approximation using

$$f_{LM}(T) = \exp(-E_R) \int_0^\infty \frac{g(E)}{E} \frac{1 + \exp(-E/k_B T)}{1 - \exp(-E/k_B T)} dE \quad (2.3)$$

and the direct relation between the atomic displacement and the Lamb-Mössbauer factor $\langle u^2 \rangle = -\ln f_{LM}/k^2$ (55), where k is the photon wavevector and $E_R = \hbar^2 k^2 / 2M_R c^2$, is the recoil energy of the resonant nucleus. Note that the extrapolated atomic displacement parameters obtained from low temperature NIS are in good agreement with those obtained by X-ray diffraction. The atomic displacement of Pb, Sn and Ge are larger than for Te. For PbTe, this behavior can be related to the lighter atomic mass of Te as compared to the one of Pb. However, for SnTe and GeTe the reason for such behavior is unclear, but it might be related to the tendency for off centering and local distortions in these compounds (19).

Table 2.3: Summary of sound velocity, force constant, Lamb-Mössbauer factor, atomic displacement parameter and Debye temperature in polycrystalline PbTe, SnTe and GeTe calculated from the Te-partial DPS.

isotope	T (K)	v_s (m/s)	F^M (N/m)	f_{LM} -	$\langle u^2 \rangle$ (\AA^2) at T	$\langle u^2 \rangle$ (\AA^2) at 298 K	θ_D	
PbTe	Te	55	1700 (100)	82(2)	0.42(2)	0.0027(4)	0.0118(4)	170(5)
SnTe	Te	60	1800 (80)	64(4)	0.39(3)	0.0029(4)	0.0120(5)	170(5)
SnTe	Sn	115	1800 (80)	67(4)	0.41(3)	0.0063(5)	0.0157(5)	160(5)
GeTe	Te	30	1900 (70)	77(4)	0.54(3)	0.0019(4)	0.0107(4)	180(7)

The average Debye temperatures of $\theta_D = 170(5)$ K for PbTe, $\theta_D \sim 165(5)$ K for SnTe, and a slightly higher value of $180(7)$ K for GeTe were calculated from the partial DPS with

$$\theta_D^2 = 3/(k_B^2 \int_0^\infty g(E)/E^2 dE). \quad (2.4)$$

The value obtained for PbTe and SnTe are higher than reported from calorimetry by Shelimova *et al.* (58), of 125 K (at 200 K) and 140 K, respectively. The large difference in the case of PbTe is ascribed to the partial Pb DPS not probed here. The reported Debye temperature for rhombohedral α -GeTe, $\theta_D = 199$ K (58), is in good agreement with our value of $\theta_D = 180(7)$ K. Additionally, the calculated average mean force constant around ≈ 70 -80 N/m indicates very soft interatomic bonds, which is comparable to typical Te force constants in thermoelectric materials, such as Bi_2Te_3 and Sb_2Te_3 with force constants of 55(2) and 58(2) N/m (59), respectively, but much smaller than *e.g.* Sb mean force constant in CoSb_3 (117 N/m) (60). Interestingly, the lattice properties of SnTe are very similar to the ones presented by PbTe, which can be an opportunity in the study and development of Pb-free compounds for thermoelectric applications.

2.4 Conclusion

A combined study of the structure and lattice dynamics of PbTe, SnTe and GeTe were performed by high-energy X-ray diffraction and nuclear inelastic scattering, respectively. The cubic NaCl-structure was confirmed for PbTe and SnTe, whereas GeTe is refined as a rhombohedral phase, at room temperature. From NIS measurements, the effect of the

crystal structure on the density of phonon states is also seen through the differences between GeTe, and PbTe and SnTe DPS. The phonon modes of these systems are in a narrow energy range below ≈ 25 meV, which indicates low force constants and a soft dynamic behavior. The Debye temperatures, the velocities of sound and the mean force constants are small as compared to other thermoelectric systems such as the Sb mean force constant in CoSb₃ (117 N/m) (60), but comparable to typical Te force constants in Bi₂Te₃ and Sb₂Te₃ (59).

The PbTe and SnTe structure (NaCl-structure and rhombohedrally distorted NaCl-structure, respectively) is softer than GeTe (rhombohedral). The experimental NIS results are found to be in fair agreement with *ab initio* calculations, in the case of PbTe (41, 42) and GeTe (43), and with experimental data from inelastic neutron scattering for SnTe (46). The estimated average mean force constant between 60 and 80 N/m arise from the low energy of the phonon modes and indicates, for the studied compounds, soft interatomic bonds. The sound velocities of PbTe, SnTe and GeTe, respectively, 1700(100), 1800(80) and 1900(70) m/s were obtained from the density of phonon states and reveal a stiffer character of rhombohedral structure of GeTe, in comparison with the cubic NaCl structure of PbTe and SnTe. In addition, the low Debye temperature, $\theta_D = 170(5)$ K of PbTe and SnTe, and 180(7) K for GeTe in combination with their low sound velocity are key factors to the high thermoelectric performed exhibit by the studied tellurides. Based on our first measurements on the pure binaries, further investigations on alloys, *e.g.*, Ge or Sn in PbTe and/or Pb in SnTe and GeTe, are now possible. In the future, for pure binaries, by varying the sample environment and performing NIS at high pressure, the Grüneisen parameter can be directly obtained and the crystal anharmonicity, which strongly affects the behavior of the crystal lattice and the thermal conductivity in the material, can be quantified.

2.5 Acknowledgements

We thank Mr. D. Bessas for his support during the NIS measurements, Dr. K. Frieze for her advice in crystallography and Dr. B. Klobes for his helpful comments on the manuscript. The European Synchrotron Radiation Facility and the Advanced Photon Source are acknowledged for provision of synchrotron radiation beam time at the nuclear resonance station ID18 and ID22N and high-energy station 6-IDD, respectively. The Federal Ministry for Education and Research of Germany (BMBF) is acknowledged for funding this research in the project NanoKoCh - Nanostructured Complex Chalcogenides (03X3540) and the Helmholtz

2.5 Acknowledgements

Gemeinschaft Deutscher Forschungszentren for funding the Young Investigator Group “Lattice dynamics in emerging functional materials” VH NG-407.

References

- [1] L. D. HICKS, T. C. HARMAN, X. SUN, AND M. S. DRESSELHAUS. **Experimental study of the effect of quantum-well structures on the thermoelectric figure of merit.** *Phys. Rev. B*, **53**:R10493–R10496, 1996. 25
- [2] C. M. I. OKOYE. **Electronic and optical properties of SnTe and GeTe.** *J. of Phys.: Cond. Matt.*, **14**:8625, 2002. 25
- [3] K. F. HSU, S. LOO, F. GUO, W. CHEN, J. S. DYCK, C. UHER, T. HOGAN, E. K. POLYCHRONIADIS, AND M. G. KANATZIDIS. **Cubic AgPbmSbTe_{2+m}: bulk thermoelectric materials with high figure of merit.** *Science*, **303**(5659):818–821, 2004. 25, 26
- [4] S. GORSSE, P. BAUER PEREIRA, R. DECOURT, AND E. SELLIER. **Microstructure engineering design for thermoelectric materials: an approach to minimize thermal diffusivity.** *Chem. Mater.*, **20**(3):988–993, 2010. 25, 27
- [5] Y. ROSENBERG, Y. GELBSTEIN, AND M. P. DARIEL. **Phase separation and thermoelectric properties of the Pb_{0.25}Sn_{0.25}Ge_{0.5}Te compound.** *J. of Alloys and Comp.*, **526**:31–38, 2012. 25, 27
- [6] V. I. KAIDANOV AND Y. I. RAVICH. *Usp. Fiz. Nauk. [Engl. Transl.: Sov. Phys. Usp. 28, 31 (1985)]*, **145**:51, 1985. 25
- [7] R. A. HEIN, J. W. GIBSON, R. MAZELSKY, R. C. MILLER, AND J. K. HULM. **Superconductivity in germanium telluride.** *Phys. Rev. Lett.*, **12**:320–322, 1964. 25
- [8] J. K. HULM, C. K. JONES, D. W. DEIS, H. A. FAIRBANK, AND P. A. LAWLESS. **Superconducting interactions in tin telluride.** *Phys. Rev.*, **169**:388–394, 1968. 25
- [9] Z. DUGHAIISH. **Lead telluride as a thermoelectric material for thermoelectric power generation.** *Phys. B: Cond. Matt.*, **322**:205–223, 2002. 25, 26
- [10] G. LUCOVSKY AND R. M. WHITE. **Effects of resonance bonding on the properties of crystalline and amorphous semiconductors.** *Phys. Rev. B*, **8**:660–667, 1973. 25
- [11] I. LEFEBVRE, M. A. SZYMANSKI, J. O. FOURCADE, AND J. C. JUMAS. **Electronic structure of tin monochalcogenides from SnO to SnTe.** *Phys. Rev. B*, **58**:1896–1906, 1998. 25
- [12] J. E. LEWIS AND J. C. LASJAUNIAS. **Specific heat and resistivity of the GeTe-SnTe alloy system.** *Philos. Mag.*, **32**(4):687–696, 1975. 25
- [13] O. VALASSIADES AND N. A. ECONOMOU. **On the phase transformation of SnTe.** *Phys. Status Solidi A*, **30**:187–195, 1975. 25
- [14] E. K. H. SALJE, D. J. SAFARIK, K. A. MODIC, J. E. GUBERNATIS, J. C. COOLEY, R. D. TAYLOR, B. MIHAILA, A. SAXENA, T. LOOKMAN, J. L. SMITH, R. A. FISHER, M. PASTERNAK, C. P. OPEL, T. SIEGRIST, P. B. LITTLEWOOD, AND J. C. LASHLEY. **Tin telluride - a weakly co-elastic metal.** *Phys. Rev. B*, **82**:184112, 2010. 25
- [15] H. WIEDEMEIER AND P. A. SIEMERS. **The thermal expansion of GeS and GeTe.** *Z. Anorg. Allg. Chem.*, **431**:299–304, 2004. 25
- [16] T. CHATTOPADHYAY, J. X. BOUCHERLE, AND H. G. VON SCHNERING. **Neutron diffraction study on the structural phase transition in GeTe.** *J. Phys. C*, **20**:1431–1440, 1987. 25
- [17] J. GOLDAK, C. S. BARRETT, D. INNES, AND W. YOUDELIS. **Structure of alpha GeTe.** *J. Chem. Phys.*, **44**:3323, 1966. 25
- [18] T. NONAKA, G. OHBAYASHI, Y. TORIUMI, Y. MORI, AND H. HASHIMOTO. **Crystal structure of GeTe and Ge₂Sb₂Te₅ meta-stable phase.** *Thin Solid Films*, **370**:258–261, 2000. 25
- [19] E. S. BOZIN, C. D. MALLIAKAS, P. SOUVATZIS, T. PROFFEN, N. A. SPALDIN, M. G. KANATZIDIS, AND S. J. L. BILLINGE. **Entropically stabilized local dipole formation in lead chalcogenides.** *Science*, **330**:1660–1663, 2010. 25, 34

REFERENCES

- [20] A. F. IOFFE. *Semiconductor Thermoelements and Thermoelectric Cooling*. Infosearch Ltd, 1957. 25
- [21] J. P. HEREMANS, V. JOVOVIC, E. S. TOBERER, A. SARAMAT, K. KUROSAKI, A. CHAROENPHAKDEE, S. YAMANAKA, AND G. J. SNYDER. **Enhancement of thermoelectric efficiency in PbTe by distortion of the electronic density of states**. *Science*, **321**:554–557, 2008. 26
- [22] A. D. LALONDE, Y. PEI, AND G. J. SNYDER. **Reevaluation of PbTe(1-x)I(x) as high performance n-type thermoelectric material**. *Energy Environ. Sci.*, **4**:2090–2096, 2011. 26
- [23] S. GORSSE, P. BELLANGER, Y. BRECHET, E. SELLIER, A. UMARJI, U. AHL, AND R. DECOURT. **Nanostructuring via solid state transformation as a strategy for improving the thermoelectric efficiency of PbTe alloys**. *Acta Mater.*, **59**:7425–7437, 2011. 26
- [24] G. C. CHRISTAKUDIS, S. K. PLACHKOVA, AND SHELIMOVA L. E. **Thermoelectric Power of (GeTe)_{1-x}((Ag₂Te)_{1-y}(Sb₂Te₃)_y)_x Solid Solutions**. *Phys. Status Solidi*, **102**:357–366, 1987. 26
- [25] D. M. ROWE, editor. *CRC Handbook of Thermoelectrics: Macro to Nano*. CRC Press, 1995. 26
- [26] M. ZHOU, J.-F. LI, AND T. KITA. **Nanostructured AgPbmSbTem+2 system bulk materials with enhanced thermoelectric performance**. *J. Am. Chem. Soc.*, **130**(13):4527–4532, 2008. 26
- [27] R. VENKATASUBRAMANIAN, E. SILVOLA, T. COLPITTS, AND B. O’QUINN. **Thin-film thermoelectric devices with high room-temperature figures of merit**. *Nature*, **413**:597–602, 2001. 26
- [28] T. C. HARMAN, P. J. TAYLOR, M. P. WALSH, AND B. E. LAForge. **Quantum dot superlattice thermoelectric materials and devices**. *Science*, **297**(5590):2229–2232, 2002. 26
- [29] V. P. VEDENEV, S. P. KRIVORUCHKO, AND E. P. SABO. **Tin telluride based thermoelectrical alloys**. *Electr. and Opt. Prop. of Semicond.*, **32**:211–244, 1998. 26
- [30] S. SUGAI, K. MURASE, S. KATAYAMA, S. TAKAOKA, S. NISHI, AND H. KAWAMURA. **Carrier density dependence of soft TO-phonon in SnTe by Raman scattering**. *Solid State Commun.*, **24**:407–409, 1977. 26
- [31] E. ROGACHEVA AND N. DZYUBENKO. **The improvement of thermoelectric properties of heterophase alloys based on tin telluride**. In *18th Int. Conf. on Thermoelectrics*, pages 226–229, 1999. 26
- [32] L. XU, H.-Q. WANG, AND J.-C. ZHENG. **Thermoelectric properties of PbTe, SnTe, and GeTe at high pressure: an ab initio study**. *J. of Electr. Mat.*, **40**:641–647, 2011. 26
- [33] A. ISHIDA, M. AOKI, AND H. FUJIYASU. **Semimetallic Hall properties of PbTe-SnTe superlattice**. *J. Appl. Phys.*, **58**:1901, 1985. 26
- [34] S. TAKAOKA, T. OKUMURA, AND K. MURASE. **Semimetallic electrical transport in PbTe-SnTe superlattices on KCl substrate**. *Solid State Commun.*, **58**:637–640, 1986. 26
- [35] D. H. DAMON. **Thermal conductivity of SnTe between 100 and 500K**. *J. Appl. Phys.*, **37**:3181–3191, 1966. 26
- [36] J. L. CUI, X. QIAN, AND X. B. ZHAO. **Mechanical and transport properties of pseudo-binary alloys (PbTe)-(SnTe) by pressureless sintering**. *J. of Alloys and Comp.*, **358**:228–234, 2003. 26
- [37] J. M. YANEZ-LIMON, J. GONZALEZ-HERNANDEZ, J. J. ALVARADO-GIL, I. DELGADILLO, AND H. VARGAS. **Thermal and electrical properties of the Ge:Sn:Te system by photoacoustic and Hall measurements**. *Phys. Rev. B*, **52**:16321–16324, 1995. 26
- [38] Y. GELBSTEIN, O. BEN-YEHUDA, E. PINHAS, T. EDREI, Y. SADIA, Z. DASHEVSKY, AND M. P. DARIEL. **Thermoelectric properties of (Pb,Sn,Ge)Te-based alloys**. *J. Electr. Mat.*, **38**:1478–1482, 2009. 27
- [39] E. SKRABECK AND D. S. TRIMMER. *Handbook of Thermoelectrics*. D. M. Rowe, 1995. 27
- [40] Y. NODA, S. OHBA, S. SATO, AND Y. SAITO. **Charge distribution and atomic thermal vibration in lead chalcogenide crystals**. *Acta Cryst.*, **B39**:312–317, 1983. 27, 30
- [41] A. H. ROMERO, M. CARDONA, R. K. KREMER, R. LAUCK, G. SIEGLE, J. SERRANO, AND X. C. GONZE. **Lattice properties of PbX (X=S, Se, Te): Experimental studies and ab initio calculations including spin-orbit effects**. *Phys. Rev. B*, **78**:224302, 2008. xiv, 27, 31, 33, 34, 36
- [42] Y. BENCHERIF, A. BOUKRA, A. ZAOU, AND M. FERHAT. **Lattice dynamics study of lead chalcogenides**. *Infrar. Phys. and Tech.*, **54**:39–43, 2011. xiv, 27, 31, 33, 34, 36
- [43] R. SHALTAF, X. GONZE, M. CARDONA, R. K. KREMER, AND G. SIEGLE. **Lattice dynamics and specific heat of alpha-GeTe: Theoretical and experimental study**. *Phys. Rev. B*, **79**:075204, 2009. xiv, 27, 31, 33, 34, 36

REFERENCES

- [44] W. COCHRAN, R. A. COWLEY, G. DOLLING, AND M. M. ELCOMBE. **The crystal dynamics of lead telluride.** *Proc. R. Soc. London, Ser. A*, **293**:433, 1966. 27
- [45] O. DELAIRE, J. MA, K. MARTY, A. F. MAY, M. A. MCGUIRE, M.-H. DU, D. J. SINGH, A. PODLESNYAK, G. EHLERS, M. D. LUMSDEN, AND B. C. SALES. **Giant anharmonic phonon scattering in PbTe.** *Nat. Mater.*, **10**:614–619, 2010. 27
- [46] E. R. COWLEY, J. K. DARBY, AND G. S. PAWLEY. **The lattice dynamics of tin telluride.** *J. Phys. B: Sol. St. Phys.*, **2**:1916–1925, 1969. xiv, 27, 31, 33, 34, 36
- [47] A. I. CHUMAKOV AND W. STURHAHN. **Experimental aspects of inelastic nuclear resonance scattering.** *Hyp. Int.*, **123-124**:781–808, 1999. 27
- [48] J. RODRIGUEZ-CARVAJAL. **FULLPROF: a program for Rietveld refinement and pattern matching analysis.** In *Abs. Sat. Meet Powder Diff. XV Cong. IUCr p. 127*, 1990. 28
- [49] H.-C. WILLE, R. P. HERMANN, I. SERGUEEV, U. PELZER, A. MÖCHEL, T. CLAUDIO, J. PERSSON, R. RÜFFER, A. SAID, AND YU. V. SHVYD'KO. **Nuclear forward and inelastic spectroscopy on 125Te and Sb2125Te3.** *Europhys. Lett.*, **91**:62001–62006, 2010. 28
- [50] I. SERGUEEV, H.-C. WILLE, R. P. HERMANN, D. BESSAS, YU. V. SHVYD'KO, M. ZAJAC, AND R. RÜFFER. **Milli-electronvolt monochromatization of hard X-rays with a sapphire backscattering monochromator.** *J. of Synchr. Rad.*, **18**:802–810, 2011. 28
- [51] Y. NODA, K. MASUMOTO, S. OHBA, Y. SAITO, K. TORIUMI, Y. IWATA, AND I. SHIBUYA. **Temperature dependence of atomic thermal parameters of lead chalcogenides, PbS, PbSe and PbTe.** *Acta Cryst.*, **C43**:1443–1445, 1987. 30
- [52] V. G. KOHN AND A. I. CHUMAKOV. **DOS: Evaluation of phonon density of states from nuclear resonant inelastic absorption.** *Hyp. Int.*, **125**:205–221, 2000. 31
- [53] A. I. CHUMAKOV, R. RÜFFER, O. LEUPOLD, AND I. SERGUEEV. **Insight to dynamics of molecules with nuclear inelastic scattering.** *Struct. Chem.*, **14**:109, 2003. 31
- [54] R.P. HERMANN, F. GRANDJEAN, AND G. J. LONG. **Einstein oscillators that impede thermal transport.** *Am. J. of Phys.*, **73**:110–118, 2005. 34
- [55] R. RÜFFER AND A. I. CHUMAKOV. **Nuclear inelastic scattering.** *Hyp. Inter.*, **128**:255–272, 2000. 34
- [56] J. DADDA, E. MÜLLER, S. PERLT, T. HÖCHE, P. BAUER PEREIRA, AND R. P. HERMANN. **Microstructures and nanostructures in long-term annealed AgPb18SbTe20 (LAST-18) compounds and their influence on the thermoelectric properties.** *J. Mater. Res.*, **26**:1800–1812, 2011. 34
- [57] T. SEDDON AND S. C. GUPTA. **Hole contribution to the elastic constants of SnTe.** *Solid State Comm.*, **20**:69–72, 1976. 34
- [58] L. E. SHELIKOVA AND S. K. PLACHKOVA. **Estimation of the Debye temperature of IV-VI semiconductor compounds and rhombohedral (GeTe)_{1-x}((Ag₂Te)_{1-y}(Sb₂Te₃)_y)_x solid solutions (y = 0.6).** *Phys. Status Solidi A*, **104**:679–685, 1987. 35
- [59] D. BESSAS, I. SERGUEEV, H.-C. WILLE, J. PERSSON, D. EBLING, AND R. P. HERMANN. **Lattice dynamics in Bi₂Te₃ and Sb₂Te₃: Te and Sb density of phonon states.** Under review *Phys. Rev. B*, 2012. 35, 36
- [60] A. MÖCHEL, I. SERGUEEV, N. NGUYEN, GARY J. LONG, F. GRANDJEAN, D. C. JOHNSON, AND R. P. HERMANN. **Lattice dynamics in the FeSb₃ skutterudite.** *Phys. Rev. B*, **84**:064302, 2011. 35, 36

Chapter 3

Lattice dynamics in AgSbTe_2

Lattice dynamics in AgSbTe₂

P. Bauer Pereira^{1,2}, I. Sergueev^{1,3}, J. Dadda⁴, E. Müller⁴, Raphaël P. Hermann^{1,2}

¹*Jülich Centre for Neutron Science JCNS and Peter Grünberg Institut PGI, JARA-FIT,
Forschungszentrum Jülich GmbH, D-52425 Jülich, Germany*

²*Faculté des Sciences, Université de Liège, B-4000 Liège, Belgium*

³*European Synchrotron Radiation Facility, F-38043 Grenoble Cedex, France*

⁴*Deutsches Zentrum für Luft- und Raumfahrt, Institut für Werkstoff-Forschung, D-51147 Köln,
Germany*

Abstract

The density of phonon states in AgSbTe₂ was investigated by ¹²¹Sb and ¹²⁵Te nuclear inelastic scattering. We observe that the phonon modes have energies below 25 meV and a sound velocity of $v_s = 1490(30)$ m/s is obtained. A low Debye temperature, $\theta_D = 150(15)$ K, a large Grüneisen parameter $\gamma = 2.3$ at 300 K, combined with the short phonon lifetime and the low sound velocity are key factors to the glassy nature of the low thermal conductivity in AgSbTe₂ and are associated to the high thermoelectric performance in AgSbTe₂ containing systems.

PACS numbers: 66.70.Df, 63.20D-, 65.40.Ba, 61.05.C-, 65.40.De, 63.20.Ry

3.1 Introduction

The atomic vibrations inside a solid are an important source of information about a material, as the lattice dynamics govern many thermal properties of solids. Different phenomena such as thermal expansion, phase transitions, thermal conductivity, diffusion and elastic behavior can be studied from the phonons properties of a system. Both, for thermoelectric and phase-change recording media applications, the material's thermal conductivity, κ , is important and low values are targeted. The total thermal conductivity is given by $\kappa = \kappa_E + \kappa_L$, where κ_E and κ_L are the electronic and the lattice contributions, respectively. Glass-like thermal conductivities are known both for disordered crystals and crystals exhibiting distortions of the lattice (1), and when the chemical bonds present an anharmonic character (2).

AgSbTe₂ is a narrow gap semiconductor with $E_g \approx 7.6 \pm 3$ meV (3) that crystallizes in a rock-salt cubic structure where the Ag and Sb atoms occupy the Na site, whereas Te is located at the Cl position. Due to its very low lattice thermal conductivity of 0.65 ± 0.05 W·m⁻¹K⁻¹, between 80 to 300 K (2), applications of AgSbTe₂ are mainly related to their thermoelectric (2, 4, 5) and optical phase-change properties (6, 7). For phase-change materials, the low thermal conductivity of AgSbTe₂ assures that the power and pulse duration for switching devices is minimized, whereas it permits to achieve a larger heat density in the smallest area possible (8). For thermoelectric applications, the material's efficiency is described by the dimensionless figure of merit $ZT = S^2\sigma T/\kappa$, where S is the Seebeck coefficient, σ the electrical conductivity, κ the thermal conductivity, and T , the working temperature. Low thermal conductivity will restrict diffusion of heat across the material, retaining heat at the junctions and maintaining a large temperature gradient through the device. The origin of low thermal conductivity in such compounds is related to their atomic and electronic structures which are responsible for the material's transport properties. Highly anharmonic chemical bonds (2) and compositional fluctuations across the material can also contribute to decrease the thermal conductivity by adding disorder scattering to phonon-phonon scattering. The atomic structure of AgSbTe₂ was investigated by different groups, and the possible existence of Ag-Sb ordering (5, 9, 10) was suggested. An ordering model however could not be fully established because according to the Ag₂Te-Sb₂Te₃ pseudo-binary Ag-Sb-Te phase diagram (11), AgSbTe₂ decomposes into Sb₂Te₃ and Ag₂Te below 630 K, depending on the synthesis conditions, which indicates the structural complexity of such alloys.

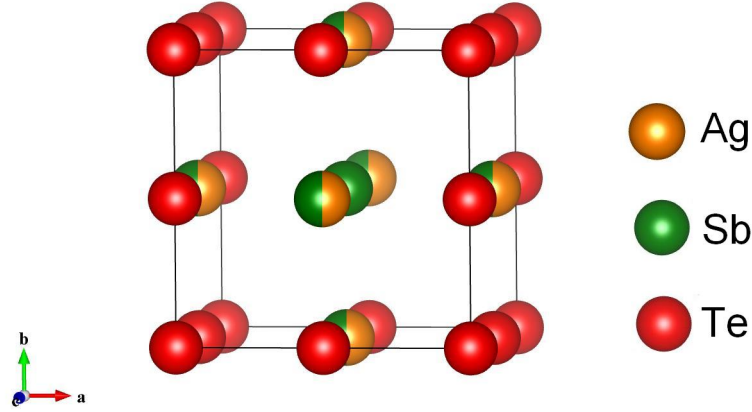


Figure 3.1: The unit cell for $Pm\bar{3}m$ AgSbTe₂, at 298 K. Ag is depicted in orange atoms, Sb in green and Te in red atoms.

To prevent this potential decomposition, AgSbTe₂ can be rapidly cooled from the melt through a quenching process. Alternatively, AgSbTe₂ is added to other thermoelectric alloys such as GeTe and PbTe and favors the formation of nanoinclusions in composite materials with increased thermoelectric efficiency, such as TAGS, (GeTe)_{0.85}(AgSbTe₂)_{0.15} (12), and LAST-*m*, AgPb_{*m*}SbTe_{2+*m*} (13). In order to clarify the *ZT* improvement due to nanocrystalline precipitates in the latter materials, a better understanding of the underlying microscopic mechanisms responsible for the low thermal conductivity in AgSbTe₂ itself is desirable.

First principles calculations of lattice vibrational properties of AgSbTe₂ predict that the phonon modes of AgSbTe₂ have average vibrational frequencies higher than the phonon spectra of PbTe due to the heavier atomic mass of PbTe (5, 14). The optical modes in AgSbTe₂ extend until 18.6 meV, whereas for PbTe, they extend up to 15.5 meV. Considering the difference between the calculated density of phonon states (DPS) from AgSbTe₂ and PbTe, Barabash *et al.* (5) suggest three main factors for the low thermal conductivity in LAST-*m* system: (i) scattering at the matrix/precipitates interfaces, (ii) mismatch of the sound velocity between matrix (PbTe-rich) and precipitates (Ag/Sb-rich), and (iii) mismatch of the ionic character of the vibrational modes, causing bending and scattering of acoustic waves. However, the phonon density of states of AgSbTe₂ has not yet been reported experimentally.

Herein we investigate the lattice vibrational properties of AgSbTe₂ by Nuclear Inelastic Scattering (NIS) (15). We report on the ¹²¹Sb and ¹²⁵Te partial density of phonon states, the mean force constant, atomic displacement parameters, the Lamb-Mössbauer factor and the average sound velocity of AgSbTe₂ at 30 K, and compare results to the calculated phonon density of states of Barabash *et al.* (5). The low value obtained for the Debye temperature, $\theta_D = 150(15)$ K combined with a Grüneisen parameter $\gamma = 2.3$ at 300 K and low sound velocity $v_s = 1490(30)$ m/s, are identified as key factors to the low thermal conductivity in AgSbTe₂ and are associated to the high thermoelectric performance in AgSbTe₂ containing systems.

3.2 Experimental

Stoichiometric amounts of high purity (99,999%) Ag, Sb and Te enriched to 95% in ¹²⁵Te were placed in a quartz capillary, evacuated and sealed under vacuum. The sample was prepared by melting the powder mixture at 1073 K. After keeping the sample for 8 h above the melting temperature, the material was water quenched. The obtained pellet, with density of 7.12 g/cm³, was characterized at room temperature by X-ray diffraction at the 6-ID-D beamline at the Advanced Photon Source. The X-ray energy used was 99.53 keV ($\lambda = 0.124559$ Å) and the detector was a circular image plate camera Mar345. The sample to detector distance of 1850(1) mm was calibrated using NIST640c silicon. Thermal expansion data was obtained by low-temperature X-ray powder diffraction, from 10 to 298 K. The wavelength of the incident radiation was 1.5405 Å (Cu- k_α). Data was collected by a Huber G670 diffractometer, between 10 and 100° and FullProf (16) was used to refine the atomic structure by Rietveld method. Heat capacity measurements from 3 to 298 K were performed using a Quantum Design Physical Property Measurement System, on a 12.5 mg sample. Nuclear inelastic scattering measurements on AgSbTe₂ were performed for ¹²¹Sb and ¹²⁵Te with the resonance energies of 37.13 (17) and 35.49 keV (18), respectively, at the ID18 and ID22N stations of the European Synchrotron Radiation Facility. For ¹²¹Sb, a resolution of 1.3 meV was reached, whereas for ¹²⁵Te, the resolution was 1.1 meV (19).

3.3 Results and discussion

3.3.1 Structural Characterization

Quarez *et al.* (9) reported Rietveld refinements using the $Pm\bar{3}m$ (cubic), $R\bar{3}m$ (rhombohedral) and a lower symmetry $P4/mmm$ (tetragonal) model for AgSbTe_2 . From our Rietveld refinement (Fig. 4.1), the $Pm\bar{3}m$ lattice is preferred, Fig. 3.1, with cell parameter of $6.070(3)$ Å. Full occupation of the cationic and anionic sites were considered and a chemically ordered random-network (stochastic) model was assumed. In this model, the force constant between atoms are randomly distributed between all atoms and no preferential atomic ordering of Ag and Sb atoms is expected. Stützite, with chemical composition $\text{Ag}_{4.5}\text{Te}_3$, was identified as secondary phase, similarly to the report by Wang *et al.* (20), accounting for 12(2)%wt Te. $\text{Ag}_{4.5}\text{Te}_3$ crystallizes in the $P\bar{6}2m$ space group with $a = b = 13.456(9)$ Å and $c = 16.915(9)$ Å, in good agreement with literature (21). This phase has a very large cell volume, $V \approx 3062.69$ Å³, containing about a hundred atoms per unit cell. The summary of refined parameters, at 298 K, and reliability factors obtained by Rietveld analysis for AgSbTe_2 are shown in Table 3.1.

The influence of temperature on the lattice constant of AgSbTe_2 is presented in Fig. 4.3. In order to decrease the data noise, the data was fitted using a third-order polynomial function $a(T)$ without first-order term. AgSbTe_2 contracts linearly on cooling until 150 K. In this region, the thermal expansion, α , defined as $\alpha = (\partial a(T)/\partial T)/a_{(300\text{K})}$, is $25 \cdot 10^{-6}\text{K}^{-1}$. This value is in good agreement with literature, where, at room temperature, $\alpha = 23 \cdot 10^{-6}\text{K}^{-1}$ is reported (22).

3.3.2 Lattice Dynamics Characterization

The measured heat capacity of AgSbTe_2 (Fig. 4.5), at 298 K is $100.4 \text{ J}\cdot\text{mol}^{-1}\text{K}^{-1}$, in agreement with reported $\approx 98.98 \text{ J}\cdot\text{mol}^{-1}\text{K}^{-1}$ (2) at the same temperature, and mostly follows the Debye model to the Petit-Dulong limit, approaching room temperature. The small deviation is observed since a harmonic approximation was used for the fitting, without considering the changes which occur in the phonon density of states with temperature and anharmonic effects. A comparison between the measured macroscopic heat capacity and ^{125}Te and ^{121}Sb heat capacities obtained from the DPS (23) is also shown. The total heat capacity from DPS was obtained by the sum of Sb and Te heat capacities contributions, assuming that the Ag contribution to heat capacity is similar to the one from Sb, and shows similar behavior to the macroscopic result. From the low temperature T^3 dependence of the heat capacity, a Debye

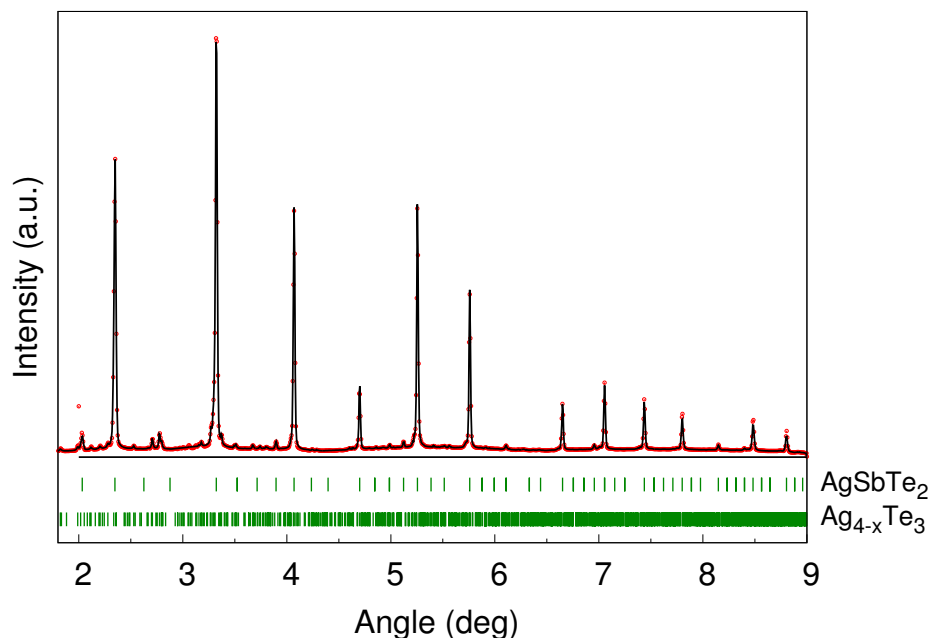


Figure 3.2: X-ray diffraction pattern of AgSbTe_2 , at room temperature. Red dots correspond to the experimental data, while the black line, blue line and green sticks are, respectively, the Rietveld refinement, the difference plot and the peak positions for AgSbTe_2 and the secondary phase $\text{Ag}_{4.5}\text{Te}_3$.

Table 3.1: AgSbTe_2 X-ray diffraction at 298 K: Refined results and reliability factors obtained by Rietveld refinement.

	AgSbTe_2	$\text{Ag}_{4.53}\text{Te}_3$
Crystal system	Cubic	Hexagonal
Space group	$Pm\bar{3}m$	$P\bar{6}2m$
Lattice parameter, \AA	$a = 6.070(3)$	$a = 13.456(9)$ $c = 16.915(9)$
Volume, \AA^3	223.648	3062.69
Density, g/cm^3	7.12	7.64
Phase amount, wt%	86(1)	14(1)
Te, wt%	88(2)	12(2)
χ^2		8.11
R_p		21.9
R_{wp}		23.9
R_{exp}		8.34

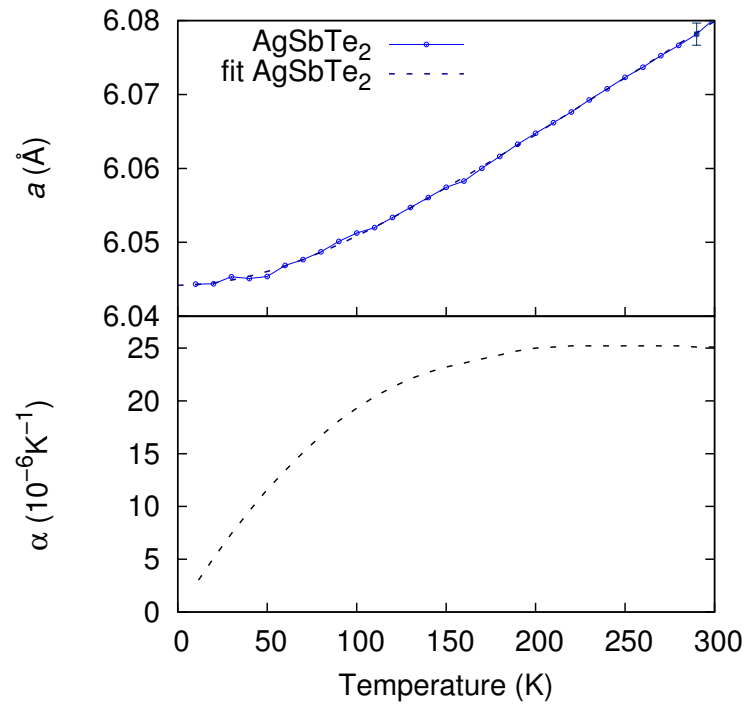


Figure 3.3: The influence of temperature on the lattice constants of AgSbTe₂ (top), and the corresponding thermal expansion, α (bottom).

temperature $\theta_D = 150(7)$ K was extracted. An estimation of the sound velocity was obtained using the Debye approximation (23)

$$v_s \approx (k_B \theta_D) / \hbar (6\pi^2 N)^{1/3}, \quad (3.1)$$

with resulting average sound velocity $v_s = 1530(30)$ m/s, where $N = 3.6 \cdot 10^{22}$ atoms/cm³ is the density of atoms for AgSbTe₂.

The ¹²¹Sb and ¹²⁵Te nuclear inelastic scattering in AgSbTe₂ has been measured at 30 K and 11, 30, and 60 K, respectively. The low temperature was chosen in order to decrease the multiphonon contributions to the inelastic spectra. The Sb and Te partial phonon density of states extracted from the inelastic spectra using conventional routine (24) are shown in Fig. 4.7. The partial Te and Sb DPS of AgSbTe₂ exhibit acoustical peaks at 6-8 meV, whereas the optical vibrations of Te and of Sb are most pronounced at 14 meV and at 18 meV, respectively. The acoustical range, E^{Ac} , is estimated, in first approximation, by $M_R/M_{Total} = \int_0^{E^{Ac}} g(E)d(E)$, where M_R is the mass of the resonant nucleus and M_{Total} is the total mass of the content of the primitive unit cell. The AgSbTe₂ acoustical region extend up to ~ 7.5 meV and, both DPS have high energy cut-off around 20 meV, consisting of broad features which are, probably, due to the stochastic distribution of the Sb and Ag atoms and/or because of phonon lifetime limitation.

The experimentally obtained DPS are compared in the Fig. 4.7 with partial DPS from first-principles calculations (5). The theoretical results show much sharper peaks than the experimentally observed for both Sb and Te atoms. This can be related to the ordering of the Sb ions possibly assumed in the first-principle calculations, which seems not to be the case for our sample. Moreover, the broadening of the theoretical DPS would be sufficient to describe the experimental Te DPS, but cannot correctly reproduce the Sb DPS, as a broadening and softening of the 10 meV peak, and hardening of the 18 meV peak would have to be applied to the theoretical Sb DPS in order to describe our experimental data. Similar effect, the softening of the low-energy modes and hardening of the high-energy modes has been observed experimentally for GeSb₂Te₄ compound (25) during transformation from the crystalline to amorphous state, related to a modification in the bond type from covalent to resonant. The observed difference between the theoretical and experimental Sb DPS in AgSbTe₂ could thus be related to different states of order of Ag and Sb considered for calculations and/or to a different type of bonding. The inset of Fig. 4.7 shows reduced DPS, $g(E)/E^2$, where the same Debye level is seen for Sb and Te vibrations. The Sb DPS mostly follows the Debye

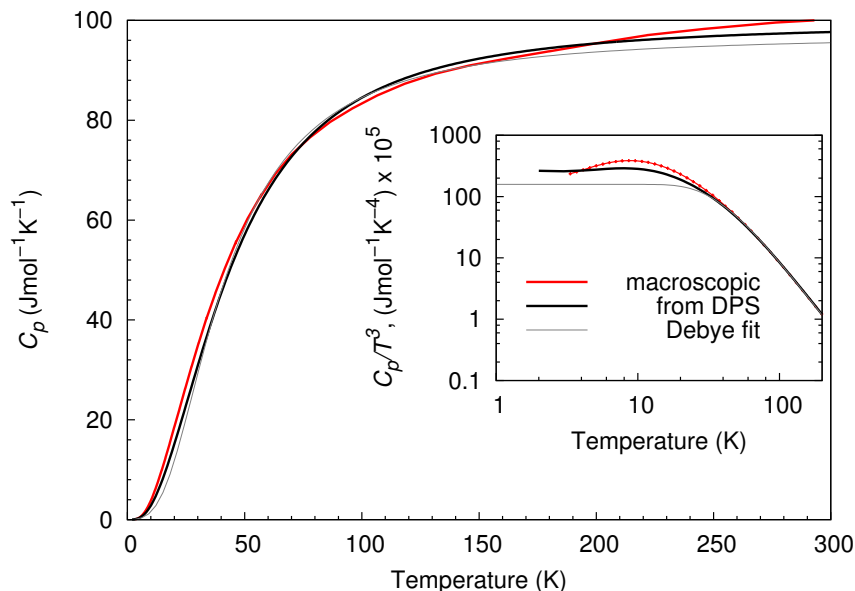


Figure 3.4: Macroscopically measured (red solid line) heat capacity AgSbTe_2 and the corresponding Debye model fit (gray). The total contribution of Ag, Sb and Te calculated from the DPS of AgSbTe_2 , assuming that Ag contribution to the heat capacity is similar to the Sb contribution, is presented in black.

behavior until ~ 7 meV whereas Te DPS shows a strong peak at 4 meV which is similar to the boson peak in glasses (26). The reason of such peak been observed only for Te atom is not clear. One explanation could be related to the presence of the $\text{Ag}_{4.5}\text{Te}_3$ phase. The large unit cell of this phase shifts the acoustic phonon modes to the low energies similarly to reported elsewhere (27). Thus, the enhancement of the reduced Te DPS at 4 meV can result from the van Hove singularity of the $\text{Ag}_{4.5}\text{Te}_3$ at this energy region; in total $\sim 10\%$ of the ^{125}Te DPS is related to this impurity.

Several different quantities can be directly accessed from the DPS, such as the force constant, Lamb-Mössbauer factor, atomic displacement parameter and the Debye temperature (15). From the relation

$$\lim_{E \rightarrow 0} \frac{g(E)}{E^2} = \frac{M_R}{2\pi^2 \hbar^3 \rho v_s^3}, \quad (3.2)$$

where M_R is the mass of the resonant atom and ρ the density, the additional information about average sound velocity v_s of the material is calculated. The average sound velocity $v_s = 1490(30)$ m/s of AgSbTe_2 was calculated from the Sb-DPS, to avoid the excessive ad-

3.3 Results and discussion

Table 3.2: Summary of the sound velocity, force constant, Lamb-Mössbauer factor, atomic displacement parameter and Debye's temperature in polycrystalline AgSbTe₂ calculated from the Sb- and Te-partial DPS.

	v_s (m/s)	F^M (N/m)	f_{LM} -	$\langle u^2 \rangle$ (10^{-3} \AA^2)	θ_D (K)
¹²¹ Sb 30 K	1490(30)	68(2)	0.31(3)	3.1(1)	161(10)
¹²⁵ Te 30 K	-	70(2)	0.43(2)	2.5(1)	151(5)

ditional phonon modes present due the secondary phase. But it is fair to assume that the obtained average sound velocity represents the whole material, since the low energy region is dominated by acoustic phonon modes.

The resulting properties, interatomic forces, Lamb-Mössbauer factor and atomic displacement, are presented in Table. 3.2. The validity of obtained properties was verified using the conventional sum rules (28). Interestingly, the atomic displacement parameter is larger for Sb as compared to Te, at 30 K. Note that NIS measurement yield a purely incoherent displacement parameter unaffected by the presence of vacancies, dislocations, etc.

The Debye temperature is an essential quantity which characterizes lattice related properties of materials. It is the temperature where the collective or acoustic vibrations switch to an independent thermal vibration, which means that the whole vibrational spectrum, up to the highest-energy phonons, is excited. From the partial DPS, with the relation

$$\theta_D^2 = 3/(k_B^2 \int_0^\infty \frac{g(E)}{E^2} dE), \quad (3.3)$$

the element specific Debye temperature $\theta_D = 161(10)$ K for Sb and $\theta_D = 151(5)$ K for Te were calculated, in good agreement with the obtained value from the macroscopic heat capacity. Those values are, however, higher than the one reported by Morelli (125 K) (2). Next to anharmonicity, low Debye temperature combined with a low sound velocity is directly related to the low thermal conductivity in AgSbTe₂. From the relation between the bulk modulus ($B = 45$ GPa (29)) and the calculated average sound velocity obtained from DPS, a longitudinal, v_l , and transversal, v_t , sound velocity of 3020(100) m/s and 1310(40) m/s, respectively, were calculated using

$$\frac{3}{v_s^3} = \frac{2}{v_t^3} + \frac{1}{v_l^3}, \quad (3.4)$$

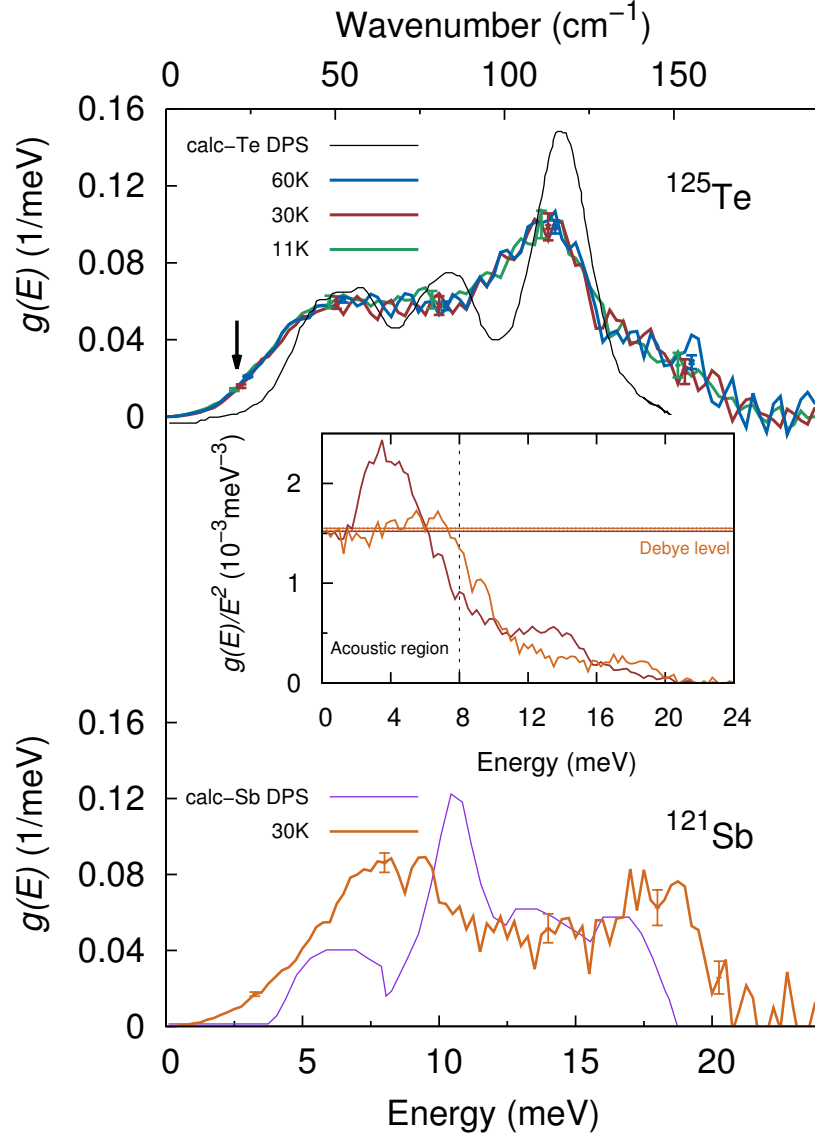


Figure 3.5: ^{125}Te -partial (top) and ^{121}Sb -partial DPS (bottom) for AgSbTe_2 , at 11K (green line), 30K (red line for ^{125}Te and orange line for ^{121}Sb) and 60K (blue line). The calculated partial DPS for Sb and Te, after Ref. (5), is presented as magenta and black lines, respectively. The arrow points the region at the experimental data with an excess of vibrational modes due the presence of the $\text{Ag}_{4.5}\text{Te}_3$ phase. The reduced partial DPS $g(E)/E^2$ in units of 10^{-3}meV^{-3} , and the low-energy fit between 0.5 and 6 meV for the Debye levels, indicated by the same type of lines, are shown in the inset.

in the Debye approximation. Finally, the elastic moduli $c_{11} = 65(10)$ GPa, $c_{44} = 12(10)$ GPa, and Poisson's ratio $\nu = 0.38(2)$ were calculated (30). Additionally, the dimensionless Grüneisen parameter γ (31) was estimated in order to quantify the crystal anharmonicity which strongly affects the behavior of the crystal lattice and the thermal conductivity in the material. $\gamma = 2.3$ at 300 K was calculated by

$$\gamma = \frac{3\alpha BV}{C_v}, \quad (3.5)$$

with the thermal expansion $\alpha = 25 \cdot 10^{-6} \text{ K}^{-1}$ obtained from our temperature dependence of the lattice parameter, the bulk modulus B (29), the molar unit cell volume $V_m = 3.38 \cdot 10^{-5} \text{ m}^3 \text{ mol}^{-1}$ and the measured heat capacity $C_p \sim C_v = 100.4 \text{ J} \cdot \text{mol}^{-1} \text{ K}^{-1}$, at 298 K. This is comparable to $\gamma = 2$, published by Morelli *et. al.* (2).

Phonon scattering mechanisms such as phonon-phonon interactions, defects and grain-boundaries scattering determine the κ_L in a material. At high temperature, heat-conducting phonons are usually mostly scattered by Umklapp processes. However, for AgSbTe₂, where κ is constant over a large range of temperature (32), the estimation of thermal conductivity considering only Umklapp processes can not be used, since in this approximation the thermal conductivity varies with $1/T$ (33). A simple temperature independent estimation of the lattice thermal conductivity of AgSbTe₂, κ_L , can be obtained by kinetic gas theory where $\kappa_L = c_v v_s^2 \tau / 3$, and depends only on the specific heat capacity c_v , the sound velocity v_s , and the phonon lifetime, τ . The phonon lifetime, $\tau = 0.45$ ps, is obtained using $\tau = 2\hbar/\text{FWHM}$, according to the Heisenbergs uncertainty principle where the full width at half maximum (FWHM) can be roughly estimated from our DPS data since no features sharper than ~ 3 meV are observed, both in the Sb and Te DPS. With $v_s = 1490(30)$ m/s, $c_v = 1.49 \cdot 10^6 \text{ J m}^{-3} \text{ K}^{-1}$, $\kappa_L = 0.50 \pm 0.05 \text{ W m}^{-1} \text{ K}^{-1}$ is obtained. This value is in good agreement with macroscopically measured thermal conductivity (20, 32) and the short phonon lifetime in combination with the very low sound velocity would appear to be the main contribution that explains the low thermal conductivity found in AgSbTe₂. A more direct determination of phonon lifetime broadening might be possible through inelastic neutron scattering if single crystalline AgSbTe₂ becomes available.

3.4 Conclusion

The partial ^{121}Sb and ^{125}Te DPS were experimentally obtained by nuclear inelastic scattering, at low temperatures. A comparison with the calculated partial DPS showed that Te DPS agrees fairly with our experimental data, whereas Sb DPS cannot correctly reproduce the experimental Sb DPS. This can be related to the ordering of the Sb ions in the first-principle calculations and resulting directional force constants, which seems not to be the case for our sample, in which an stochastic model is assumed. The calculated average mean force constant for Sb and Te, both of $\approx 70\text{ N/m}$, indicates very soft interatomic bonds, comparable to mean force constants of PbTe and SnTe (34), but smaller and therefore, softer, than *e.g.* Sb mean force constant in CoSb_3 (117 N/m) (27). The sound velocity in AgSbTe_2 of $v_s = 1490(30)\text{ m/s}$ is lower than in PbTe for which a $v_s = 1900(30)\text{ m/s}$ (35) is reported which indicates a softer bonding character of AgSbTe_2 compared to PbTe. The presence of $\text{Ag}_{4.3}\text{Te}_3$ as secondary phase add excess of phonon modes at low energy region (acoustic region) but overall does only contribute to $\sim 10\%$ of the Te DPS. In addition, the low Debye temperature, $\theta_D = 150(15)\text{ K}$ combined with the short phonon lifetime and the low sound velocity are key factors to the low thermal conductivity in AgSbTe_2 and are associated to the high thermoelectric performance in AgSbTe_2 containing systems.

3.5 Acknowledgements

We thank Mr. D. Bessas for his support during the NIS measurements. The European Synchrotron Radiation Facility and the Advanced Photon Source are acknowledged for provision of synchrotron radiation beam time at the nuclear resonance station ID18 and ID22N and high-energy station 6-IDD, respectively. The Federal Ministry for Education and Research of Germany (BMBF) is acknowledged for funding this research study in the project “NanoKoCh - Nanostructured Complex Chalcogenides” (03X3540) and the Helmholtz Gemeinschaft Deutscher Forschungszentren for funding of the Young Investigator Group “Lattice dynamics in emerging functional materials” VH NG-407.

References

- [1] A. F. BIRCH AND H. CLARK. **The thermal conductivity of rocks and its dependence upon temperature and composition.** *Am. J. of Science*, **238**:529–558, 1940. 43
- [2] D. T. MORELLI, V. JOVOVIC, AND J. P. HEREMANS. **Intrinsically minimal thermal conductivity in cubic I-V-VI2 semiconductors.** *Phys. Rev. Lett.*, **101**:035901, 2008. 43, 46, 51, 53
- [3] V. JOVOVIC AND J. P. HEREMANS. **Measurements of the energy band gap and valence band structure of AgSbTe₂.** *Phys. Rev. B*, **77**:245204, 2008. 43
- [4] J. XU, H. LI, B. DU, X. TANG, Q. ZHANG, AND C. UHER. **High thermoelectric figure of merit and nanostructuring in bulk AgSbTe₂.** *J. of Mater. Chem.*, **20**:6138–6143, 2010. 43
- [5] S. V. BARABASH, V. OZOLINS, AND C. WOLVERTON. **First-Principles Theory of Competing Order Types, Phase Separation, and Phonon Spectra in Thermoelectric AgPb_mSbTe_{m+2} Alloys.** *Phys. Rev. Lett.*, **101**:155704, 2008. xv, 43, 44, 45, 49, 52
- [6] R. DETEMPLE, D. WAMWANGI, M. WUTTIG, AND G. BIHLMAYER. **Identification of Te alloys with suitable phase change characteristics.** *Appl. Phys. Lett.*, **83**:2572, 2003. 43
- [7] C. STEIMER, W. WELNIC, J. KALB, AND M. WUTTIG. **Towards an atomistic understanding of phase change materials.** *J. of Optoelectr. and Adv. Mat.*, **8**:2044–2050, 2006. 43
- [8] M. WUTTIG AND N. YAMADA. **Phase-change materials for rewriteable data storage.** *Nature Mater.*, **6**:824–832, 2007. 43
- [9] E. QUAREZ, K. F. HSU, R. PCIONEK, N. FRANGIS, E. K. POLYCHRONIADIS, AND M. G. KANATZIDIS. **Nanostructuring, compositional fluctuations, and atomic ordering in the thermoelectric materials AgPbmSbTe_{2+m}: the myth of solid solutions.** *J. of the Am. Chem. Soc.*, **127**(25):9177–9190, 2005. 43, 46
- [10] K. HOANG, S. D. MAHANTI, J. R. SALVADOR, AND M. G. KANATZIDIS. **Atomic ordering and gap formation in Ag-Sb-based ternary chalcogenides.** *Phys. Rev. Lett.*, **99**:156403, 2007. 43
- [11] J. D. SUGAR AND D. L. MEDLIN. **Precipitation of Ag₂Te in the thermoelectric material AgSbTe₂.** *J. of All. and Comp.*, **478**(1-2):75–82, 2009. 43
- [12] D. M. ROWE, editor. *CRC Handbook of Thermoelectrics: Macro to Nano.* CRC Press, 1995. 44
- [13] K. F. HSU, S. LOO, F. GUO, W. CHEN, J. S. DYCK, C. UHER, T. HOGAN, E. K. POLYCHRONIADIS, AND M. G. KANATZIDIS. **Cubic AgPbmSbTe_{2+m}: bulk thermoelectric materials with high figure of merit.** *Science*, **303**(5659):818–821, 2004. 44
- [14] L.-H. YE, K. HOANG, A. J. FREEMAN, S. D. MAHANTI, J. HE, T. M. TRITT, AND M. G. KANATZIDIS. **First-principles study of the electronic, optical, and lattice vibrational properties of AgSbTe₂.** *Phys. Rev. B*, **77**:245203, 2008. 44
- [15] A. I. CHUMAKOV AND W. STURHAHN. **Experimental aspects of inelastic nuclear resonance scattering.** *Hyp. Int.*, **123-124**:781–808, 1999. 45, 50
- [16] J. RODRIGUEZ-CARVAJAL. **FULLPROF: a program for Rietveld refinement and pattern matching analysis.** In *Abs. Sat. Meet Powder Diff. XV Cong. IUCr p. 127*, 1990. 45
- [17] H.-C. WILLE, YU. V. SHVYD'KO, E. E. ALP, H. D. RÜTER, O. LEUPOLD, I. SERGUEEV, R. RFFER, A. BARLA, AND J. P. SANCHEZ. **Nuclear resonant forward scattering of synchrotron radiation from ¹²¹Sb at 37.13 keV.** *Europhys. Lett.*, **74**:170, 2006. 45
- [18] H.-C. WILLE, R. P. HERMANN, I. SERGUEEV, U. PELZER, A. MÔCHEL, T. CLAUDIO, J. PERSSON, R. RÜFFER, A. SAID, AND YU. V. SHVYD'KO. **Nuclear forward and inelastic spectroscopy on ¹²⁵Te and Sb₂¹²⁵Te₃.** *Europhys. Lett.*, **91**:62001–62006, 2010. 45

REFERENCES

- [19] I. SERGUEEV, H.-C. WILLE, R. P. HERMANN, D. BESSAS, YU. V. SHVYD'KO, M. ZAJAC, AND R. RÜFFER. **Milli-electronvolt monochromatization of hard X-rays with a sapphire backscattering monochromator.** *J. of Synchr. Rad.*, **18**:802–810, 2011. 45
- [20] H. WANG, J.-F. LI, M. ZOU, AND T. SUI. **Synthesis and transport property of AgSbTe₂ as a promising thermoelectric compound.** *Appl. Phys. Lett.*, **93**:202106, 2008. 46, 53
- [21] J. PETERS, O. CONRAD, B. BREMER, AND B. KREBS. **Die Kristallstruktur des synthetischen Sttzits, Ag(5-x)Te₃.** *Z. anorg. allg. Chem.*, **622**:1823–1832, 1996. 46
- [22] O. MADELUNG, U. RÖSSLER, AND M. SCHULZ, editors. *Landolt-Börnstein - Group III Condensed Matter*, **41E**, chapter AgSbTe₂ crystal structure, physical properties. SpringerMaterials - The Landolt-Börnstein Database, 2011. 46
- [23] R.P. HERMANN, F. GRANDJEAN, AND G. J. LONG. **Einstein oscillators that impede thermal transport.** *Am. J. of Phys.*, **73**:110–118, 2005. 46, 49
- [24] V. G. KOHN AND A. I. CHUMAKOV. **DOS: Evaluation of phonon density of states from nuclear resonant inelastic absorption.** *Hyp. Int.*, **125**:205–221, 2000. 49
- [25] T. MATSUNAGA, N. YAMADA, R. KOJIMA, S. SHAMOTO, M. SATO, H. TANIDA, T. URUGA, S. KOHARA, M. TAKATA, P. ZALDEN, G. BRUNS, I. SERGUEEV, H.-C. WILLE, R. P. HERMANN, AND M. WUTTIG. **Phase-change materials: vibrational softening upon crystallization and its impact on thermal properties.** *Adv. Funct. Mat.*, **21**(12):2232–2239, 2011. 49
- [26] F. R. DRYMIOTIS, S. LINDSEY, J. CAPPS, J. C. LASHLEY, D. RHODES, Q. R. ZHANG, C. NUCKLOS, AND T. B. DRYE. **Excess vibrational modes and high thermoelectric performance of the quenched and slow-cooled two-phase alloy Cu_{0.2}Ag_{2.8}SbSeTe₂.** *J. Phys. Condens. Matter.*, **23**:135305, 2011. 50
- [27] A. MÖCHEL, I. SERGUEEV, N. NGUYEN, GARY J. LONG, F. GRANDJEAN, D. C. JOHNSON, AND R. P. HERMANN. **Lattice dynamics in the FeSb₃ skutterudite.** *Phys. Rev. B*, **84**:064302, 2011. 50, 54
- [28] H. J. LIPKIN. **Mössbauer sum rules for use with synchrotron sources.** *Phys. Rev. B*, **52**:10073–10079, 1995. 51
- [29] R. S. KUMAR, A. L. CORNELIUS, E. KIM, Y. SHEN, S. YONEDA, C. CHEN, AND M. F. NICOL. **Pressure induced structural phase transition in AgSbTe₂.** *Phys. Rev. B*, **72**:060101, 2005. 51, 53
- [30] L. ZHANG, G. ROGL, A. GRYSIV, S. PUCHEGGER, J. KOPPENSTEINER, F. SPIECKERMANN, H. KABELKA, M. REINECKER, P. ROGL, W. SCHRANZ, M. ZEHETBAUER, AND M.A. CARPENTER. **Mechanical properties of filled antimonide skutterudites.** *Mat. Sci. and Eng.: B*, **170**:26–31, 2010. 53
- [31] H. LEDBETTER, A. LAWSON, AND A. MIGLIORI. **Alpha-plutonium's Grüneisen parameter.** *J. Phys.: Condens. Matter.*, **22**:165401, 2010. 53
- [32] D. T. MORELLI AND J. P. HEREMANS. **Thermal conductivity of germanium, silicon, and carbon nitrides.** *Appl. Phys. Lett.*, **81**:5126, 2002. 53
- [33] G.A. SLACK. **The thermal conductivity of nonmetallic crystals.** *Solid State Phys.*, **34**:1–71, 1979. 53
- [34] P. BAUER PEREIRA, R. P. HERMANN, I. SERGUEEV, S. GORSSE, J. DADDA, AND E. MÜLLER. **Lattice dynamics and structure of GeTe, SnTe and PbTe.** Submitted to Phys. Stat. Sol. B in Sep. 2012. 54
- [35] J. DADDA, E. MÜLLER, S. PERLT, T. HÖCHE, P. BAUER PEREIRA, AND R. P. HERMANN. **Microstructures and nanostructures in long-term annealed AgPb₁₈SbTe₂₀ (LAST-18) compounds and their influence on the thermoelectric properties.** *J. Mater. Res.*, **26**:1800–1812, 2011. 54

Chapter 4

Structure and Lattice dynamics in $\text{AgPb}_{18}\text{SbTe}_{20}$

Structure and Lattice dynamics in $\text{AgPb}_{18}\text{SbTe}_{20}$

P. Bauer Pereira^{1,2}, I. Sergueev³, J. Dadda⁴, E. Müller⁴, Raphaël P. Hermann^{1,2}

¹*Jülich Centre for Neutron Science JCNS and Peter Grünberg Institut PGI, JARA-FIT, Forschungszentrum Jülich GmbH, D-52425 Jülich, Germany*

²*Faculté des Sciences, Université de Liège, B-4000 Liège, Belgium*

³*European Synchrotron Radiation Facility, F-38043 Grenoble Cedex, France*

⁴*Deutsches Zentrum für Luft- und Raumfahrt, Institut für Werkstoff-Forschung, D-51147 Köln, Germany*

Abstract

We report on the average and local structure in bulk $\text{AgPb}_{18}\text{SbTe}_{20}$ alloy, known as LAST-18. Using a combined approach with Rietveld and Pair Distribution Function analysis, the presence of distinct amounts of randomly embedded nanostructures in a PbTe-matrix of an annealed and a quenched sample were identified. The lattice parameters of LAST-18 as a function of annealing temperature have been determined, and reveal the important effect of the synthesis on the properties of this family of compounds. Furthermore, ^{121}Sb and ^{125}Te partial density of phonons states were obtained by nuclear inelastic scattering in order to separately characterize the lattice dynamics from matrix and nanoinclusions. Additional characterization of the elastic properties and lattice governed properties were performed by resonance ultrasound spectroscopy, heat capacity and thermal expansion measurements.

PACS numbers: 66.70.Df, 63.20D-, 65.40.Ba, 61.05.C-, 65.40.De, 63.20.Ry

4.1 Introduction

An analysis of the energy efficiency, from automobile engines and power plants to industrial boilers, passing through computer processors and domestic devices, shows that only 30 to 50 % of the produced energy is really exploited as work whereas the large part is lost as heat (1). Thermoelectric (TE) generators can harvest part of this large amount of energy since they are capable of converting the waste heat in usable electricity. Since its discovery in the 19th century, despite its simplicity in design, scalability and reliability, thermoelectric technology has not fulfilled its whole potential in engineering applications mainly due the relatively low efficiency (<10 %) of commercially available materials (2). In order to fully benefit from all the advantages of TE devices, an improvement in the efficiency which the material converts heat into electricity is required.

A material's potential to convert heat into electricity is represented by its thermoelectric figure of merit Z (in units of K^{-1}). Z is directly related to the material's electrical conductivity σ and to the square of the Seebeck coefficient S , and inversely proportional to its thermal conductivity κ , where $\kappa = \kappa_E + \kappa_L$, the electronic and lattice contributions, respectively. Taking the working temperature T into consideration, the dimensionless figure-of-merit $ZT = (S^2\sigma/\kappa)T$ is defined (3). The major difficulty in improving ZT relies on the basic definition of a thermoelectric material being able both, to convert a thermal gradient in electricity and inversely, to generate a temperature difference when an electrical current is applied to the material. Therefore, a good thermoelectric must combine simultaneously high electronic mobility and a low thermal conductivity. Few materials can simultaneously fulfill these requirements. The list includes bulk materials such as clathrates (4, 5), skutterudites (6), half-Heusler (7) and chalcogenides alloys (8, 9, 10). Common attributes are identified in the latter materials such as (i) narrow energy gap in order to optimize the charge carriers concentration, (ii) complex crystal structure and/or heavy atoms in their atomic formula in order to disrupt the propagation of lattice vibrations by mass fluctuation scattering, and (iii) high mobility carriers for achieving the highest electrical conductivity for a given carrier concentration.

Over the years, different strategies have been used to optimize and increase ZT . One possible approach is to modify a known material, *e.g.*, with high electrical conductivity, by doping or by introduction of point defects as vacancies and substitutional atoms. The additional doping element or substitutional atom creates the necessary disorder to induce

increased phonon scattering which greatly reduces the thermal conductivity and thus the thermoelectric quality of the materials increases significantly. A classical example is the system Bi_2Te_3 and the solid solutions $\text{Bi}_{2-x}\text{Sb}_x\text{Te}_3$ and $\text{Bi}_2\text{Sb}_{3-x}\text{Se}_x$. By alloying Bi_2Te_3 with Sb or Se, a reduction close to 40% in thermal conductivity is achieved and ZT is increased from ~ 0.6 to $ZT \sim 1$, at 550 K (11, 12).

More recently, the use of nanostructured materials has provided another path for tuning ZT through different phenomena such as energy filtering, quantum confinement and phonon scattering at surfaces and interfaces (13). ZT values larger than 2 have been reported for artificially nanostructured materials grown by chemical vapour deposition (14, 15) or molecular beam epitaxy (MBE) (16, 17, 18, 19). However, the production of artificially nanostructured materials is time consuming and prohibitively expensive. Another problem is the difficulty in scaling up lab scale production to mass production by unconventional synthesis processes.

$\text{AgPb}_m\text{SbTe}_{m+2}$ (LAST- m) is a promising bulk material for TE applications at mid-range temperatures (500-700 K) with naturally formed nanoinclusions through conventional melt-route synthesis. High figure of merit, ~ 1.7 to 2.2, were reported (10, 20, 21). The system is derived from the combination of PbTe and AgSbTe_2 , and the properties can be tuned by modifying Ag, Sb and Pb fractions. It crystallizes in a cubic NaCl structure, where Ag, Pb and Sb occupy the cationic site, whereas Te sits at the anionic position. The presence of nanostructures and the compositional fluctuation in the matrix introduces inhomogeneity on the atomic and nanometric scales which are believed to act as scatterers for phonon propagation. This effect greatly reduce the thermal conductivity and ZT improves significantly, as compared to PbTe (20). However, this system presents a complex phase diagram, and the final properties will strongly depend on the synthesis conditions (10, 22, 23).

In this work, we report on the local and average structure and the lattice dynamics in bulk $\text{AgPb}_{18}\text{SbTe}_{20}$ (LAST-18). By combining Rietveld and Pair Distribution Function (PDF) analysis, the presence of distinct amounts of dispersed nanostructures in a PbTe-matrix in an annealed and a quenched sample were identified. The effect of the annealing temperature on the lattice parameter was also investigated, which confirms the important effect of the material's synthesis on the final structure parameters of this alloy. Furthermore, ^{121}Sb and ^{125}Te partial density of phonons states (DPS) were obtained by Nuclear Inelastic Scattering (NIS) in order to separately characterize the lattice dynamics from matrix and nanoinclusions. The experimental data is compared with theoretical calculation for

PbTe (24), and with LAST-18 time-of-flight inelastic neutron scattering data (25). From first principles calculations, it was reported that the calculated bulk thermodynamics favors the formation of coherent precipitates of ordered $\text{Ag}_m\text{Sb}_n\text{Te}_{m+n}$ phases, such as AgSbTe_2 (24) and that the DPS of the precipitates and matrix are mismatched in the acoustic energy range (24, 25), similarly as demonstrated for multilayered materials (14). Additional lattice dynamics related properties such as the mean force constant, atomic displacement parameters, the Lamb-Mössbauer factor and the average sound velocity are presented. Thermal expansion, heat capacity and elastic properties were also characterized since they are directly related to the thermal properties of the material and this information can help developing better designed thermoelectric materials and devices.

4.2 Experimental

Samples with nominal compositions $\text{AgPb}_{18}\text{SbTe}_{20}$ were produced by melting high purity (99.999 %) Ag, PbTe and Sb powder in quartz ampoules sealed under vacuum, in a rocking furnace at 1293 K. In order to ensure homogeneity, the melt was kept for 2 h at this high temperature and then, water quenched (WQ). In order to improve mechanical properties of the produced ingots, they were ground into powder, charged into a graphite die of 15 mm in diameter and short-term sintered in a direct-current sintering press at 673 K and 56 MPa. The obtained cylindrical sample was annealed in a temperature gradient (gradient annealing, GA) between 683 and 853 K (26), where each position represents a particular annealing temperature. Phase identification and structural characterization were performed by conventional X-ray diffraction (XRD) and by XRD using an approach similar to rapid acquisition pair distribution function (RA-PDF) (27) at the high energy station of the Advanced Photon Source. The X-ray energy used was 87.09 keV ($\lambda = 0.142519\text{\AA}$) and the detector was a General Electric amorphous silicon detector positioned at a distance of 1850(2) mm and 265(1) mm, for conventional XRD and RA-PDF, respectively. The sample to detector distances were calibrated using NIST640c silicon. To avoid saturation of the detector, each measurement exposure took 5 s and was repeated ten times to improve the counting statistics. The data were integrated and converted to intensity *versus* 2θ patterns with the program FIT2D (28), where 2θ is the angle between the incident and scattered X-rays. Background data including the empty sample container was also recorded and subtracted from the sample data during

the correction step. Additional corrections for multiple scattering, absorption and Compton scattering and processing of the integrated data to obtain the PDF, $G(r)$, were carried out using the PDFgetX2 program package (29). $G(r)$ was modeled over a range from 2 to 40 Å with the program PDFgui (30). Thermal expansion data was obtained by low-temperature XRD, from from 10 to 298 K, and were collected by a Huber G670 diffractometer, between 10 and 100°. The wavelength of the incident radiation was 1.5405 Å (Cu- k_α) and FullProf (31) was used to refine the atomic structure by Rietveld analysis. Heat capacity measurements between 3 and 298 K were performed using a Quantum Design Physical Property Measurement System, on a 16 mg sample. ^{121}Sb and ^{125}Te partial density of phonon states of LAST-18 were obtained by nuclear inelastic scattering, with the resonance energies of 37.13 (32) and 35.49 keV (33), respectively, at the ID18 station at the European Synchrotron Radiation Facility. Resolutions of 1.3 and 1.1 meV (34) were reached for ^{121}Sb and ^{125}Te , respectively. Mechanical characterization of LAST-18, at room temperature, was performed by Resonant Ultrasound Spectroscopy (RUS) (35, 36). In this technique, the elastic response of well-defined shape LAST-18 sample, *e.g.* a rectangular parallelepiped, was determined. The sample is held between two transducers, which one is the drive frequency emitter whereas the second detects the response of the sample. We evaluated 24 resonance frequencies, and the bulk and shear moduli, Poisson's ratio and the sound velocity were obtained.

4.3 Results and discussion

4.3.1 Structural characterization

The influence of the annealing temperature (T_{ann}) on the diffraction patterns of LAST-18 is presented in Fig. 4.1. The annealing temperature was defined by using a gradient annealing method, where a 40 mm long sintered sample rod was heat treated in an axial temperature gradient spanning between 683 K and 853 K, as reported elsewhere (26). The main phase, for all temperatures, has the nominal composition of LAST-18 and crystallizes in the $Fm\bar{3}m$ cubic structure, with lattice parameters ranging from 6.430 to 6.451 Å. More details on the annealing temperature used, sample identification, and on the obtained structural parameters and reliability factors from the Rietveld analysis are presented in Table 4.1.

For the presented annealing temperatures, except for $T_{ann} = 853$ K, Sb-metal is identified as secondary phase. It is observed that the weight fraction of the secondary phase in the matrix is reduced by increasing the annealing temperature, and a corresponding decrease in

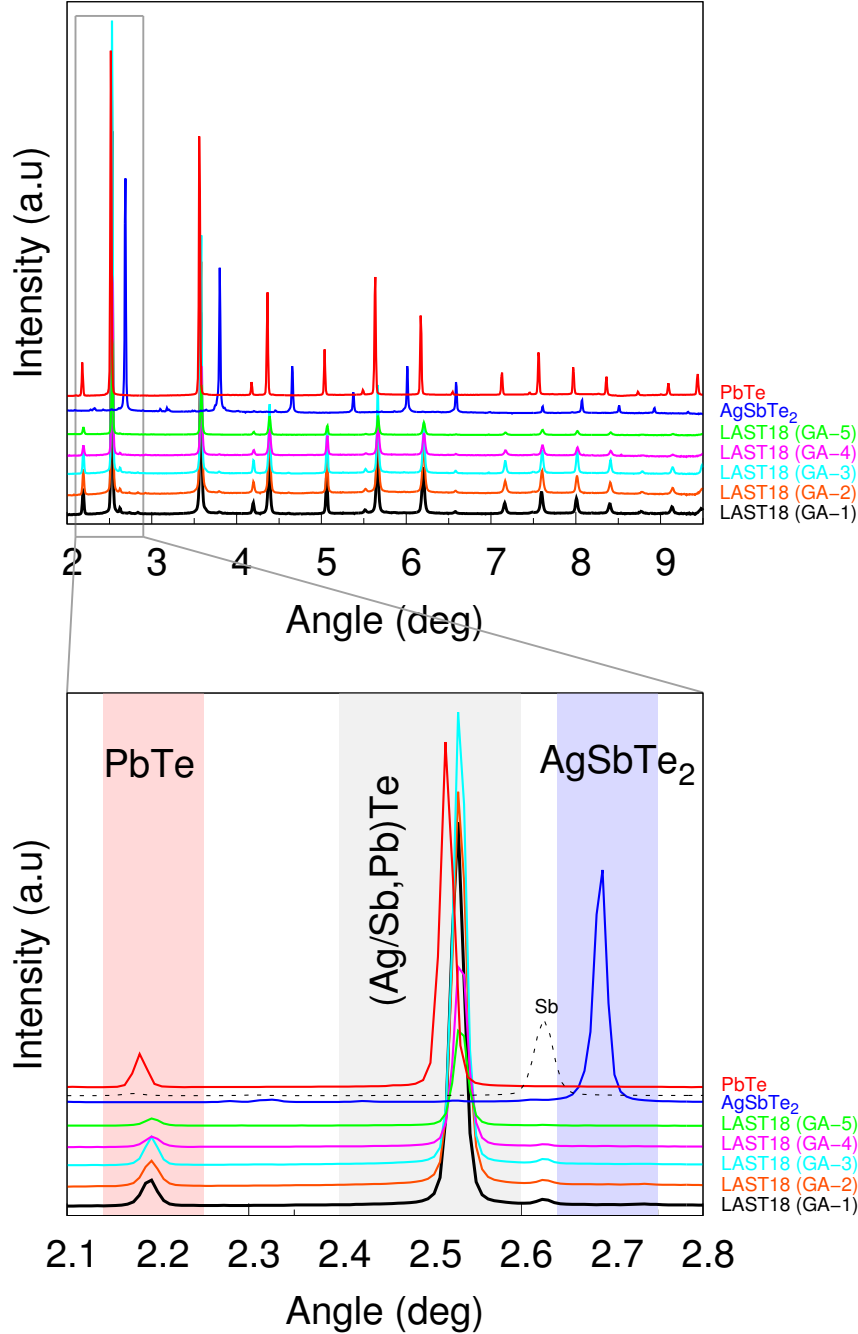


Figure 4.1: X-ray diffraction patterns, at room temperature, of LAST-18 samples obtained by gradient annealing method, along with those of the end-member (pure chalcogenides PbTe and AgSbTe₂) and Sb-metal (dashed line). The samples are identified as GA-1 (Gradient annealing-1), GA-2, GA-3, GA-4 and GA-5, according to their corresponding annealing temperature of 683, 738, 778, 798 and 853 K, respectively. In the bottom image, the Sb-peak at $\sim 2.62^\circ$ is seen to decrease, until it vanishes, with increasing the annealing temperature during synthesis of LAST-18.

intensity of the Sb-peak in the XRD patterns is seen, see Fig. 4.1 (bottom). This indicates the necessity of the annealing heat treatment to be performed, in the gradient annealing method, at temperatures higher than 798 K, in order to produce macroscopically homogeneous LAST-18 material. This result is consistent with previous reports based on scanning electronic microscopy observations (26, 37). The lattice parameter is also affected by the annealing temperature (Fig. 4.2). The lattice parameter is the largest for the water quenched sample ($a = 6.463 \text{ \AA}$), followed by the sample GA-1 heat treated at 683 K ($a = 6.451 \text{ \AA}$) and this value decreases, at first, as the annealing temperature is increased, reaching a minimum ($a = 6.430 \text{ \AA}$) for $T_{ann} = 798 \text{ K}$. A slightly increase is observed for the annealed temperature of 853 K, where a reaches 6.444 \AA . The difference can be explained by the Sb presence in the material in two different forms, as a precipitated secondary phase, until 798 K, and as solute atoms in the solutioned alloy, above 798 K. The larger lattice parameter of the sample annealed at 798 K is attributed to the increased concentration of dissolved Sb in the matrix, leading to a cell distortion. In a parallel study, the structures of $\text{AgPb}_6\text{SbTe}_8$ (LAST-6) and $\text{AgPb}_{10}\text{SbTe}_{12}$ (LAST-10) were investigated. As expected, the lattice parameters vary with m value and composition, with $a = 6.441(3) \text{ \AA}$ and $a = 6.444(3) \text{ \AA}$ for LAST-6 and LAST-10, respectively. Those are higher values than reported elsewhere (10), due to the differences in the synthesis conditions. The final properties are greatly affected by the alloy's composition and processing, which enables other degrees of freedom for optimization of the thermoelectric efficiency in these materials.

Table 4.1: Powder X-ray diffraction refined results and reliability factors, at room temperature, for $\text{AgPb}_{18}\text{SbTe}_{20}$ samples annealed at different temperatures along with a water quenched sample.

LAST-18							
Annealing temperature, K	Water quenched	683	723	738	778	798	853
Sample ID	WQ	GA-1	DLR2594	GA-2	GA-3	GA-4	GA-5
Crystal symmetry							
Space group							
Lattice parameter, Å	6.463(3)	6.451(3)	6.450(3)	6.449(3)	6.436(3)	6.430(3)	6.444(3)
Unit cell volume, Å ³	269.9(3)	268.5(3)	268.3(3)	268.2(3)	266.6(3)	265.8(3)	267.6(3)
Secondary phase	AgSbTe ₂	Sb	-	Sb	Sb	Sb	-
Secondary phase amount, wt%	< 5	10(3)	-	8(2)	5(2)	< 5	-
R _p (R-structure factor) %	14.	13.7	8.41	14.2	12.0	-	8.8
R _{wtp} (R-weighted pattern) %	17.1	14.6	9.62	15.2	13.5	-	16.9
R _{exp} (Expected error) %	24.1	29.5	21.9	28.5	29.8	-	60.0
Goodness-of-fit	0.50	0.24	0.19	0.29	0.21	6.55	0.1

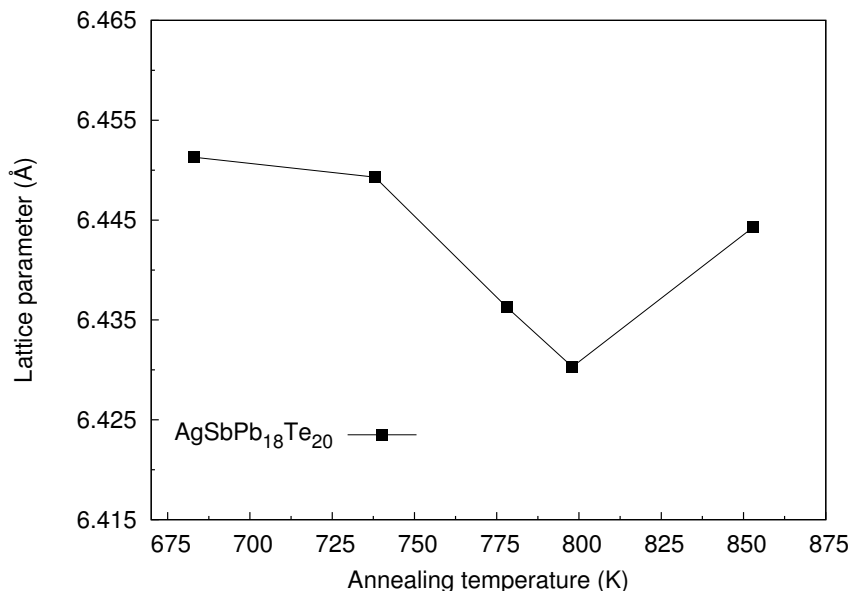


Figure 4.2: Dependence of the lattice parameter of $\text{AgPb}_{18}\text{SbTe}_{20}$ (LAST-18) on the annealing temperature. XRD data was collected at room temperature.

The structure and temperature dependence on the lattice constant of LAST-18 was further investigated by low-temperature XRD (Fig. 4.3) and thermal expansion was determined. The data was fitted using a third-order polynomial function without first order term, $a(T)$, in order to decrease the data noise, specially below 70 K. LAST-18 contracts linearly on cooling until ≈ 110 K. The thermal expansion is, calculated using $\alpha = (\partial a(T)/\partial T)/a_{(300\text{K})}$, is $19.3 \cdot 10^{-6} \text{ K}^{-1}$, at 300 K. This is in good agreement with Ren *et al.* (38), where α ranging between $20 \cdot 10^{-6} \text{ K}^{-1}$ and $24 \cdot 10^{-6} \text{ K}^{-1}$ measured independently by thermomechanical analysis and by high-temperature X-ray diffraction was reported. The measured value of α for LAST-18 is comparable to the values for other TE materials such as PbTe (39) and Bi_2Te_3 (40).

Traditional X-ray diffraction provides information on the long range average structure of the material under study, see Fig. 4.4(a) and (b). The presence of locally disordered regions is seen as diffuse scattering and broadening of the diffraction intensity profile which are usually discarded as scattering background. For a description of the local structure, the diffuse scattering contribution must be considered, therefore analysis of the corresponding atomic Pair Distribution Function, at room temperature, was also performed. PDF is a total scattering method that takes into account both Bragg and diffuse scattering information and gives structural information in real space on various length scales, including its local

structure (bond lengths and coordination number) and the average long range structure (41), in a full-profile method analogous to the Rietveld method.

The approach for the refinement is to start with a proper structure model, where the material's parameters (cell parameters, atomic positions in the unit cell and the average atomic occupancy of each site) are allowed to vary until a best fit of the calculated and the experimental PDF data is obtained. The agreement between calculated and experimental PDF is quantified by the residual function R_w (41). For the modeling, it is important that the used software, PDFgui, allows the refinement to be performed with multiple phases. Each phase has its own scale factor to be refined, which reflects the relative phase fraction in the multiphase system and any difference in the scattering power of the phases related to their compositions. The nanostructures in the PbTe-rich matrix, assumed to be a secondary phase, can be distinguished as long as the fit is made over a range of r , the atomic pairs separation distance, that is smaller than the particle size. For the LAST-18 water quenched sample (WQ) and annealed DLR2594 sample ($T_{ann} = 723$ K), different models were used. The first structural model is a homogeneous single phase with the PbTe composition, because PbTe and LAST-18 crystallize in the $Fm\bar{3}m$ structure and have similar lattice parameters. In the second model, complexity was added to the homogeneous single phased-PbTe model by introducing Ag and Sb atoms randomly distributed in the Na-occupation sites, according to the correct average composition of LAST-18; the cubic symmetry of the PbTe matrix was maintained. The third model is a two-phase model that intends to verify the presence of nanostructures in LAST-18. In this model, the main phase is a matrix of pure PbTe, whereas for the secondary phase, we have tried different compositions of LAST- m . The composition of the secondary phase was adjusted by varying m until a better fit with the experimental data was obtained, with resulting R_w value around 7.5%. No chemical ordering was attempted during modeling, and all refinements were performed over the range of PDF from 2 to 40 Å. From the modeling results, the presence of distinct amounts of nanostructures embedded in a PbTe-matrix in the annealed and a quenched sample were identified, indicating that different thermal treatments lead to a different amount of nanoinclusions in the LAST-18 samples. In the WQ sample, a low amount of nanoclusters ($\sim 0.2\%$) with average composition LAST-2 were identified in the PbTe-matrix, whereas in the annealed DLR2594 sample, 1.8% of nanoinclusions, with average composition LAST-10, were identified. As suggested by Lin *et al.* (42), the size, composition and the concentration of nanoclusters in the PbTe-matrix will depend strongly on the synthesis conditions.

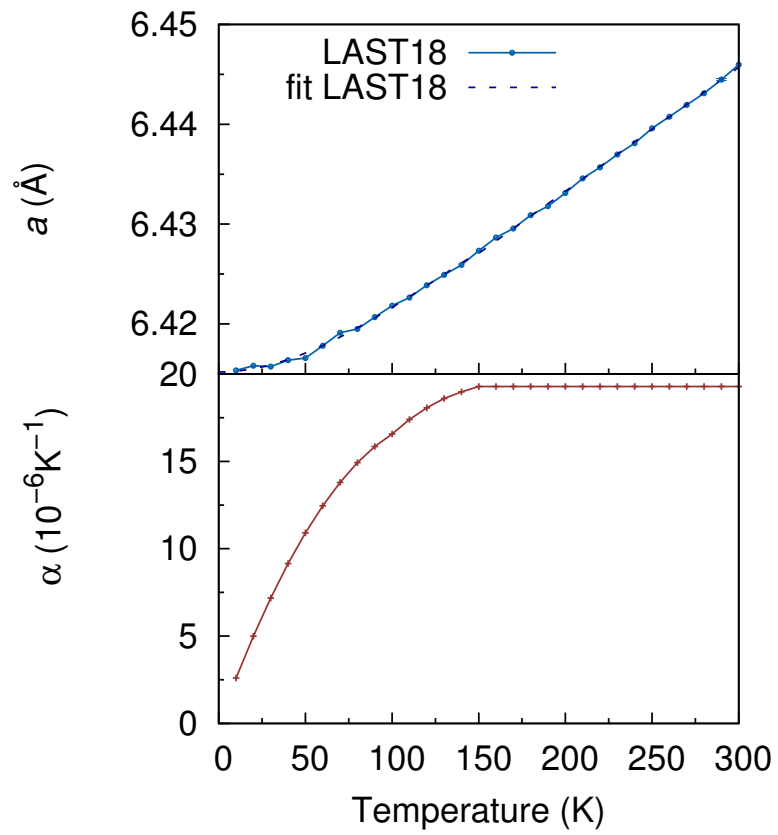


Figure 4.3: The influence of temperature on the lattice constants of LAST-18 (top), and the corresponding thermal expansion, α (bottom).

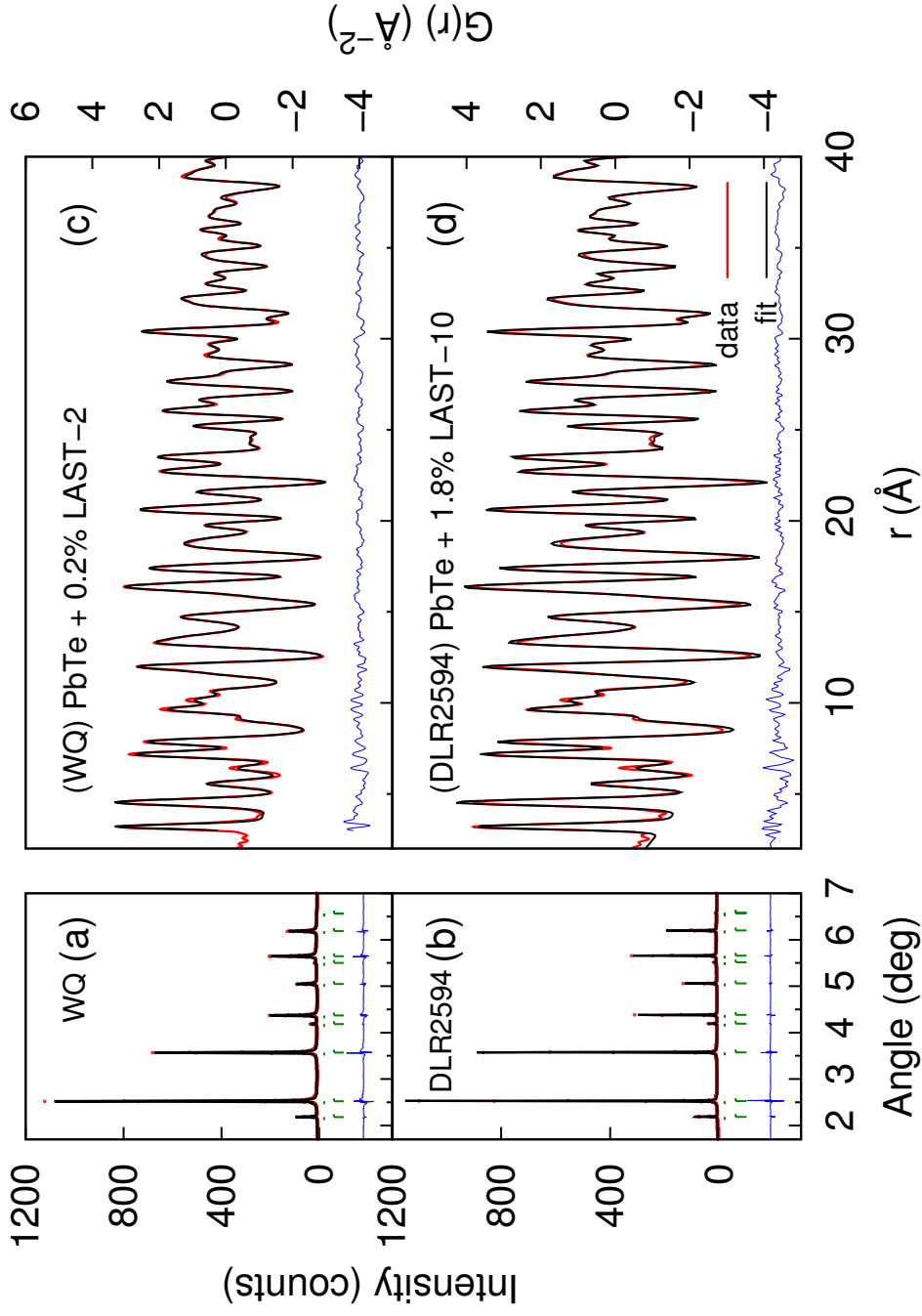


Figure 4.4: (a) X-ray powder diffraction of a water quenched (WQ) LAST-18 sample; the corresponding PDF data analysis with a two-phase model (PbTe -matrix with $\text{AgPb}_2\text{SbTe}_4$) is shown in (c). (b) X-ray powder diffraction from an annealed LAST-18 sample (DLR2594, $T_{\text{ann}} = 723 \text{ K}$); the corresponding PDF data analysis with a two-phase model (PbTe -matrix with $\text{AgPb}_{10}\text{SbTe}_{12}$) is shown in (d). Red line is the data, black line is the calculated curve from fitting, and the blue line in offset is their difference. In the X-ray diffraction patterns, the peak positions for main phases is depicted in green.

4.3.2 Lattice dynamics characterization

The measured heat capacity of LAST-18 (Fig. 4.5), at 298 K is $98.2 \text{ Jmol}^{-1}\text{K}^{-1}$, in good agreement with reported $C_p \sim 99.6 \text{ Jmol}^{-1}\text{K}^{-1}$ (20), at the same temperature. From the low temperature T^3 dependence of the heat capacity, a Debye temperature of $\theta_D = 130(10) \text{ K}$ was extracted, and the sound velocity was estimated using the Debye approximation (43)

$$v_s^3 \approx (k_B \theta_D) / \hbar (6\pi^2 N), \quad (4.1)$$

with resulting average sound velocity $v_s = 1400 \text{ m/s}$, where $N = 3 \cdot 10^{22} \text{ atoms/cm}^3$ is the density of atoms for LAST-18.

The ^{121}Sb and ^{125}Te nuclear inelastic scattering spectra from sample DLR2594 (LAST-18, annealed at 723 K) are presented in Fig. 4.6. The nuclear forward scattering (NFS, *i.e.*, elastic scattering) represents the instrumental function with a FWHM resolution of 1.3 and 1.1 meV for ^{121}Sb and ^{125}Te , respectively. The idea behind this measurement is to characterize the lattice properties of matrix (PbTe-rich) and nanoinclusions (Ag/Sb-rich) separately, and if possible, to confirm the elastic mismatch between the two terms, as proposed by Barabash *et al.* (24). Following the conventional procedure to extract the DPS from the inelastic scattering data (44), including the subtraction of the elastic peak, multiphonon correction, deconvolution of the data with the instrumental function, and finally the convolution of the data with a symmetric Gaussian, the partial contributions of Sb and Te for the DPS of sample DLR2594 were obtained and shown in Fig. 4.7 (c).

For comparison, experimental DPS of LAST-18 measured by time-of-flight (TOF) inelastic neutron scattering (25), at 7 and 300 K, along with the first-principles calculated DPS of pure PbTe (24) and the DPS of an alloy composed of PbTe plus 0.125 AgSbTe₂ (similar composition to LAST-16, with an excess of Te) (25), are also shown in Fig. 4.7 (a) and (b), respectively. The shape of the partial density of states obtained from the contributions of the Sb and Te ions are distinct and the vibrational energies of Sb contribution are higher than the ones from Te-contribution. The Sb DPS consists of two main regions centered at ~ 7.5 and 17.5 meV , whereas the Te DPS spectra consist of a main peak around 12 meV . Note the large differences in both Sb and Te DPS in the low energy acoustic range. The cut-off energies for Sb and Te-DPS are 16.1 and 20.6 meV, respectively.

As reported earlier (25), the overall agreement between the calculated DPS and data from TOF inelastic neutron scattering for LAST-18 is fairly good. The main features reported by

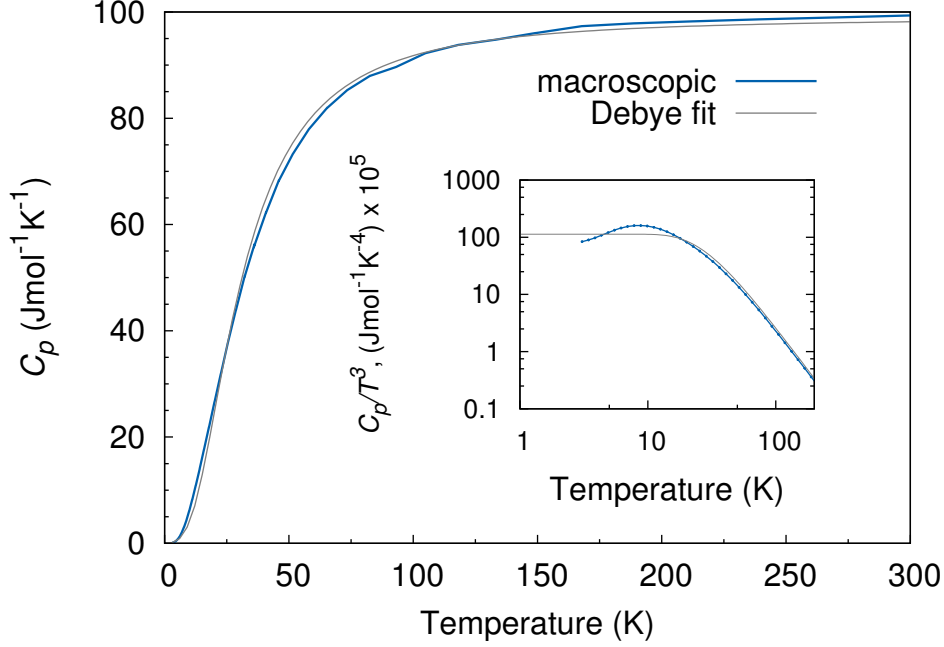


Figure 4.5: Macroscopically measured heat capacity (blue line) and the fit from the Debye model (light gray).

Barabash *et al.* (24) and Manley *et al.* (25) are two peaks, one at ~ 5 meV and other one at higher energies, around ~ 12 meV, and a cut-off energy of ~ 17.5 meV. However, those reports are not reproduced by our NIS data. The TOF measurements is partly insensitive to the small contributions of Sb and Ag, due to the cross section values of 3.9 and 4.99 barn, respectively, as compared to the Pb cross section of 11.18 barn, and also due the low content of Ag and Sb in LAST-18. Note that the energy cut-off for the theoretical prediction and TOF data matches with the cut-off energy of the Te DPS, whereas the Sb DPS extends up to higher values.

The reduced DPS, $g(E)/E^2$ in units of 10^{-3}meV^{-3} , for Sb and Te resonances, and the low energy fit, between 0 and 3 meV for the Debye levels are shown in Fig. 4.8. The sound velocity can be estimated from the Debye level $\lim_{E \rightarrow 0} g(E)/E^2$, in the Debye approximation (45), using

$$\lim_{E \rightarrow 0} g(E)/E^2 = M_R / (2\pi^2 \hbar^3 \rho v_s^3), \quad (4.2)$$

where M_R is the mass of the resonant atom and ρ the density ρ is the density of the material.

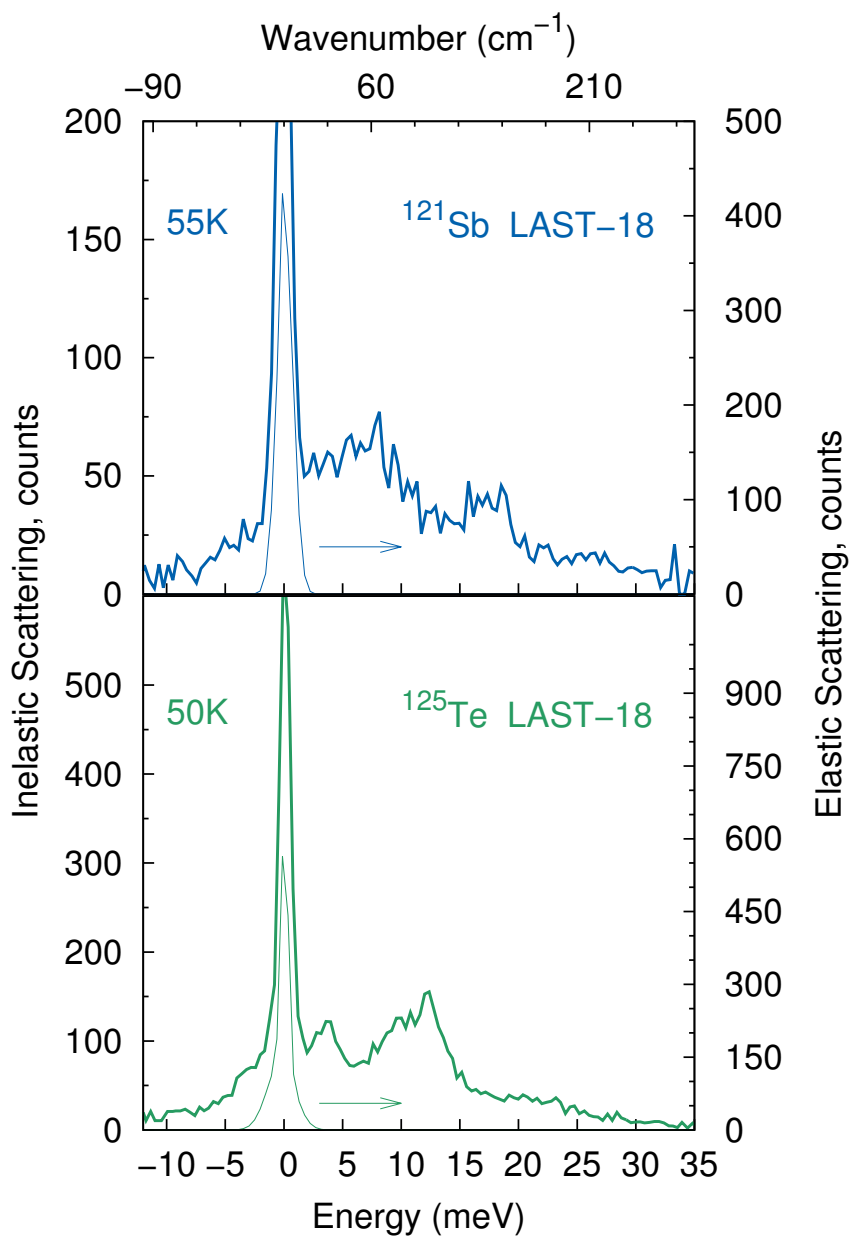


Figure 4.6: The nuclear inelastic scattering, NIS, spectra and the instrumental functions, measured by nuclear forward scattering, NFS, obtained with the ^{121}Sb (top) and ^{125}Te resonance for sample DLR2594 (bottom).

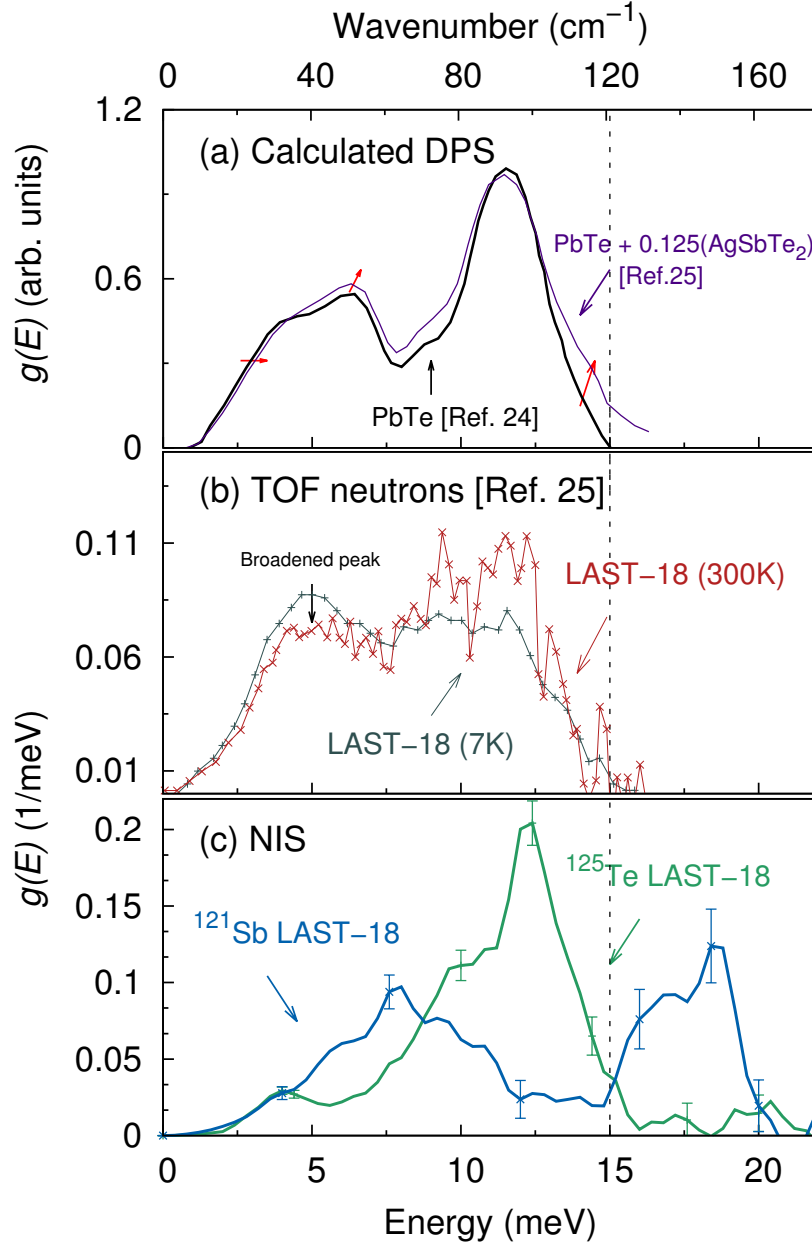


Figure 4.7: (a) Calculated DPS of PbTe (24) and (PbTe + 0.125 AgSbTe₂) alloy (25) and, (b) DPS of LAST-18 measured by time-of-flight (TOF) inelastic neutron scattering (25), at 7 and 300 K. (c) The element specific DPS measured with the ¹²¹Sb (blue line) and ¹²⁵Te (green line) resonances for sample DLR2594, at 55 and 50 K, respectively. The dashed line crossing the three graphics indicate the mismatch between the energy cut-off obtained by theoretical calculations and TOF, with the NIS data.

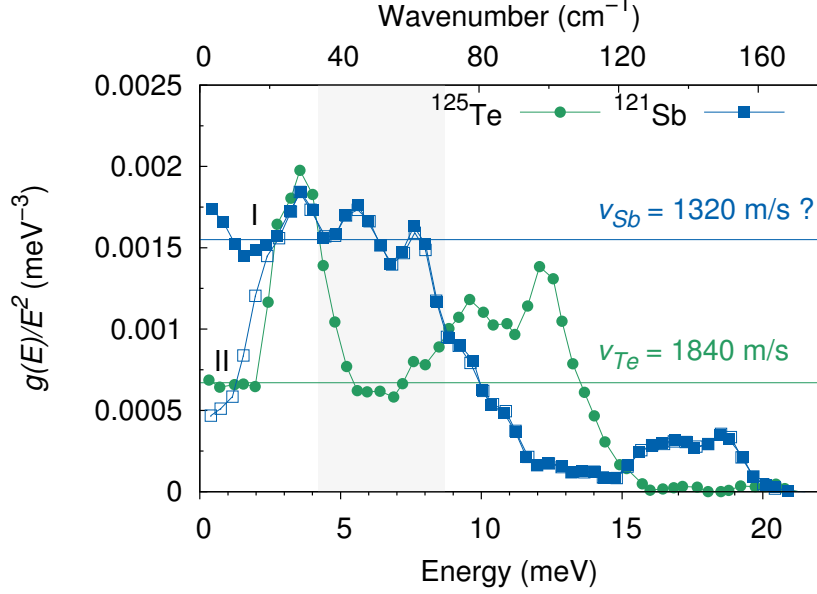


Figure 4.8: The reduced partial DPS of DLR2594, $g(E)/E^2$, and the low energy fit, between 0 and 3 meV, for the Debye levels, indicated by the same type of lines. The regions marked with I and II show two possible Debye levels for the Sb contribution, that depend of the subtracting procedure of the elastic line from the inelastic scattering data for Sb in LAST-18. The shaded are between 4.2 and 8.7 meV reveals a mismatch in the acoustic region between the Sb and Te reduced DPS.

The average sound velocity $v_s = 1840(60)$ m/s of LAST-18 was calculated from the Te DPS. Due to the instrumental energy resolution of 1.3 meV for the Sb DPS, it was observed that the reduced DPS below 2 meV is strongly affected by the subtraction of the elastic line from the inelastic scattering data. This is represented in Fig. 4.8 by the two possible Debye levels for Sb marked as *I* and *II*, depending on the degree of subtraction of the elastic peak. Therefore, a sound velocity mismatch between the matrix (mainly probed by the ^{125}Te resonance) and nanoinclusions (probed by ^{121}Sb) could not be directly confirmed or disproved by observing the difference in the Debye level from Sb and Te reduced DPS. Further investigation is required, on samples with larger Sb content and with improved instrumental energy resolution. However, a large difference in the number of phonon modes in the reduced Sb and Te DPS is observed between 4.2 and 8.7 meV, which confirms the mismatch in the acoustic range of the DPS of matrix and nanostructures suggested by Barabash *et. al.* (24).

We also compare the Sb and Te DPS data of LAST-18 with our previous results in AgSbTe₂ (46) and in PbTe (47), respectively, see Fig. 4.9. The similarities between the

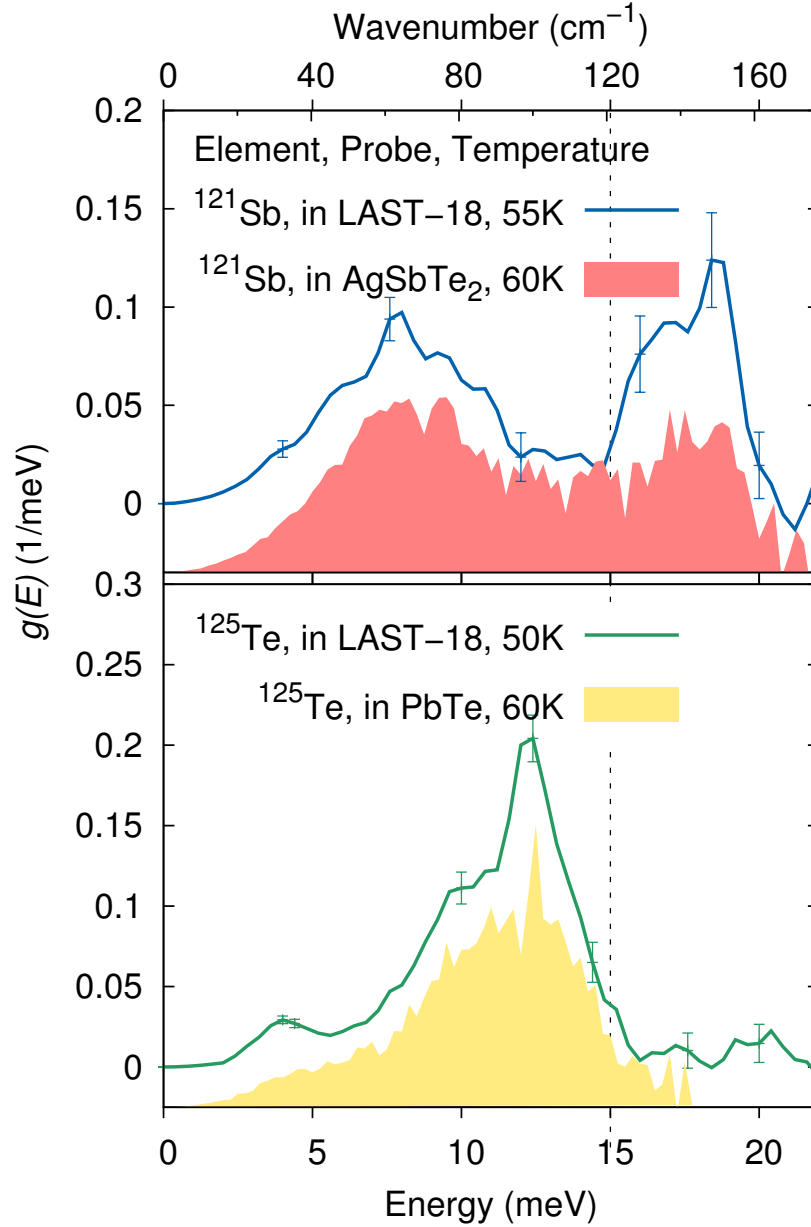


Figure 4.9: Comparison between the Sb DPS of LAST-18 and the Sb DPS of AgSbTe_2 (46) (top) and the partial Te DPS of LAST-18 compared to the partial DPS of PbTe (47) (bottom).

4.3 Results and discussion

Table 4.2: Summary of the sound velocity v_s , force constant F^M , Lamb-Mössbauer factor f_{LM} , atomic displacement parameter $\langle u^2 \rangle$ and Debye's temperature θ_D in polycrystalline LAST-18 calculated from the Sb- and Te-partial DPS.

	T (K)	v_s (m/s)	F^M (N/m)	f_{LM} -	$\langle u^2 \rangle$ (\AA^2) at T	θ_D (K)
^{121}Sb	50	-	50(3)	0.37(2)	0.0030(5)	160(5)
^{125}Te	55	1840(60)	90(5)	0.36(2)	0.0029(4)	165(5)

Table 4.3: Longitudinal and transversal sound velocities and elastic properties of polycrystalline LAST-18 obtained by RUS, at room temperature.

Young's modulus E (GPa)	Bulk modulus B (GPa)	Poisson's ratio ν	v_s (m/s)	v_l (m/s)	v_s (m/s)
68(1)	37(2)	0.24(1)	1900(50)	2885(60)	1685(40)

spectrum of Sb in AgSbTe₂ and Sb in LAST-18 are clearly seen. The main peaks and the minimum around 13 meV are present in the two compounds. Similarly, the Te-DPS in PbTe and the Te-DPS in LAST-18 exhibit similar features, and the same energy range. The sound velocities reported for Sb AgSbTe₂ and Te PbTe are, 1490(30) and 1700(100) m /s. This indicates a difference in the atomic environment and in the elastic forces between atoms, leading to distinct sound velocities and lattice properties.

In addition to the sound velocity, other vibrational quantities can be obtained from the DPS (45), such as the interatomic forces constants, the Lamb-Mössbauer factor and atomic displacements. The values are summarized in Table 4.2. From NIS data, the average Debye, θ_D , of 160(5) and 165(5) K were calculated, for Sb and Te resonances, respectively, using

$$\theta_D^2 = 3/(k_B^2 \int_0^\infty g(E)dE^2). \quad (4.3)$$

These values are in good agreement with report for LAST-18 by Kosuga *et al.* (48), where θ_D for Ag_xPb₁₈SbTe₂₀ ($x=0.7, 0.9$ and 1) varied between 132 and 170 K .

The elastic properties of LAST-18 were characterized by resonant ultrasound spectroscopy, at room temperature. A typical RMS error between observed and computed frequencies of 0.45 % was obtained including 24 modes. The elastic constants, c_{11} and c_{44} , are directly obtained from this technique, and have values of 67.6(0.5) and 23.1(0.5) GPa, re-

spectively. The shear modulus G is equal to c_{44} . With c_{11} and c_{44} , the Young modulus, $E = (3c_{44}c_{11} - 4c_{44}^2)/(c_{11} - c_{44})$, Poisson ratio, $\nu = (E/2G) - 1$, and the bulk modulus, $B = E/(3(1 - 2\nu))$, were calculated. The isotropic average of the longitudinal and the transversal velocity of sound were obtained by $v_l^2 = c_{11}/\rho$ and $v_t^2 = c_{44}/\rho$, respectively, where $\rho = 8.12 \text{ g/cm}^3$ is the density of the material. The mean velocity of sound was calculated using $3/v_s^3 = (2/v_t^3 + 1/v_l^3)$, in the Debye approximation. The resulting values are summarized in Table 4.3. The sound velocity obtained from the RUS data, $v_s = 1900(40) \text{ m/s}$, is in good agreement with the value of $1840(60) \text{ m/s}$ obtained by NIS, and with report from Kosuga *et al.* (48), where v_s between 1810 and 1920 m/s were obtained.

Additionally, the dimensionless Grüneisen parameter (49), γ , was estimated in order to quantify the crystal anharmonicity which strongly affects the behavior of the crystal lattice and the thermal conductivity in the material. A γ value of ~ 1.9 , at 300 K , was calculated by

$$\gamma = \frac{3\alpha BV}{C_v}, \quad (4.4)$$

with the thermal expansion $\alpha = 25 \cdot 10^{-6} \text{ K}^{-1}$, the bulk modulus $B = 38 \text{ GPa}$, the molar unit cell volume $V_m = 3.38 \cdot 10^{-5} \text{ m}^3 \text{ mol}^{-1}$, and assuming $C_v \sim C_p$, and the measured heat capacity $C_p = 98.2 \text{ Jmol}^{-1}\text{K}^{-1}$, at 298 K . This is comparable to the value of $\gamma \approx 2.05$ for AgSbTe_2 , published by Morelli (50).

4.4 Conclusion

The partial ^{121}Sb and ^{125}Te DPS were obtained by nuclear inelastic scattering, at low temperatures. A comparison of our data with previous reports from first-principles calculations (24, 25) and time-of-flight inelastic neutron scattering data (25) showed a great discrepancy between these data and NIS, specially concerning the energy cut-off for Sb. This difference can be related to the greater Pb contribution, with the largest cross section of the containing LAST-18 atoms, observed by neutrons, and also due to the low amount of Ag and Sb in LAST-18. We also observed many similarities between the spectrum of Sb in AgSbTe_2 and Sb in LAST-18, and between the Te-DPS of PbTe and the Te-DPS of LAST-18. However, the sound velocities of AgSbTe_2 and PbTe are $1490(30)$ (46) and $1700(100) \text{ m/s}$ (47), respectively, whereas LAST-18 sound velocity is $1840(60) \text{ m/s}$. The expected sound velocity mismatch between PbTe-rich matrix and nanoinclusions could not be confirmed nor disproved, but a

difference in the acoustical region for Sb and Te contributions is seen, revealing the mismatch in the acoustic range of the DPS of matrix and nanostructures. The lattice parameters and phase homogeneity of LAST-18 samples annealed in a gradient temperature between 683 and 853 K have been determined as a function of annealing temperature, which points to the necessity of the annealing treatment to be performed at temperatures higher than 798 K for producing macroscopically homogeneous LAST-18 material without the presence of Sb as secondary phase. The average and local structure in bulk $\text{AgPb}_{18}\text{SbTe}_{20}$ was studied by PDF analysis, where the presence of distinct amounts of nanostructures embedded in a PbTe-matrix in an annealed and a quenched sample were identified. As suggested by Lin et al. (42), the size, composition and the concentration of nanoclusters in the PbTe-matrix, as well as the final properties, will depend strongly on the synthesis conditions.

4.5 Acknowledgements

We thank Mr. D. Bessas for his support during the NIS measurements. The European Synchrotron Radiation Facility and the Advanced Photon Source are acknowledged for provision of synchrotron radiation beam time at the nuclear resonance station ID18 and ID22N and high-energy station 6-IDD, respectively. Dr. K. Friese is acknowledged for the fruitful discussions concerning structural analysis, and Dr. S. Disch for her help with the PDF analysis. The authors acknowledge the Federal Ministry for Education and Research of Germany (BMBF) for funding this research in the project “NanoKoCh - Nanostructured Complex Chalcogenides” (03X3540) and the Helmholtz Gemeinschaft Deutscher Forschungszentren for funding of the Young Investigator Group “Lattice dynamics in emerging functional materials” VH NG-407.

References

- [1] BCS INCORPORATED. **Waste Heat Recovery: Technology and Opportunities in U.S. Industry**. Technical report, U.S. Department of Energy - Industrial Technologies Program, 2008. 59
- [2] D. M. ROWE, editor. *CRC Handbook of Thermoelectrics: Macro to Nano*. CRC Press, 1995. 59
- [3] A. F. IOFFE. *Semiconductor Thermoelements and Thermoelectric Cooling*. Infosearch Ltd, 1957. 59
- [4] W. JEITSCHKO AND D. BRAUN. **LaFe₄P₁₂ with filled CoAs₃-type structure and isotypic lanthanoid-transition metal polyphosphides**. *Acta Cryst.*, **B33**:3401–3406, 1977. 59
- [5] G. S. NOLAS, G. A. SLACK, AND S. B. SCHUJMAN. **Chapter 6: Semiconductor clathrates - A phonon glass electron crystal material with potential for thermoelectric applications**. In TERRY M. TRITT, editor, *Recent Trends in Thermoelectric Materials Research II*, **69** of *Semiconductors and Semimetals*, pages 255 – 300. Elsevier, 2001. 59
- [6] G. S. NOLAS, D. T. MORELLI, AND TERRY M. TRITT. **Skutterudites: a phonon-glass-electron-crystal approach to advanced thermoelectric energy conversion applications**. *Annual Rev. of Mater. Science*, **29**:89–116, 1999. 59
- [7] G. J. POON. **Chapter 2 Electronic and thermoelectric properties of Half-Heusler alloys**. In TERRY M. TRITT, editor, *Recent Trends in Thermoelectric Materials Research II*, **70** of *Semiconductors and Semimetals*, pages 37 – 75. Elsevier, 2001. 59
- [8] D. A. WRIGHT. **Thermoelectric properties of bismuth telluride and its alloys**. *Nature*, **181**(4612):834, 1958. 59
- [9] S. K. PLACHEOVA. **Thermoelectric figure of merit of the system (GeTe)_{1-x}(AgSbTe₂)_x**. *Phys. Status Solidi A*, **83**:349–355, 1984. 59
- [10] K. F. HSU, S. LOO, F. GUO, W. CHEN, J. S. DYCK, C. UHER, T. HOGAN, E. K. POLYCHRONIADIS, AND M. G. KANATZIDIS. **Cubic AgPbmSbTe_{2+m}: bulk thermoelectric materials with high figure of merit**. *Science*, **303**(5659):818–821, 2004. 59, 60, 64
- [11] G. S. NOLAS, J. POON, AND M. KANATZIDIS. **Recent developments in bulk thermoelectric materials**. *MRS Bulletin*, **31**:199–205, 2006. 60
- [12] T. M. TRITT AND M. A. SUBRAMANIAN. **Thermoelectric materials, phenomena, and applications: a bird’s eye view**. *MRS Bulletin*, **31**:188–198, 2006. 60
- [13] L. D. HICKS AND M. S. DRESSELHAUS. **Effect of quantum-well structures on the thermoelectric figure of merit**. *Phys. Rev. B*, **47**(19):12727–12731, 1993. 60
- [14] R. VENKATASUBRAMANIAN, E. SILVOLA, T. COLPITTS, AND B. O’QUINN. **Thin-film thermoelectric devices with high room-temperature figures of merit**. *Nature*, **413**:597–602, 2001. 60, 61
- [15] J. C. CAYLOR, K. COONLEY, J. STUART, T. COLPITTS, AND R. VENKATASUBRAMANIAN. **Enhanced thermoelectric performance in PbTe-based superlattice structures from reduction of lattice thermal conductivity**. *Appl. Phys. Lett.*, **87**(2):023105, 2005. 60
- [16] T. C. HARMAN, P. J. TAYLOR, M. P. WALSH, AND B. E. LAFORGE. **Quantum dot superlattice thermoelectric materials and devices**. *Science*, **297**(5590):2229–2232, 2002. 60
- [17] H. BEYER, J. NURNUS, H. BÖTTNER, A. LAMBRECHT, T. ROCH, AND G. BAUER. **PbTe based superlattice structures with high thermoelectric efficiency**. *Appl. Phys. Lett.*, **80**:1216, 2002. 60
- [18] T. C. HARMAN, M. P. WALSH, B. E. LAFORGE, AND G. W. TURNER. **Nanostructured thermoelectric materials**. *J. of Electr. Mat.*, **34**:L19–L22, 2005. 60
- [19] J. R. SOOTSMAN, R. J. PCIONEK, H. KONG, C. UHER, AND M. G. KANATZIDIS. **Strong reduction of thermal conductivity in nanostructured PbTe prepared by matrix encapsulation**. *Chem. of Mater.*, **18**:4993–4995, 2006. 60

REFERENCES

- [20] M. ZHOU, J.-F. LI, AND T. KITA. **Nanostructured AgPbmSbTem+2 system bulk materials with enhanced thermoelectric performance.** *J. Am. Chem. Soc.*, **130**(13):4527–4532, 2008. 60, 70
- [21] H. WANG, J.-F. LI, C.-W. NAN, M. ZHOU, W. LIU, B.-P. ZHANG, AND T. KITA. **High-performance Ag0.8Pb18SbTe20 thermoelectric bulk materials fabricated by mechanical alloying and spark plasma sintering.** *Appl. Phys. Lett.*, **88**(9):092104, 2006. 60
- [22] T. J. ZHU, F. YAN, S. N. ZHANG, AND X. B. ZHAO. **Microstructure and electrical properties of quenched AgPb18Sb(1-x)Te20 thermoelectric materials.** *J. of Phys. D: Appl. Phys.*, **40**(11):3537–3540, 2007. 60
- [23] H. S. DOW, M. W. OH, S. D. PARK, B. S. KIM, B. K. MIN, H. W. LEE, AND D. M. WEE. **Thermoelectric properties of AgPbmSbTe(m+2) at elevated temperature.** *J. Appl. Phys.*, **105**(11):113703, 2009. 60
- [24] S. V. BARABASH, V. OZOLINS, AND C. WOLVERTON. **First-Principles Theory of Competing Order Types, Phase Separation, and Phonon Spectra in Thermoelectric AgPbmSbTem+2 Alloys.** *Phys. Rev. Lett.*, **101**:155704, 2008. xvi, 61, 70, 71, 73, 74, 77
- [25] M. E. MANLEY, S. SHAPIRO, Q. LI, A. LLOBET, AND M. E. HAGEN. **Lattice dynamical origin of peak thermoelectric performance in AgPbmSbTe2+m observed by inelastic neutron scattering.** *J. Appl. Phys.*, **109**:083722, 2011. xvi, 61, 70, 71, 73, 77
- [26] J. DADDA, E. MÜLLER, S. PERLT, T. HÖCHE, P. BAUER PEREIRA, AND R. P. HERMANN. **Microstructures and nanostructures in long-term annealed AgPb18SbTe20 (LAST-18) compounds and their influence on the thermoelectric properties.** *J. Mater. Res.*, **26**:1800–1812, 2011. 61, 62, 64
- [27] P. J. CHUPAS, X. QIU, J. C. HANSON, P. L. LEE, C. P. GREY, AND S. J. L. BILLINGE. **Rapid-acquisition pair distribution function (RA-PDF) analysis.** *J. of Appl. Cryst.*, **36**:6, 2003. 61
- [28] A. P. HAMMERSLEY. **FIT2D: An Introduction and Overview.** ESRF Internal Report ESRF97HA02T, ESRF, 1997. 61
- [29] X. QIU, JEROEN W. THOMPSON, AND S. J. L. BILLINGE. **PDFgetX2: a GUI-driven program to obtain the pair distribution function from X-ray powder diffraction data.** *J. of Appl. Cryst.*, **37**(4):678, 2004. 62
- [30] C. L. FARROW, P. JUHAS, J. W. LIU, D. BRYNDIN, E. S. BOZIN, J. BLOCH, TH. PROFFEN, AND S. J. L. BILLINGE. **PDFfit2 and PDFgui: computer programs for studying nanostructure in crystals.** *J. of Phys.: Cond. Matter*, **19**(33):335219, 2007. 62
- [31] J. RODRIGUEZ-CARVAJAL. **FULLPROF: a program for Rietveld refinement and pattern matching analysis.** In *Abs. Sat. Meet Powder Diff. XV Cong. IUCr p. 127*, 1990. 62
- [32] H.-C. WILLE, YU. V. SHVYD'KO, E. E. ALP, H. D. RÜTER, O. LEUPOLD, I. SERGUEEV, R. RFFER, A. BARLA, AND J. P. SANCHEZ. **Nuclear resonant forward scattering of synchrotron radiation from 121Sb at 37.13 keV.** *Europhys. Lett.*, **74**:170, 2006. 62
- [33] H.-C. WILLE, R. P. HERMANN, I. SERGUEEV, U. PELZER, A. MÖCHEL, T. CLAUDIO, J. PERSSON, R. RÜFFER, A. SAID, AND YU. V. SHVYD'KO. **Nuclear forward and inelastic spectroscopy on 125Te and Sb2125Te3.** *Europhys. Lett.*, **91**:62001–62006, 2010. 62
- [34] I. SERGUEEV, H.-C. WILLE, R. P. HERMANN, D. BESSAS, YU. V. SHVYD'KO, M. ZAJAC, AND R. RÜFFER. **Milli-electronvolt monochromatization of hard X-rays with a sapphire backscattering monochromator.** *J. of Synchr. Rad.*, **18**:802–810, 2011. 62
- [35] A. MIGLIORI, J. L. SARRAO, W. M. VISSCHER, T. M. BELL, M. LEI, Z. FISK, AND R. G. LEISURE. **Resonant ultrasound spectroscopic techniques for measurement of the elastic moduli of solids.** *Physica B*, **183**:1–24, 1993. 62
- [36] A. MIGLIORI AND J. L. SARRAO. *Resonant Ultrasound Spectroscopy: Applications to Physics, Materials Measurements, and Nondestructive Evaluation.* Wiley-Interscience, 1 edition edition, 1997. 62
- [37] S. PERLT, T. HÖCHE, J. DADDA, E. MÜLLER, P. BAUER PEREIRA, R. P. HERMANN, M. SARAHA, E. PIPPEL, AND R. BRYDSON. **Microstructure analysis and thermoelectric properties of Ag(1-x)Pb18Sb(1+y)Te20.** *J. of Solid State Chem.*, **193**:58–63, 2012. 64
- [38] F. REN, B. D. HALL, E. D. CASE, E. J. TIMM, R. M. TREJO, R. A. MEISNER, AND E. LARA-CURZIO. **Temperature-dependent thermal expansion of cast and hot-pressed LAST (Pb-Sb-Ag-Te) thermoelectric materials.** *Philos. Mag.*, **89**:1439, 2009. 66
- [39] B. HOUSTON, R. E. STRAKNA, AND H. S. BELSON. **Elastic constants, thermal expansion, and Debye temperature of lead telluride.** *J. of Appl. Phys.*, **39**:3913–3916, 1968. 66
- [40] J. O. BARNES, J. A. RAYNE, AND R. W. URE JR. **Lattice expansion of Bi2Te3 from 4.2 to 600 K.** *Phys. Lett. A*, **46**:317–418, 1974. 66
- [41] T. EGAMI AND S. J. L. BILLINGE. *Underneath the Bragg Peaks: Structural Analysis of Complex Materials.* Pergamon Press, Oxford, England, 2003. 67
- [42] H. LIN, E. S. BOZIN, S. J. L. BILLINGE, E. QUAREZ, AND M. G. KANATZIDIS. **Nanoscale clusters in the high performance thermoelectric AgPbmSbTem+2.** *Phys. Rev. B*, **72**:174113, 2005. 67, 78

REFERENCES

- [43] R.P. HERMANN, F. GRANDJEAN, AND G. J. LONG. **Einstein oscillators that impede thermal transport.** *Am. J. of Phys.*, **73**:110–118, 2005. 70
- [44] V. G. KOHN AND A. I. CHUMAKOV. **DOS: Evaluation of phonon density of states from nuclear resonant inelastic absorption.** *Hyp. Int.*, **125**:205–221, 2000. 70
- [45] R. RÜFFER AND A. I. CHUMAKOV. **Nuclear inelastic scattering.** *Hyp. Inter.*, **128**:255–272, 2000. 71, 76
- [46] BAUER PEREIRA P, SERGUEEV I, J. DADDA, E. MÜLLER, AND R. P. HERMANN. **Lattice dynamics in AgSbTe₂.** In preparation. xvi, 74, 75, 77
- [47] P. BAUER PEREIRA, R. P. HERMANN, I. SERGUEEV, S. GORSSE, J. DADDA, AND E. MÜLLER. **Lattice dynamics and structure of GeTe, SnTe and PbTe.** Submitted to *Phys. Stat. Sol. B* in Sep. 2012. xvi, 74, 75, 77
- [48] A. KOSUGA, M. UNO, K. KUROSAKI, AND S. YAMANAKA. **Thermoelectric properties of Ag(1-x)Pb₁₈SbTe₂₀ (x = 0, 0.1, 0.3).** *J. of Alloys and Compds*, **387**:52–55, 2005. 76, 77
- [49] H. LEDBETTER, A. LAWSON, AND A. MIGLIORI. **Alpha-plutonium's Grüneisen parameter.** *J. Phys.: Condens. Matter.*, **22**:165401, 2010. 77
- [50] D. T. MORELLI, V. JOVOVIC, AND J. P. HEREMANS. **Intrinsically minimal thermal conductivity in cubic I-V-VI₂ semiconductors.** *Phys. Rev. Lett.*, **101**:035901, 2008. 77

Chapter 5

Resonant Ultrasound Spectroscopy

5.1 Resonant Ultrasound Spectroscopy

The elastic constants (moduli) correlate the deformation or strain to the applied stress, and characterize the elastic properties of a material. Since they correspond to the second derivatives of the free energy with respect to strain, their values macroscopically reflect the mechanical response of the material with respect to deformation, or the curvature of the interatomic potential around the equilibrium position. Larger elastic constants correspond to a sharper curvature. Measurements of the elastic constants is very important in solid state physics and materials science, since they are linked to the lattice behavior, the phonon spectra, and the other thermodynamic properties such as the Debye temperature and the Grüneisen parameter. Their characterization is also important for many engineering materials since a material's design and application will depend on its reliability and on its mechanical properties. Elastic properties can be determined by means of static techniques that measure a finite displacement as a linear response to an applied force. By ultrasonic techniques, one can measure either the time needed for an acoustic wave to travel through a medium, as in the pulse-echo (1) method, or the resonance vibration frequency spectrum of a solid body, as in the case of Resonant Ultrasound Spectroscopy (RUS) (2, 3). The choice of the appropriate technique depends on different factors such as the material, composition, sample quality and size, desired accuracy and, of course, availability of the apparatus and expertise. For example, homogeneous and anisotropic materials are commonly probed by the pulse-echo technique. One of the disadvantages of this method is the necessity of measuring the elastic constants along all the main crystallographic directions which can be time consuming and an inconvenience for low symmetry crystals. Another difficulty is that good acoustic coupling or even bonding between the sample and the transducer is required. However, when the temperature is increased, the stability of the coupling between the sample and transducer tends to decrease, which can endanger the quality of the investigation. The RUS technique, on the other hand, enables the direct determination of the elastic constants of a material in a unique measurement with high precision, as a frequency measurement can be as precise as several parts per million. RUS is also a good technique for measuring the material's mechanical properties at high temperature. Its principle is based on the fact that a body resonates when an external vibrational excitation matches one of its natural frequencies of vibration. The elastic constants can be inferred if the vibrational spectra, the mass and dimensions and estimated values for the elastic constants of a sample are known. The basic

5.1 Resonant Ultrasound Spectroscopy

steps for a successful RUS measurement at room or high temperature are the following: sample preparation, sample mounting, data acquisition and signal processing, followed by frequency extraction.

The sample for a RUS measurement should be properly cut and polished in order to obtain a geometrically perfect shape with parallel faces, normally a rectangular parallelepiped. Errors in parallelism error and perpendicularity of at most few parts in 10^3 are acceptable (4).

For isotropic materials, as the ones that we are working with, no orientation is needed during the preparation process. The cut is performed with a low-speed diamond saw or wire saw. After the cutting procedure, the sample is mounted in a sample holder, with the help of cold wax. The wax also protects the sample from mechanical and thermal stresses and can be easily removed with acetone. The polishing steps demand more attention and care, in order to achieve perfectly parallel faces. A polishing machine with SiC abrasive discs in different grid sizes is used. The process starts with two opposing faces. One face is glued with cold wax to the stainless steel mounting disk, so that the opposite face can be polished. The procedure is repeated after flipping the sample. Next, to keep the parallelism, the use of two rectangular blocks is needed to mount the sample so faces that are 90° with respect to the first two polished will be obtained. After the six faces are done, the sample is cleaned with acetone (and/or ethanol) and checked microscopically to assure that no voids or surface defects (as cracks) are present. Finally, the mass and dimensions are measured before the sample is mounted for RUS measurements. A schematic apparatus for RUS experiments is illustrated in Fig. 5.1. For the experiment, the specimen is placed between two piezoelectric transducers (for conventional room temperature and direct-contact set ups) or between the buffer-rods (for the high temperature setup). Basically, the mounting can be done in two ways, face-mounting and corner-mounting. In theory, all the vibrational modes can be detected by corner-mounting the sample since in this configuration there is a minimum contact between sample and transducers and the best possible approximation of fully free vibration body is achieved. However, depending on the sample size, such arrangement is very difficult to be maintained, and face-mounting configuration is preferred. With the sample placed in the equipment, a drive frequency is emitted from one transducer, and the sample response is detected by the second transducer; when the incoming wave matches a natural frequency of the sample, a resonance peak can be seen at this frequency. The detected resonance signals in frequency domain contain both magnitude and phase information. The resonance

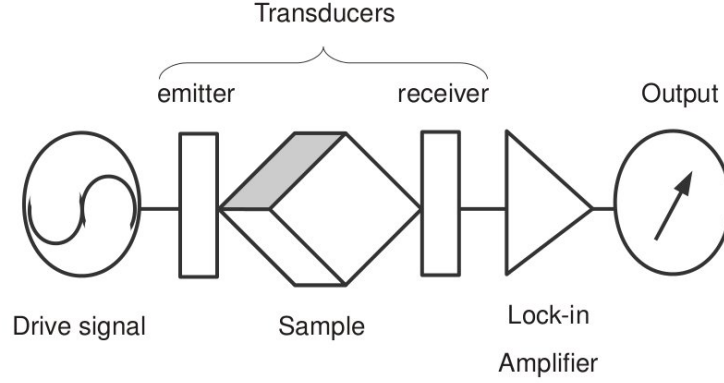


Figure 5.1: Classical experimental arrangement of the RUS method.

modes are computed from the in-phase component. With high signal-to-noise ratio and well-separated modes, the fitting code (written by Dr. J. Gladden, University of Mississippi) can automatically extract the center frequency and quality factor ($Q = \frac{\Delta f}{f_o}$, and Δf is the frequency width of half magnitude and f_o is the measured frequency) for each single mode. This procedure is straightforward when peaks are well separated from each other. The observed experimental spectra is compared to the computed one, and the elastic constants are extracted.

From probing a polycrystalline isotropic sample by RUS two independent elastic constants can be directly obtained, c_{11} and c_{44} . The shear modulus G is equal to c_{44} . With c_{11} and c_{44} , the Young modulus, $E = (3c_{44}c_{11} - 4c_{44}^2)/(c_{11} - c_{44})$, Poisson ratio, $\nu = (E/2G) - 1$, and the bulk modulus, $B = E/(3(1 - 2\nu))$, are calculated (5). Additionally, the isotropic average of the longitudinal and the transversal velocity of sound can be obtained by $v_L^2 = c_{11}/\rho$ and $v_T^2 = c_{44}/\rho$, respectively, where ρ is the density of the material. The mean velocity of sound can be calculated using $3/v_s^3 = (2/v_T^3 + 1/v_L^3)$, in the Debye approximation.

5.2 Theoretical background

The resonance frequencies (normal modes) of a solid body can be computed if its dimensions, density and elastic moduli are known; this is called the *direct problem*. The *inverse problem* - that is, the extraction of all elastic constants of a material from a measured set of resonance

frequencies is of greater interest. As the resonances of a material are easily measured, for example, by RUS method, this is a strong technique for “solving” the *inverse problem*.

5.2.1 Linear Elasticity

A short overview of the linear elasticity theory (6, 7) is presented next, not exhaustively but in order to present the basic elements to understand the theoretical basics behind RUS characterization. The linear elasticity theory is interested in how solid objects deform and become internally stressed due to prescribed loading conditions. The basic assumptions of linear elasticity include small deformations - or strains below the yield point - and a linear relationships between strain (displacement between particles due an applied stress) and stress (force per unit area); that means that the strain in the solid depends only on the stress applied to it, regardless of other parameters as rate of loading or history of loading, for example. In the elastic regime, after the removal of load the deformations is completely recoverable and the solid body returns to its initial state. When the yield point is reached, the solid might deform plastically and fail (i.e., ductile metals) or fracture (i.e., ceramics). This theory can be applied to most engineering materials if the applied loads are small enough. Assuming a homogeneous solid body without load where any point in the body is defined by its radius vector \mathbf{r} (with components $x_1 = x$, $x_2 = y$, $x_3 = z$) in Cartesian coordinates. Considering one particular point P , r (with components x_i). If a external force is applied, the point P is displaced to a new coordinate r' (with components x'_i), described by the displacement vector $u = r' - r$

$$u_i = x'_i - x_i. \tag{5.1}$$

Due to the relation between the displacement vector and the initial position, which is a function of x itself, a small deformation of the solid can be written as a sum of the partial derivatives with respect to each direction

$$du_i = u_{i1}dx_1 + u_{i2}dx_2 + u_{i3}dx_3 = u_{ij}dx_j. \tag{5.2}$$

Applying the Einstein notation, where indices of same index are summed over, and separating Eq. 5.2 into a symmetrical and antisymmetrical components yields

$$du_i = \frac{1}{2}(u_{ij} + u_{ji}) + \frac{1}{2}(u_{ij} - u_{ji}). \tag{5.3}$$

The strain tensor, which describes the deformation produced by applied forces, is obtained from Eq. 5.3, after neglecting the second term corresponding to full body rotations (independent of any elastic deformation):

$$\epsilon_{ij} = \frac{1}{2}(u_{ij} + u_{ji}). \quad (5.4)$$

Due to the strain tensor symmetry, only six components are independent:

$$\epsilon_{ij} = \epsilon_{ji}. \quad (5.5)$$

When a body is subjected to external forces, the displacement of the body's constituting particles produces internally distributed forces. The distortions undergone by a solid are caused by the sum of the internal forces acting in the body, namely, the stress applied in a certain area. In order to evaluate the magnitude of the forces acting at any point, we can assume a small part of the body divided into two by an imaginary surface. Normal strains (axial), and/or parallel strains (shear) to the surface can be acting on the differential surface area dS_j . With this in mind, the components of the force, dt_i , acting in a surface dS_j are described as

$$dt_i = \sigma_{ij}dS_j, \quad (5.6)$$

where σ_{ij} is the stress tensor with units of force per unit area. The subscript notation have the following meaning: the first subscript correspond to the direction of the surface normal upon which the stress acts, whereas the second subscript indicates the direction of the stress term.

Since each point in the body is under static equilibrium (no net force in the absence of any body forces, no translations, no rotations), the stress tensor is symmetric:

$$\sigma_{ij} = \sigma_{ji}. \quad (5.7)$$

These components can be organized into the matrix:

$$\sigma_{ij} = \begin{bmatrix} \sigma_{xx} & \sigma_{xy} & \sigma_{xz} \\ \sigma_{yx} & \sigma_{yy} & \sigma_{yz} \\ \sigma_{zx} & \sigma_{zy} & \sigma_{zz} \end{bmatrix} \quad (5.8)$$

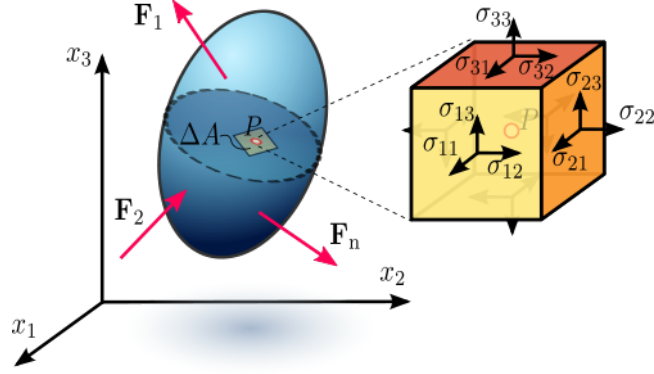


Figure 5.2: Stress tensor in an infinitesimal material element around a point P.

where shear stresses across the diagonal are symmetric ($\sigma_{xy} = \sigma_{yx}$, $\sigma_{yz} = \sigma_{zy}$, $\sigma_{zx} = \sigma_{xz}$), the moment is zero and only six independent components are independent.

The stress tensor and the strain tensor (both second rank tensors) are related through the elasticity (elastic modulus) tensor C_{ijkl} by Hooke's law

$$\sigma_{ij} = C_{ijkl}\epsilon_{kl}. \quad (5.9)$$

where σ_{ij} is the stress tensor, C_{ijkl} is the elasticity (or stiffness) tensor, and ϵ_{kl} is the strain tensor. The fourth-order tensor C_{ijkl} has $i, j, k,$ and $l=1, 2, 3$ and generalises the concept of the spring constant of a simple spring to three-dimensional elastic media.

In general a tensor of rank 4 in three dimensions has 81 components (6). The symmetry relations (see Eq. 2.5 and 2.7) reduce the number of independent components of the elasticity tensor to the number of independent elements of a symmetric 6×6 matrix C_{ij} , which means that the elasticity tensor has at most 21 independent elements in three dimensions. When the crystallographic symmetry is also taken into account, the number of elastic constants is further reduced depending on symmetry of the system, i.e., from triclinic system (minimum symmetry) with 21 elastic constants to cubic with 3, and finally, an isotropic system with only 2 independent elastic constants. The Voigt notation is used for simplifying the tensor representation by grouping pairs of indices in a single new index ($11 \rightarrow 1; 22 \rightarrow 2; 33 \rightarrow 3; 12 = 21 \rightarrow 6; 23 = 32 \rightarrow 4; 13 = 31 \rightarrow 5$). Some examples are

5.2 Theoretical background

presented next, in Table 5.1. Notice that for isotropic materials, only 2 independent elastic constants are required to fully describe its elastic properties. Young's modulus, E , and Poisson's ratio, ν , are common properties used to characterize an elastic body. Other measurements such as bulk modulus, B , and/or shear modulus, G , can however be preferred. For isotropic materials, G and B are obtained from E and ν by a set of equations, as $G = \frac{E}{2(1+\nu)}$ and $E = 3B(1 - 2\nu)$.

Table 5.1: Different crystal symmetries and their independent elastic constants.

Crystal symmetry	Number of C_{ij}	Elastic constants
Triclinic	21	All possible combinations
Monoclinic	13	$C_{11}; C_{12}; C_{13}; C_{16}; C_{22}; C_{23}; C_{26};$ $C_{33}; C_{36}; C_{44}; C_{45}; C_{55}; C_{66}$
Orthorhombic	9	$C_{11}; C_{12}; C_{13}; C_{22}; C_{23};$ $C_{33}; C_{44}; C_{55}; C_{66}$
Trigonal	7	$C_{11}; C_{12}; C_{13}; C_{14}; C_{15}; C_{33}; C_{44}$
Tetragonal	6	$C_{11}; C_{12}; C_{13}; C_{33}; C_{44}; C_{66}$
Hexagonal	5	$C_{11}; C_{12}; C_{14}; C_{33}; C_{44}$
Cubic	3	$C_{11}; C_{12}; C_{44}$
Isotropic	2	$C_{11}; C_{44}$

The numerical approach used to calculate the natural frequency modes of a solid and to solve the inverse problem is based on Rayleigh-Ritz method (8), where the equilibrium state of a system is obtained by minimizing the Lagrangian

$$L = \int_V (T - U) dV, \quad (5.10)$$

where T is the kinetic energy and U the potential energy of the body with volume V . For an elastic body of arbitrary shape, the potential and kinetic energies are given by

$$U = \frac{1}{2} c_{ijkl} \epsilon_{ij} \epsilon_{kl} = \frac{1}{2} c_{ijkl} \frac{\partial u_i}{\partial x_j} \frac{\partial u_k}{\partial x_l} = \frac{1}{2} c_{ijkl} u_{ij} u_{kl} \quad (5.11)$$

$$T = \frac{1}{2} \rho \omega^2 u_i u_j, \quad (5.12)$$

respectively, where ρ is the material's density, ω is the angular frequency of normal modes and c_{ijkl} the components of the elastic modulus tensor. The displacement is approximated by an expansion into a complete set of basis functions

$$u_i \approx a_{i\alpha} \psi_\alpha, \quad (5.13)$$

where we choose as our basis functions powers of Cartesian coordination, for the evaluation of the presented integrals for a large number of shapes:

$$\psi_\alpha = x^l y^m z^n, \quad (5.14)$$

where $\alpha = (l, m, n)$ is the function label, that results in well-conditioned matrices and allows the analytic solution of the integrals involved. The Lagrangian is re-written as

$$L \approx \frac{1}{2} (a_{i\alpha} a_{i'\alpha'} \omega^2) \int_V \delta_{ii'} \psi_\alpha \psi_{\alpha'} dV - \frac{1}{2} a_{i\alpha} a_{i'\alpha'} \int_V c_{ijj'j'} \psi_{\alpha j} \psi_{\alpha' j'} dV \quad (5.15)$$

Reformulating Eq 5.13 in a compact matrix format

$$L = \frac{1}{2} ((\rho\omega^2) a^T \mathbf{E} a - a^T \mathbf{\Gamma} a) \quad (5.16)$$

with the matrices \mathbf{E} and $\mathbf{\Gamma}$ defined as

$$E_{\alpha i \alpha' i'} \rho = \delta_{ii'} \int_V \psi_\alpha \psi_{\alpha'} dV \quad (5.17)$$

$$\Gamma_{\alpha i \alpha' i'} = c_{ijj'j'} \int_V \psi_{\alpha j} \psi_{\alpha' j'} dV \quad (5.18)$$

yields a generalized eigenvalue equation with eigenvalues ω^2 and eigenvector \mathbf{a} (expansion coefficients):

$$\mathbf{\Gamma} \mathbf{a} = (\rho\omega^2) \mathbf{E} \mathbf{a}. \quad (5.19)$$

This procedure reduces the inverse problem to the evaluation of Eq. 5.16 and 5.17.

5.3 High Temperature RUS

Since the publication of Migliori *et al.* in 1993 (3), when a clean computational method for acquiring data and calculating the resonance frequencies of a regular shaped sample was first presented, the RUS technique has attracted more attention in the study of novel or well known materials. The development of personal computers had also a great influence in the spread of the method as an efficient and accurate possibility for characterizing the elastic properties of a material at low and room temperatures. The elastic properties of materials however depend on temperature. In order to understand a materials response to thermal and mechanical stresses, the dependence of the elastic constants with temperature should be determined. At higher temperatures, normally it is expected that the Young modulus E and shear modulus G are, both, lower than values at low or room temperatures (9). For materials intended for high temperature use, such characterization is essential to assure that the device will not fail and will keep its properties for the whole range of working temperatures. Applications of RUS in the high temperature regime have been limited, partly due to the difficulties caused by the weak resonance signals at high temperatures.

During the first years of development of RUS, the technique was mainly applied to minerals of geophysical interest. The study of the elastic properties of the Earth's mantle in temperatures above the Debye temperature of constituent minerals (700 to 1200 K) was first suggested by Birch in 1952 (10). After this publications, different setups were proposed in the next years by Sumino *et al.* (11, 12) with operating temperatures up to 1300 K. A practical buffer-rod design was built in 1989, by Anderson (13) for the characterization of elastic constants of mantle-related materials at temperatures up to 1800 K. The main design difference between the reported setups is how the contact between sample and transducers is established. For the *direct-contact* setup, as the name implies, the sample is directly placed between the two transducers. The conjunct sample plus transducers is placed inside a heated chamber and exposed both to the same temperature range during the measurements. Therefore, the maximum operating temperature for the direct-contact set up will be determined by appropriate selection of the piezoelectric transducer. For higher temperature measurements, a buffer rod setup is required in order to separate the transducer from the heating zone. In this case, the sample is held between two long thin alumina buffer rods, with piezoelectric transducers attached to their opposite ends. To avoid oxidation of the sample during measurement, the whole system is placed in a sealed environment with a gas flushing system or with connection

to a vacuum pump. The transmission of the acoustical signal occurs through the buffer rod material, which reduces the signal strength. Also, it is important in this case to be aware of the natural buffer rods resonances and the possibility that they might overlap with the materials resonance peaks.

5.3.1 Design and Fabrication

This section describes our design and fabrication of the buffer-rods high-temperature RUS setup, during the period of this thesis, at the Forschungszentrum Jülich. The design and fabrication of the buffer-rod high-temperature RUS measurement system involved different steps: identification and purchase of the required materials, fabrication of components, construction of the measurement system and support cage, and finally, testing the system at room and at high temperatures. Several components are crucial to the high-temperature RUS setup, to guarantee high quality signals and to withstand the high temperature zone inside the furnace, *i.e.*, (i) two buffer rods made of low acoustic attenuation and low thermal conductivity material, (ii) piezoelectric materials with high Curie and operating temperatures for transducers; (iii) coaxial cables that offer stable and excellent high temperature performance; and (iv) high temperature adhesives for settling the measuring cage. Additional components for the system include a turbo vacuum pump to prevent the sample and transducer from being oxidized at high temperature, a quartz tube in which the set up is placed and sealed, and a vertical furnace for heating. It is also important to notice here that for achieving optimized RUS results, the sample preparation step is crucial. Therefore, a wire saw was also purchased. Equipment and materials for sample manipulation includes: vacuum tweezers, lapping and polishing accessories, SiC abrasive film discs and a stereoscope. The alumina buffer rods cage drawing from our high temperature RUS is presented in Fig. 5.3.

The main part of the system consist of the measurement cage, where the buffer-rods/transducer assembly is placed. To provide structural support, a cage of six alumina discs (60 mm in diameter and 7 mm thick) and three long alumina rods (3 mm in diameter and 594 mm long) has been constructed. The cage components are made from alumina due its low acoustic attenuation, thermal stability and low cost. The first step to set the measurement cage is to assure that all components are clean and free of dust and grease. The alumina rods are placed in drilled holes separated 120° from each other in the discs. The transducers probes are placed through holes of 2.1 mm diameter at the center of each disc. An additional set of holes in the three top discs is necessary for the thermocouple used to verify the temperature

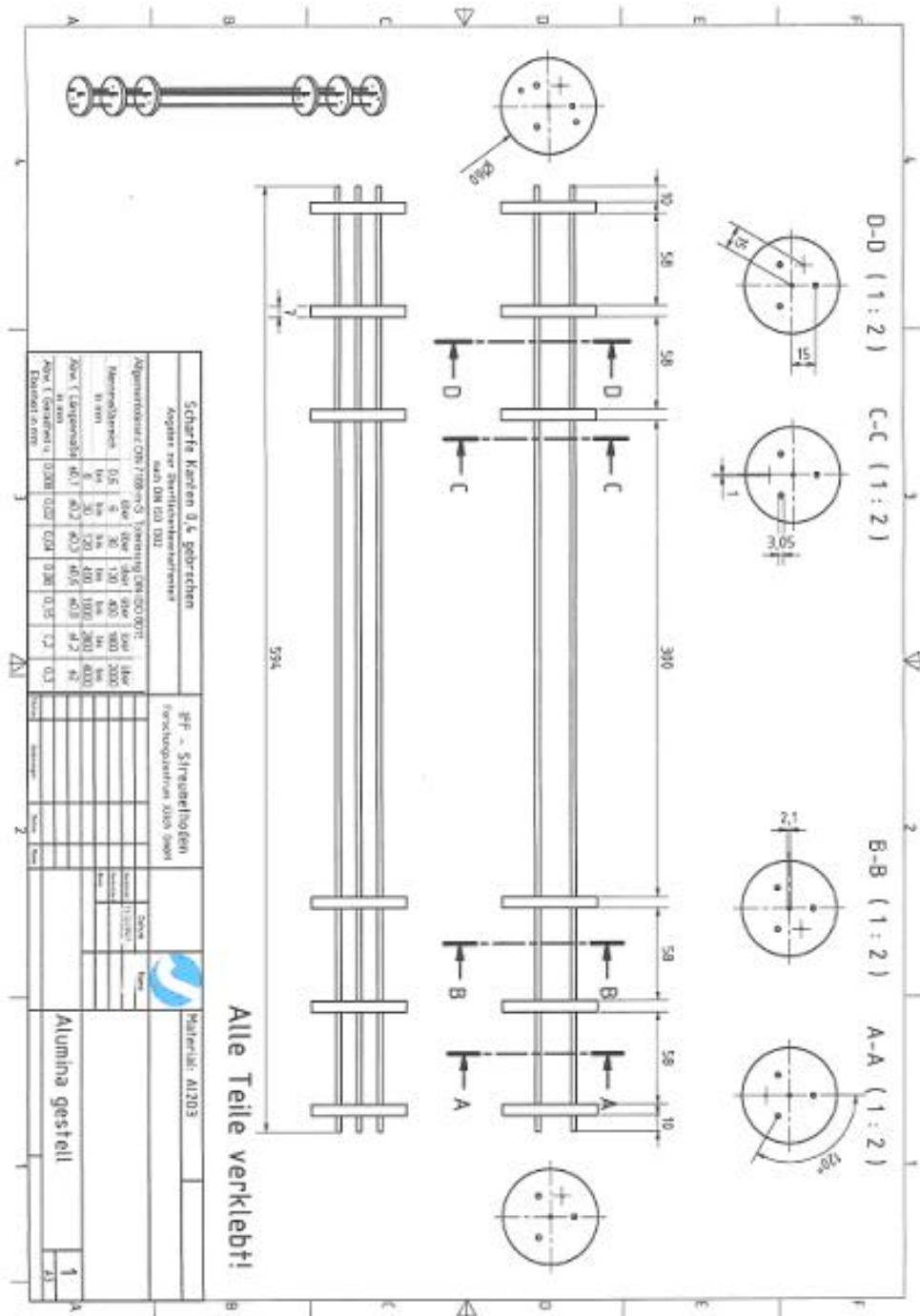


Figure 5.3: Technical drawing of the support cage of the HT-RUS setup. The figure shows the components (discs and long alumina rods) used and their dimensions.

close to the sample. In the assembly, the three bottom discs and the three top discs are separated by 58 mm; the hot zone (distance between disc 3 and 4) is 300 mm long. The alumina discs and long rods are glued together with the high temperature ceramic adhesive Ceramabond[®]503. The adhesive is diluted in 20% water by weight and applied with a clean brush. During the adhesive application, the loose components are kept in the correct position by wood blocks placed between the discs. The drying process consists of letting the cement adhesive one hour in ambient temperature, followed by another four to five hours drying with the heat gun. After the drying, a quick check if the components are properly glued is necessary. If any part is still loose, the adhesive application and drying process are repeated. Six discs were used in total in our setup to guarantee that the temperature in the cold zone is always lower than the 473 K. During the measurements, the complete cage plus buffer-rods/transducers conjunct are placed inside the quartz tube which goes in the vertical furnace. Care must be taken not to bend the cage when placing it in the quartz tube or while lifting it. After repeated heating/cooling cycles, the components or the adhesive might lose some of their mechanical stability and the whole assembly must be replaced. With the support cage ready, the buffer-rods/transducer and connections are made next. The choice of the transducer to be used is crucial to assure good signal quality during the probed range of temperature, especially at high temperature. Ideally, the highest possible Curie temperature is desired. Based on this, only a few candidates were identified, which included lead zirconate titanate $\text{Pb}[\text{Zr}_x\text{Ti}_{1-x}]\text{O}_3$ (PZT), bismuth titanate $\text{Bi}_4\text{Ti}_3\text{O}_{12}$, gallium orthophosphate GaPO_4 and lithium niobate LiNbO_3 with Curie temperatures of 623 K, 930 K, 1243 K and 1473 K respectively. Despite exhibiting the lowest Curie temperature among the pre-selected materials, PZT was the final material of choice due its commercial availability and exceptional high-signal properties at an affordable price. To confirm the viability of the use of PZT, a temperature scan of the furnace regions was done and showed that while the temperature at the heat zone was kept at 1273 K for several hours, the temperature at the transducer's position (cold zone) never raised above 473 K. PZT transducers were purchased from Boston Piezo-Electronics. Single crystals of 3 mm diameter coated with chrome/gold in the back side and in a "coaxial" fashion in one face were chosen for the excitation and detection function. The coaxial layout means that, in one face, three distinct areas are identification (1) a non-coated ring which is present between the (2) central point (0.8 mm) and the (3) outside layer. This layout is necessary in order to make the electrical contact between the transducer and driving cables cables, with the conductor part (central point)

5.3 High Temperature RUS

and the grounding (outer layer) in just one surface. The electrical connection between driving system and piezoelectric element was made using a regular coaxial cable with stranded copper and braided gold-plated copper as the inner and outer conductor, respectively. The inner conductor is welded directly to the central point of the transducer, whereas the sheath is connected to the outer layer. A simple electrical resistance measurement between the inner and outer connection is performed to guarantee the absence of a short circuit remaining from the welding process. The transducer probe is ready when the contact between coaxial cable and transducer is established. Then, the transducer is glued to the alumina buffer rod with instantaneous adhesive. The instantaneous adhesive allows a very quick cure process, good adherence and it is easily solved in acetone. A pair of transducer probes were prepared as described for the high-temperature RUS apparatus. The environment of the experiment is confined to the inner part of a quartz tube of 70 mm in diameter and 700 mm long. The top part is specially designed with three possible out connections, while the bottom has only one connection. For a high temperature measurement, the assembly of two transducer probes and the support cage are carefully slid in a quartz tube, which is placed in a vertical tube furnace (Carbolite Model VST 12/200). The quartz tube is connected to a turbo vacuum pump (Pfeiffer Vacuum Model HiCube[®] 80 Eco), a pressure gauge (Pfeiffer Vacuum Single Gauge DCU 002) and a temperature control unit. The turbo pump is necessary in order to maintain the oxygen presence to its possible minimum and consequently, to protect the sample from any oxidation process during heating and to minimize thermal conductivity by gas convection. Pressures in the order of 10^{-4} mbar are kept during the whole measurement; the pressure is continuously monitored by the pressure control unit. Fig. 5.4 shows a picture of the actual high-temperature RUS measurement system. After the construction of the buffer-rods high-temperature RUS system, a test has been performed to confirm the functionality of the system.

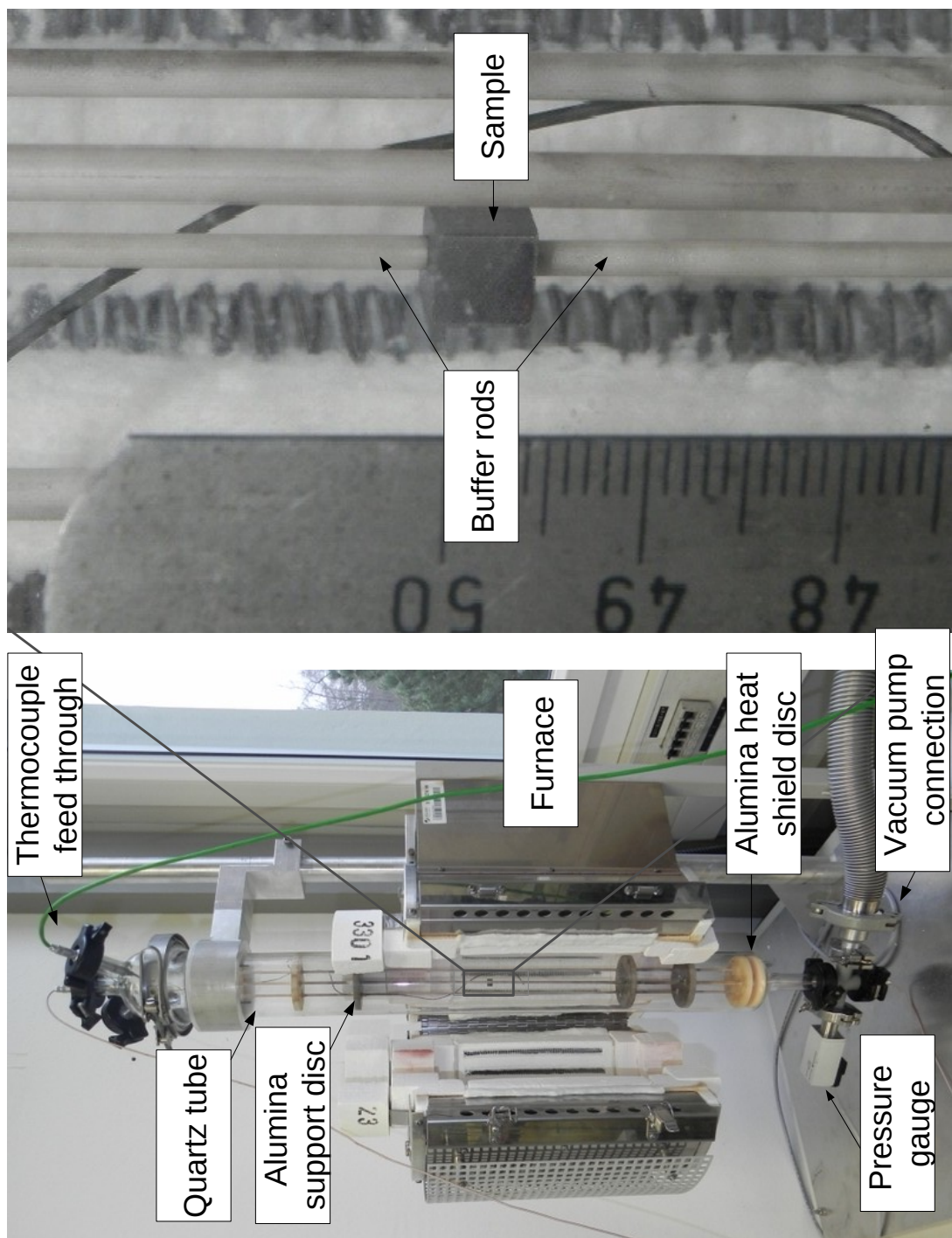


Figure 5.4: Current HT-RUS set up. The figure shows cage/transducer probes inside the quartz tube in the tube furnace, before a measurement.

5.3.2 Testing of the Buffer-rod Transducer System

The functionality of the newly constructed buffer-rods high temperature RUS system was first tested at room temperature. The interest for such a test was (i) to check the electric connection with the PZT transducer probes, (ii) to check the signal-to-noise ratio and resonance characteristics of the whole system (two transducers, two buffer-rods, thermocouple wire, cage, etc) at room temperature, and (iii) to test the structural stability of the system as sample is mounted. Further tests with increasing temperature were also performed and in order to check the same properties (specially the signal-to-noise ratio) and to test the thermal stability of the system after repeated heating/cooling cycles. The room temperature test was conducted with the RUS cell outside the furnace so that there is free access to the sample. A PbTe sample with dimensions 2.228 mm x 2.366 mm x 1.634 mm was prepared, as previously described. Before the test measurement on the high temperature RUS setup, data on the same sample was acquired at our standard room temperature system; the measured resonance peaks and the extracted elastic constants will be used for future comparison of both systems. Several scans, with the sample face-mounted and corner-mounted were performed and for all measurements the sample was swept in the same frequency range. After the preliminary room temperature test, the RUS set up was moved to the furnace for high-temperature evaluation. The test started at room temperature until 573 K, in steps of 50 K.

Frequencies scans obtained with RT-RUS and HT-RUS set ups, at room temperature, are presented in the Fig. 5.5. The buffer-rod data has been amplified by a factor of 10 to aid the comparison. The signal-to-noise ratio is better for the conventional system than that for the buffer-rod system, but the resonance peaks are easily distinguishable in both cases. The agreement between the peak position obtained from the two set ups is good, with a maximum mismatch shift of 0.6% in the high frequency region. The background noise depends on the sensitivity of the lock-in amplifier. Lower noise corresponds to higher sensitivity, but it can cause overload of the amplifier for stronger peaks. In Fig. 5.5, some peaks do not correspond to resonance frequencies of the sample, but to peaks generated by the lock-in amplifier during frequency switching. Those marks occur in characteristic frequencies, and normally, do not interfere in the results. For complete elimination of these marks, a longer sweep (smaller frequency step) can be performed.

The smaller shift from the HT-RUS, and higher frequency precision, is explained by lower loading effect caused by the light weighted buffer rod (3.83 g) in comparison with the load

applied in the conventional RT setup (10 g). For a properly prepared sample, the overall RMS (root-mean-square) error comparing the calculated and experimentally obtained frequencies should stay the range of 0.1-0.3% to be considered good. Table 5.2 shows the measured and calculated resonance frequencies, at room temperature, probed by the RT-RUS and HT-RUS. The resulting elastic properties of PbTe extracted from the obtained frequencies scans probed by the two different set ups are presented in Table 5.3. Only small deviation between measured and calculated data (rms = 0.22%) that was obtained by HT-RUS is noteworthy. Experimental and literature values (14) are in good agreement.

Table 5.2: Measured (f^{meas}) and calculated (f^{calc}) resonance frequencies for a PbTe sample, at room temperature, using the conventional room temperature (RT-RUS) and HT-RUS setups. A final RMS error of 0.44 and 0.22%, respectively, were obtained for these sets of data.

RT-RUS			
Mode	f^{meas} (kHz)	f^{calc} (kHz)	Difference (%)
1	159.405	157.620	1.13
2	178.258	179.203	-0.53
3	265.664	265.344	0.12
4	292.376	292.150	0.07
5	300.286	300.196	0.03
6	314.621	309.597	1.66
7	348.087	347.853	0.06
8	369.464	369.986	-0.14

HT-RUS			
Mode	f^{meas} (kHz)	f^{calc} (kHz)	Difference (%)
1	160.395	164.391	-2.52
2	179.013	176.157	1.50
3	266.121	267.546	-0.53
4	292.916	279.257	0.46
5	301.085	300.726	0.11
6	315.396	315.311	0.02
7	349.038	348.892	0.04
8	370.600	370.470	0.03
9	406.944	408.581	0.40

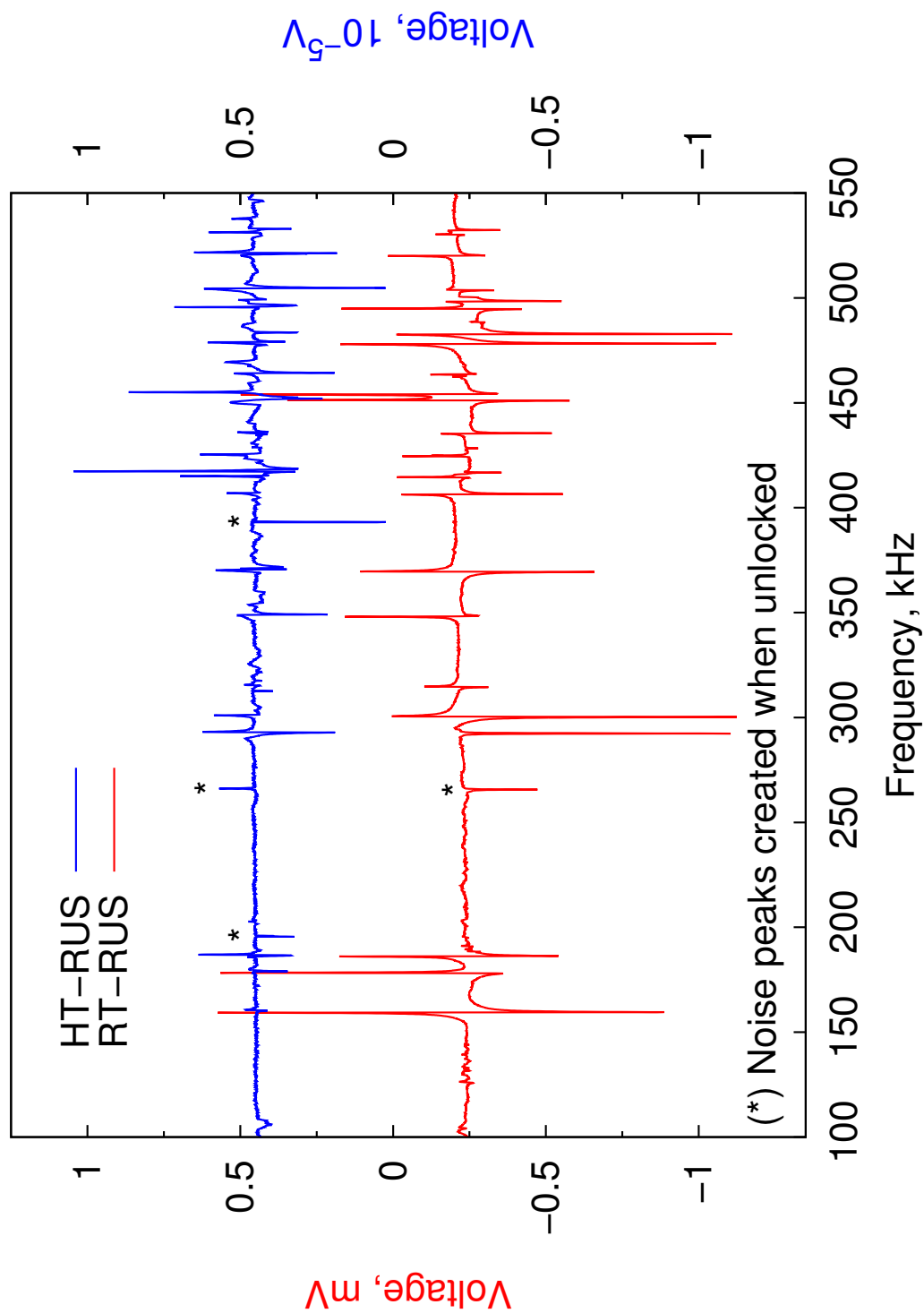


Figure 5.5: The figure compares frequency scans obtained with the conventional room temperature setup (red line) and the newly constructed high-temperature RUS (blue line). The extra peaks, marked with (*), correspond to peaks generated by the lock-in amplifier when the amplifier is momentarily unlocked during frequency switching.

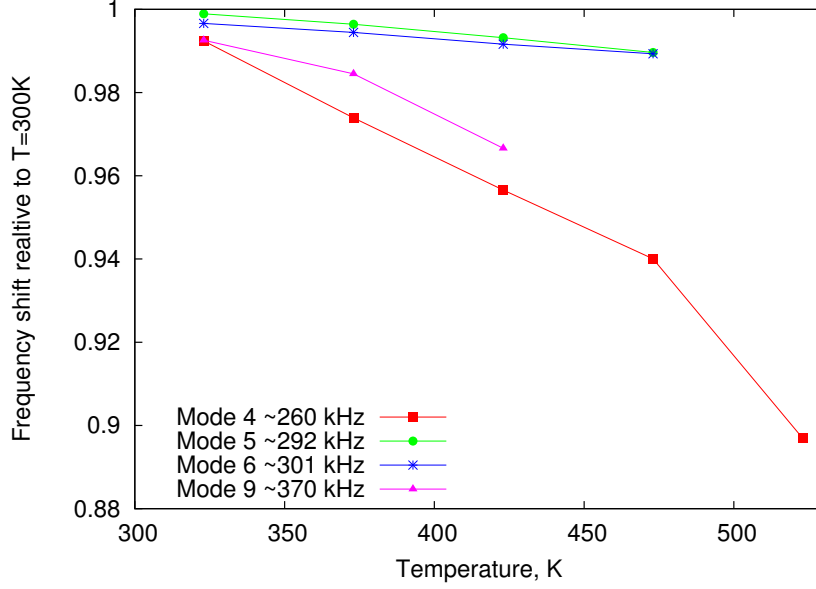


Figure 5.6: Modes tracking of PbTe from room temperature to 523 K. Four modes were tracked throughout the temperature range from room to 523 K. The elastic behavior of PbTe can be inferred based on this method.

Table 5.3: Comparison between the elastic properties of a PbTe sample, at room temperature, probed with the conventional and HT-RUS setups.

Source	Sample	Young's Modulus, GPa	Shear's Modulus, GPa	Poisson's ratio ν	rms RUS fit, %
RT-RUS setup	PbTe	54.8	21.9	0.25	0.44
HT-RUS setup	PbTe	57.3	22.4	0.28	0.22
Literature(14)	PbTe	57.5	22.3	0.29	0.62

Next, the first experiment with PbTe, at temperatures above room temperature, was performed. After the sample is mounted between the buffer rods, the whole measuring cage is placed inside the tube furnace. During this procedure, the sample might be shifted or even fall out of the set up. Before closing and sealing the quartz tube, a quick scan is performed to ensure the correct contact between sample and measuring probes. The furnace was manually controlled and set up to heat the system up to 523 K, in 5 K steps. For this range of temperature, a proper fit of the resonances could not be performed. The soft character of PbTe, and structural instability above 550 K, was reported by Bozin *et. al.* (15). This

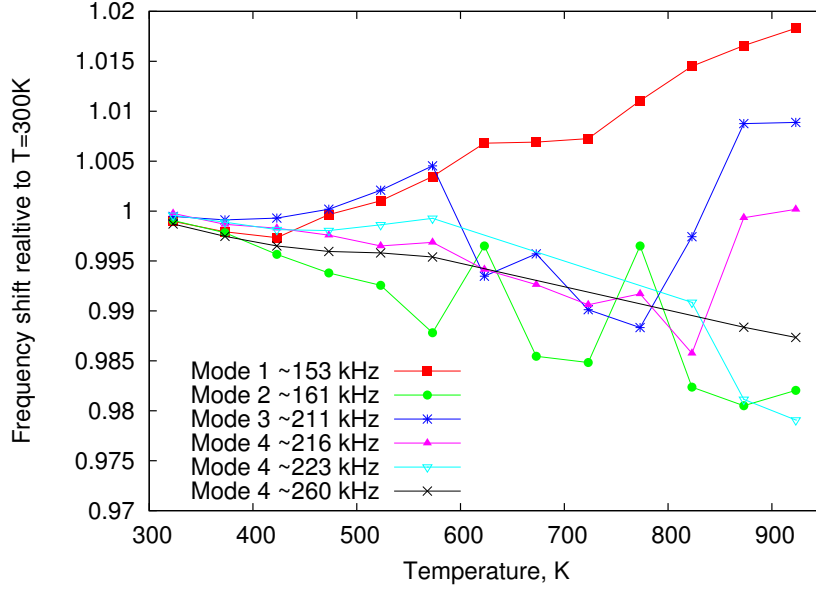


Figure 5.7: Nb modes tracking: Six modes were tracked throughout the temperature range from room to 973 K.

particular characteristic makes the RUS measurement very difficult to perform on PbTe, due to lossy nature of the sample and due the poor signal-to-noise ratio obtained with increasing temperature. Above 373 K, the resonant signal is weak and therefore, the peaks are difficult to identify. However, the general behavior of the elastic properties can be inferred from the changes in the frequency within temperature, in the so called “*mode tracking*” method. In the case that the majority of sample peaks can not be obtained for computing the elastic moduli of a sample, the behavior of the identified peaks with temperature can be useful. Despite the low signal-to-noise ratio, four peaks have been tracked and are plotted on Fig. 5.6. We observe that, in general, with increasing temperature the frequencies are shifted to lower values, indicating a softening of the material with heating. We can see that, *i.e.*, mode 4 is strongly influenced by temperature, while mode 5 and 6 respond in a different matter to temperature.

The mode tracking method was also used for studying a Niobium sample (6.073mm x 5.953 mm x 5.840 mm, and density of 8.57g/cm³) from room temperature to 927 K, see Fig. 5.7. The simplicity and practicality of the method was used to evaluate the functionality of our system at high temperatures. The interest here was to observe the signal-to-noise ratio at high temperature and also to test the structural stability of the cage/transducer assembly

during and after the heating/cooling cycle. Niobium was chosen for being a dense material with high melting point, which can withstand the temperature regime imposed without losing its mechanical properties. We conclude that the system is functional until (at least) 927 K. The system withstands the temperature regime without compromising its mechanical and structural stability. However, for a successful RUS measurement, starting with the detection of resonance frequencies and concluding with extracting the elastic constants of a material, the sample quality is essential for successful measurements, including high parallelism of sample faces (in the case of a parallelepiped shape), high density, and absence of defects, such as voids and cracks.

References

- [1] M. F. MARKHAM. **Measurement of elastic constants by the ultrasonic pulse method.** *British Journal of Appl. Phys.*, **8**:56, 1957. 83
- [2] R. F. S. HEARMON. **The elastic constants of anisotropic materials.** *Rev. Mod. Phys.*, **18**:409–440, Jul 1946. 83
- [3] A. MIGLIORI, J. L. SARRAO, W. M. VISSCHER, T. M. BELL, M. LEI, Z. FISK, AND R. G. LEISURE. **Resonant ultrasound spectroscopic techniques for measurement of the elastic moduli of solids.** *Physica B*, **183**:1–24, 1993. 83, 91
- [4] A. MIGLIORI AND J. D. MAYNARD. **Implementation of a modern resonant ultrasound spectroscopy system for the measurement of the elastic moduli of small solid specimens.** *Rev. Sci. Instrum.*, **76**:121301, 2005. 84
- [5] L. ZHANG, G. ROGL, A. GRYSIV, S. PUCHEGGER, J. KOPPENSTEINER, F. SPIECKERMANN, H. KABELKA, M. REINECKER, P. ROGL, W. SCHRANZ, M. ZEHETBAUER, AND M.A. CARPENTER. **Mechanical properties of filled antimonide skutterudites.** *Mat. Sci. and Eng.: B*, **170**:26–31, 2010. 85
- [6] S. P. TIMOSHENKO AND J. N. GODIER. *Theory of Elasticity.* McGraw Hill Higher Education, 1970. 86, 88
- [7] A. MIGLIORI AND J. L. SARRAO. *Resonant Ultrasound Spectroscopy: Applications to Physics, Materials Measurements, and Nondestructive Evaluation.* Wiley-Interscience, 1 edition edition, 1997. 86
- [8] P. MORSE AND FESHBACH H. *Methods of Theoretical Physics.* McGraw Hill, New York, 1953. 89
- [9] J. B. WATCHMAN. *Mechanical properties of ceramics.* Willey Interscience, 1996. 91
- [10] F. BIRCH. **Elasticity and constitution of the Earth's interior.** *J. Geophys. Res.*, **57(2)**:227–286, 1952. 91
- [11] Y. SUMINO, O. NISHIZAWA, T. GOTO, I. OHNO, AND M. OZIMA. **Temperature variation of elastic constants of single-crystal forsterite between -190 and 400 C.** *J Phys Earth*, **25**:377–392, 1977. 91
- [12] Y. SUMINO, O. L. ANDERSON, AND I. SUZUKI. **Temperature coefficients of elastic constants of single crystal MgO between 80 and 1300 K.** *Phys. and Chem. of Minerals*, **9**:38–47, 1983. 91
- [13] O. L. ANDERSON AND T. GOTO. **Measurement of elastic constants of mantle-related minerals at temperatures up to 1800 K.** *Physics of the Earth and Planetary Interiors*, **55(3-4)**:241–253, 1989. 91
- [14] F. REN, E. D. CASE, J. R. SOOTSMAN, M. G. KANATZIDIS, H.KONG, C. UHER, E. L. CURZIOD, AND R. M. TREJO. **The high-temperature elastic moduli of polycrystalline PbTe measured by resonant ultrasound spectroscopy.** *Acta Mater.*, **56**:5954–5963, 2008. 98, 101
- [15] E. S. BOZIN, C. D. MALLIAKAS, P. SOUVATZIS, T. PROFFEN, N. A. SPALDIN, M. G. KANATZIDIS, AND S. J. L. BILLINGE. **Entropically stabilized local dipole formation in lead chalcogenides.** *Science*, **330**:1660–1663, 2010. 101

Chapter 6

Conclusions and Outlook

The lattice dynamics in complex chalcogenides LAST-18, AgSbTe₂ and the binaries PbTe, SnTe and GeTe were studied by X-ray diffraction, nuclear inelastic scattering (NIS) and macroscopic techniques including heat capacity, thermal expansion and resonant ultrasound spectroscopy. These measurements allowed a deeper insight into the lattice dynamics of materials and other important lattice related properties such as the elastic behavior, the heat capacity, force constants and Debye temperatures. The low Debye temperatures, combined with the low sound velocities are key factors to the low thermal conductivity in chalcogenides and are associated to the high thermoelectric efficiency in these systems.

It was observed that PbTe and SnTe have a softer structure (NaCl-structure and rhombohedrally distorted NaCl-structure, respectively) than GeTe (rhombohedral). Our results are found to be in fair agreement with the *ab initio* calculations, in the case of PbTe and GeTe, and from experimental data by inelastic neutron scattering for SnTe. Similar results were found for AgSbTe₂, including low sound velocity and low Debye temperature. In this material, however, additional vibrational modes at low energy related to the presence of the secondary phase Ag_{4.3}Te₃ were identified which influences the overall vibrational properties of the material, including its thermal conductivity. A large Grüneisen parameter, $\gamma = 2.3$, at 300 K, in combination with the short phonon lifetime are also related to the glassy nature of the low thermal conductivity in AgSbTe₂.

For LAST-18, we observed a great discrepancy between our NIS data and reported first-principles calculations and inelastic neutron scattering data, especially concerning the cut-off energy for Sb. From NIS, the Sb behavior in LAST-18 is very similar to that of Sb in AgSbTe₂, and the Te DPS in LAST-18 is very similar to the Te-DPS in PbTe. A mismatch in the acoustic range of the Sb and Te DPS of matrix and nanostructures is seen, and is one additional contribution for scattering phonons at phase interface and for reducing the thermal conductivity in the LAST family of materials. The local structure in LAST-18 is strongly affected by the synthesis conditions, which enable new degrees of freedom for optimization of the thermoelectric efficiency in these materials.

Based on our first measurements on the pure binaries, further investigations on alloys, *e.g.*, Ge or Sn in PbTe and/or Pb in SnTe and GeTe, are now possible. In the future, for pure binaries, by varying the sample environment and performing NIS at high pressure, the Grüneisen parameter could be directly obtained and the crystal anharmonicity, which strongly

affects the behavior of the crystal lattice and the thermal conductivity in the material, could be quantified.

The origin of the anharmonic character and its relation to the low thermal conductivity, should be revisited by theoretical calculations and further experimental investigations of the phonon density of states in a pure AgSbTe₂ compound, considering a chemically ordered random-network, stochastic, model.

In LAST-18, element selectivity may be added to the study of local structure, and possible, ordering, by extended x-ray absorption fine structure spectroscopy, EXAFS, for local ordering or imaging techniques such as high-angle-annular-dark-field scanning transmission electron microscopy, HAADF-STEM, for atomic resolution. Differential atomic PDF could also be exploited, which involves measuring two diffraction data sets below the absorption edge of an atomic species, taking the difference between the two data sets, and Fourier transforming it to real space. The correlations relative to the element whose absorption edge is probed up to the longest interatomic distances to which they extend could be obtained, for *e.g.* Ag and Sb atoms. Mechanical characterization of LAST alloys at working temperatures is required, in order to assure mechanical stability and reliable working performance.

Vita

Paula Bauer Pereira was born on the 6th September 1984 in Lages, Brazil. She received her undergraduate diploma in Materials Engineering from the Federal University of Santa Catarina in February 2007. In the period from 2007-2009, she was part of the european FAME (Functionalized Advanced Materials and Engineering) Master Program, as part of the Erasmus Mundus Program. Such international elite program awarded her with a double degree of Master in Sciences, from the University of Bordeaux I, in France, and the Augsburg University, Germany. Her master thesis on the “Synthesis of composite materials based on alloy engineering and nanoparticle technology in thermoelectric PbTe system” was written at the ICMCB-CNRS under the supervision of Dr. Stéphane Gorsse. She carried out her doctoral research at the Forschungszentrum Jülich and the University of Liège under the supervision of Dr. Raphaël Hermann.

Publications and submitted or prepared manuscripts:

1. S. Gorsse, P. Bauer Pereira, R. Decourt, E. Sellier, **Microstructure Engineering Design for Thermoelectric Materials: An Approach to Minimize Thermal Diffusivity**, *Chem. of Materials* **22**, 988-993 (2010).
2. J. Dadda, E. Müller, S. Perlt, T. Höche, P. Bauer Pereira, R. P. Hermann, **Microstructures and nanostructures in long-term annealed $\text{AgPb}_{18}\text{SbTe}_{20}$ (LAST-18) compounds and their influence on the thermoelectric properties**, *J. of Mat. Research* **26**, 1800-1812 (2011).

3. J. Dadda, E. Müller, B. Klobes, P. Bauer Pereira, R. P. Hermann, **Electronic Properties as a Function of Ag/Sb Ratio in $\text{Ag}_{1y}\text{Pb}_{18}\text{Sb}_{1+z}\text{Te}_{20}$ Compounds**, *J. Electr. Mater.* **41**, 2065-2072, (2012).
4. S. Perlt, T. Höche, J. Dadda, E. Müller, P. Bauer Pereira, R. P. Hermann, M. Sarahan, E. Pippel, R. Brydson, **Microstructure analyses and thermoelectric properties of $\text{Ag}_{1-x}\text{Pb}_{18}\text{Sb}_{1+y}\text{Te}_{20}$** , *J. Sol. State Chem.*, **193** 58-63 (2012).
5. P. Bauer Pereira, S. Gorsse, I. Sergueev, J. Dadda, E. Müller, R. P. Hermann, **Lattice dynamics and structure of GeTe, SnTe and PbTe**, submitted to *Physica Status Solidi B* (2012).

